

THESIS

A TEST OF GENERAL SHEAR VERSUS FOLDING FOR THE ORIGIN OF A CRYPTIC
STRUCTURAL FEATURE, NASON TERRANE, WASHINGTON

Submitted by

Max Alexander Jackl

Department of Geosciences

In partial fulfillment of the requirements

For the Degree of Master of Science

Colorado State University

Fort Collins, Colorado

Summer 2013

Master's Committee:

Advisor: Jerry Magloughlin

John Ridley
Graham Baird
John Stednick

Copyright by Max Alexander Jackl

All Rights Reserved

ABSTRACT

A TEST OF GENERAL SHEAR VERSUS FOLDING FOR THE ORIGIN OF A CRYPTIC STRUCTURAL FEATURE, NASON TERRANE, WASHINGTON

The Nason terrane of the Cascades Crystalline Core is a complex tectonostratigraphic terrane that has been the topic of much study due to its long deformational history and importance in the debate surrounding the Baja B.C. hypothesis. Structural patterns along Nason Ridge in the central part of the terrane have been interpreted as the result of either the presence of a major shear zone or the development of fold interference patterns. Distinguishing fold-controlled lineations from shear zone produced lineations can be a complex, but important problem. This study aims to provide a better understanding of high-temperature deformation which may be obscured due to extensive recrystallization.

Outside of the cryptic zone the foliation is steeply dipping and striking to the NW with lineations which are subhorizontal. Previous observations revealed a structural zone ~1 km wide striking NW-SE. Within the zone, fold hinges and mineral lineations are typically subvertical with mineral lineations clustering tightly and trending NE, indicating that this zone has a fundamentally different structural fabric than the surrounding terrane. Fold hinge lines are more dispersed along the trend of the zone, possibly reflecting incomplete rotation of pre-existing fold hinges into a near vertical orientation.

Anisotropy of magnetic susceptibility analysis indicates the magnetic fabric correlates well with lineations and foliations measured in the field, and lineations likewise shallow to near horizontal outside the zone. Quantification of the strength of the AMS fabric reveals an oblate spheroid, which is interpreted as a proxy for an oblate strain ellipsoid, indicating the presence of a component of pure

shear. Asymmetrical microstructural features present include tailed porphyroclasts, mineral fish, and domino clasts. Sense of shear indicators agree with the hypothesized NE-side-up motion (Magloughlin, 1990).

Electron backscatter diffraction analysis reveals biotite and amphibole possess a lattice preferred orientation (LPO), whereas quartz and plagioclase have a nearly random crystallographic fabric. The biotite and amphibole LPO was used to determine NE-side-up sense of shear in thin sections from the cryptic zone.

It is clear from the agreement between outcrop scale structures, magnetic fabric, microstructures, and crystallographic fabric that a significantly different structural fabric is tightly localized on the zone. The highly focused nature of the zone and the lack of structures typically created by fold interference indicates that superposed folding is unlikely. These data, coupled with geothermobarometric constraints, point to a zone of displacement best characterized by northeast-side-up general shear.

ACKNOWLEDGEMENTS

Many thanks go to my family, especially my amazing wife for all of her love, encouragement, and patience throughout this process. I could not have done this without her support. Thank you to Mike Jackson and the Institute for Rock Magnetism for the invaluable help and insight they gave me while in Minnesota, and after I left. Thanks to Kevin Mahan for generously donating his time, assistance, and lab space for EBSD analysis at the University of Colorado. Tyler Keck was an amazing field assistant who helped me immeasurably, kept me company, and kept me warm with his fire making skills. Thank you to the many friends I made while at CSU who have helped me work through many issues, scientific and otherwise. Finally, much appreciation goes to my advisor, Jerry Magloughlin, for the incalculable amount of time, energy, advice, and support he has offered me. Thank you all.

Soli Deo gloria.

TABLE OF CONTENTS

ABSTRACT.....	ii
ACKNOWLEDGEMENTS.....	iv
1. Introduction	1
1.1. Purpose and scope.....	1
1.2. Geologic setting	2
1.2.1. The Baja B.C. Hypothesis and the tectonic history of the crystalline core of the North Cascade Mountains	2
1.2.2. Geology of the North Cascades Crystalline Core	5
1.2.2.1. Location.....	5
1.2.2.2. Mount Stuart Batholith.....	5
1.2.2.3. Structural geology and deformational history.....	6
1.2.2.4. Petrology and metamorphic history.....	7
1.2.2.5. Differences between the northern and southern parts of the terrane.....	9
1.3. The Rock Lake ‘Cryptic Zone’	10
1.3.1. Proposal/Discovery	10
1.3.2. Fold hypothesis for the Rock Lake area	11
1.3.3. Closing remarks.....	12
2. Methods.....	18
2.1. Field methods	18
2.1.1. Travel and access	18
2.1.2. Equipment.....	18
2.1.3. Data collection	18
2.2. Analytical work.....	19
2.2.1. Magnetic techniques.....	19
2.2.2. Microscopy.....	21
2.2.2.1. Photo analysis and editing	22
2.2.2.2. Vorticity analysis	22
2.2.3. Electron Backscatter Diffraction (EBSD)	23
3. Results.....	34

3.1. Field work and structural data	34
3.1.1. Petrology	34
3.1.1.1. Schist	34
3.1.1.2. Orthoamphibolite	34
3.1.1.3. Metatonalite	35
3.1.2. Structural geology	35
3.1.2.1. Foliation	35
3.1.2.2. Folds	35
3.1.2.3. Mineral lineations	36
3.1.2.4. Boudinage	37
3.2. Analytical Results	50
3.2.1. Magnetic data	50
3.2.1.1. Room temperature AMS	50
3.2.1.2. High temperature magnetic susceptibility	59
3.2.1.3. Low temperature susceptibility	62
3.2.2. Microscopy	64
3.2.2.1. Microstructures and fabrics	64
3.2.2.2. Vorticity	75
3.2.3. Electron Back Scatter Diffraction (EBSD)	78
4. Interpretation and discussion	86
4.1. Field and structural data	86
4.2. AMS	88
4.3. Microstructures and petrology	89
4.4. EBSD	91
5. Conclusions and future work	94
5.1. Conclusions	94
5.2. Future work	95
6. References Cited	97
7. Appendices	105
7.1. Appendix I - Field Data and Structural Measurements	105
7.2. Appendix II - Microstructural Data	115
7.3. Appendix III - Magnetic Data	119

1. Introduction

1.1. Purpose and scope

The goal of this study is to better understand the processes of folding and ductile shearing in the formation and/or reorientation of lineations in relatively weak metasedimentary rocks which may be obscured due to extensive recrystallization. The Rock Mountain area along Nason Ridge in the North Cascades Crystalline Core of northern Washington will serve as the locality for this study. It is well known that pelitic schist commonly does not retain abundant evidence of early stages of deformational and metamorphic histories due to a propensity to thoroughly recrystallize, thus destroying previous fabrics (Passchier and Trouw, 2005; Trouw et al., 2009). Although ductile shear zones commonly cut through rheologically weak rocks (Trouw et al., 2009), surprisingly little work has been devoted to identifying and characterizing the effects of shearing and subsequent recrystallization. Rock Mountain is an ideal location for this study due to its accessibility and the relatively well studied terrane in which it is located. Additionally, arguments regarding its deformational history have already been supplied by Magloughlin (1993, 1995) and Miller et al. (2006), thus providing two testable hypotheses. Secondary purposes include 1) the better understanding of the deformational history the Nason Terrane and 2) how the lack or presence of a large scale shear affects the Baja B.C. hypothesis with respect to the role played by the Nason Terrane in this controversy.

Multiple methods have been undertaken to better understand the structural history of this area. Detailed structural mapping and magnetic susceptibility techniques are utilized to better understand the structural fabric and recent deformational events. Sense of shear and vorticity analyses performed aide in reconstructing the strain history of the area. Finally, electron backscatter diffraction is employed to examine the crystallographic fabric, also assisting in the understanding of strain history.

1.2. Geologic setting

1.2.1. The Baja B.C. Hypothesis and the tectonic history of the crystalline core of the North Cascade Mountains

The geologic history of the crystalline core of the North Cascade Mountains centers on the validity of the Baja B.C. hypothesis (Beck and Noson, 1972; Monger and Price, 1979). This model states, in part, that large blocks of the North Cascades Crystalline Core originated approximately 2000 km south, approximately at the latitude of northern Mexico. The name Baja B.C. comes from Baja California and British Columbia, the hypothesized original and current latitudes, respectively (Coney et al., 1980; Monger and Irving, 1980). After the rise in acceptance of plate tectonics in the 1960's and early 1970's, the terrane model was popularized as an explanation for the allochthonous nature of much of the west coast of North America (Monger et al., 1972; Coney et al., 1980). However, the assertion that these terranes also experienced thousands of kilometers of northward translation remains controversial. At the center of this debate are discordant paleomagnetic data (Irving et al., 1980; Beck et al., 1981) with paleopoles between 10 and 30 degrees of tilt off of their Cretaceous reference poles. The dominant alternate theory to explain discordant paleomagnetic data is the large scale tilting of crustal blocks (Costanzo-Alvarez and Dunlop, 1988; Butler et al., 1991).

Early in the discussion, papers by Bates et al. (1981) and others focused predominately on magnetic data supporting a significant degree of rotation. Those in favor of the Baja B.C. hypothesis generally agree that terranes have moved longitudinally due to the shear strain applied by the oblique NE motion of the Kula and Farallon plates (Monger and Price, 1979; Beck et al., 1981). This oblique motion is presumed to have also caused clockwise rotation, in addition to up to 4000 km of transportation of major crustal blocks (Beck, 1976; Butler et al., 2001).

Several studies (Bates et al., 1981; Wells, 1990; Ague and Brandon, 1996; Symons, 2000) report Cretaceous paleomagnetic data which shows upwards of 25° of clockwise rotation relative to the

reference Cretaceous pole. Simply put, many authors are reluctant to accept a mechanism for this degree of rotation without major tectonic translation. Oblique forces on these blocks would predictably create very large amounts of shear strain – enough to cause the rotation of major pieces of continental lithosphere (Bates et al., 1981; Wells, 1990). In addition, this view is supported by Wells (1990) in a study which found that dextral shear is noticeably increased in rocks closer to the coast. That study also noted that this increased dextral shear is present throughout various depths along the west coast, implying that the increased strain was continuous throughout the Cretaceous. Additionally, Wells notes that the pattern of seismicity after the eruption of Mount St. Helens shows substantial dextral slip which is currently occurring in the North Cascades. This could be evidence that this process is still active (Wells, 1990).

The alternative to the Baja B.C. hypothesis is that large-scale tilting and a small degree of clockwise rotation of these blocks better explains the discordant paleomagnetic poles observed (Beck et al., 1981; Butler et al., 1989). However, it is notable that a consensus has not been reached over the exact mechanism of how this tilting and rotation happen devoid of significant latitudinal translation (Ague and Brandon, 1996).

Cowan et al. (1997) proposed several “crucial tests” by which the Baja B.C. controversy may be resolved. One such test has been labeled the “detrital zircon test”, which was taken up by Mahoney et al. (1999). They assert that detrital zircons within Cretaceous strata have no known source in the southwestern continental U.S. or northern Mexico. However, there are known drainages of detrital sources in the northwest U.S. and Canada. Mahoney et al. (1999) analyzed detrital zircons in early Cretaceous northwest terranes, coming to the conclusion that Cretaceous detrital zircons could not have been carried downstream to the southwestern coast of what is now near northern Mexico and then transported back north by tectonic processes. It is much more likely that these terranes were accreted in more or less their current position, and the zircons were deposited with the terranes already in their

northern latitude (Mahoney et al., 1999). Ague and Brandon (1996) also added evidence in support of the tilting hypothesis by attempting to reconstruct paleohorizontal using the aluminum-in-hornblende (AH) barometer. From their study, it was determined by the AH barometer that pressures of the Mount Stuart batholith (MSB) decrease from 0.3 GPa in the northwest to 0.15 GPa in the southeast, implying that the northern end of batholith has been tilted upward. One interesting aspect of their study was the evidence for southeast tilting, as opposed to previously suggested southwest down tilting. After reconstruction, the study determined that the batholith has been tilted by up to 9° (Ague and Brandon, 1996). However, critics of this study note several problems with Ague and Brandon's conclusions. It was first noted that Ague and Brandon did not properly calibrate their data to take into account how aluminum content changes with temperature (Anderson, 1997). Later, objections were again raised regarding Ague and Brandon's endeavor to determine a paleobarometric surface in the MSB, regional relationships which affect interpretations of tilt, the direction of motion on the Windy Pass thrust, and proper interpretation of existing paleomagnetic data for the MSB (Paterson and Miller, 1998). Housen et al. (2003) added 20 new paleomagnetic sites from the Mount Stuart batholith and adjacent Beckler Peak stock. Like Ague and Brandon (1996), Housen et al. used the AH barometer to estimate paleohorizontal, and concluded that magnetization found throughout the MSB supports the northward translation of significant portions of the Pacific Northwest Cordillera (Housen, 2003).

1.2.2. Geology of the North Cascades Crystalline Core

1.2.2.1. Location

The Nason Terrane (Tabor et al., 1987) is a tectonostratigraphic terrane making up a significant portion (over 2000 km²) of the North Cascades Crystalline Core (Misch, 1982) of northern Washington. This allochthonous terrane is a member of the Wenatchee block (Haugerud, 1987) (Fig. 1.1) – a group of terranes which have undergone a similar metamorphic history. The terrane was named for Nason Creek along U.S. Highway 2 where rocks typical of the terrane are well exposed (Tabor et al., 1987). Whole rock Rb-Sr and Sm-Nd analyses (Magloughlin, 1993) indicate that the protolith for the basement unit to the terrane, the Chiwaukum Schist, is approximately early Permian to Triassic.

The Nason Terrane is bounded by the Leavenworth fault to the east, and the Evergreen Fault and Straight Creek Fault Zone to the west (Tabor et al., 1987). Additionally, it is bounded by the White River Shear Zone (Magloughlin, 1988) to the northeast where it meets the Mad River terrane, and it is overthrust by the Ingalls Ophiolite Complex to the south at the Windy Pass thrust (Fig. 1.2) (Miller, 1985).

The Chiwaukum Schist of the Nason Terrane is believed to correspond with the Settler Schist of British Columbia (Fig. 1.3), and was offset by the Straight Creek-Fraser fault system (Evans and Berti, 1986; Ague, 1990; Magloughlin and Edwards, 1993).

1.2.2.2. Mount Stuart Batholith

The Mount Stuart Batholith (MSB) played a major role in the metamorphic and deformational history of the Nason Terrane, as well as in the larger debate surrounding the Baja B.C. hypothesis. By intruding into the Ingalls Ophiolite to the south, as well as the Chiwaukum Schist of the Nason Terrane to the north, the batholith is a stitching pluton in the same way that many allochthonous terranes are joined by large intrusive bodies (Ague and Brandon, 1996).

The batholith consists primarily of tonalite, quartz diorite, and granodiorite (Erikson, 1977). Locally, it also contains granite, gabbro, and some ultramafic rocks (Ague and Brandon, 1996). Batholith emplacement occurred at approximately 93 to 96 Ma as determined by U-Pb zircon dating, making the MSB the largest of a suite of calc-alkaline intrusions from the late Cretaceous (Ague and Brandon, 1996; Benn et al., 2001).

It is believed that the MSB was emplaced at about 7 to 12 km depth, as demonstrated by abundant andalusite in the contact aureole around the body (Evans and Berti, 1986). More recent studies have confirmed that the MSB experienced pressures of < 4 kbar (Stowell et al., 2007a).

1.2.2.3. Structural geology and deformational history

Several studies have attempted to decipher the deformational history of the Nason Terrane (Getsinger, 1978; Brown and Talbot, 1989; Magloughlin, 1993, 1995; Paterson and Miller, 1998; Paterson, 2004; Miller et al., 2006) giving rise to several different models. Most of these models are similar in their approximate order and timing of deformation, but group or divide stages differently. One of the more straightforward of these was offered by Magloughlin (1993), and is summarized here along with supplementation by other relevant studies.

The deformational history of the Nason Terrane can be divided into roughly four major events. The first event (D_1) is preserved rarely, but is present in floating fold hinges (that is, fold hinges which have been disconnected along their limbs) and inclusion trails within porphyroblasts. The relict fold hinges are quartzofeldspathic or amphibolitic, and do not show a consistent orientation. The scarcity of these fold hinges along with the parallelism of S_1 with S_0 suggests that foliation did not develop from folding, but more likely from layer-parallel shear early in the deformational history (Magloughlin, 1993, p. 109). Inclusion trails of graphite, oxides, and quartz within garnet, staurolite, kyanite, micas, and plagioclase also preserve this early D_1 event.

The D_2 event is a folding of S_1 creating an S_2 crenulation cleavage which is also preserved in porphyroblasts.

D_3 formed the dominant foliation and lineation throughout the majority of the terrane. The foliation generally strikes NW-SE and commonly dips NE. Fold hinges trend NW or SE with dominantly shallow plunges. Stretching lineations are similarly oriented, and have subhorizontal plunges. The origins of this regional fabric are not agreed upon. Magloughlin (1990) suggested the foliation resulted from regional shear strain related to tectonic unroofing during the Cretaceous. It has also been proposed that regional transpression (Brown and Talbot, 1989), or NE-SW shortening (Paterson, 2004; Stowell et al., 2007b) could be the primary cause of the regional fabric. Paterson (2004) states that from roughly 96-73 Ma the Crystalline Core experienced SW-NE contraction and crustal thickening (responsible for the dominant regional fabric), which was then followed by dextral transpression from approximately 73-55 Ma, and finally transtension after 55 Ma, with the added note that exhumation was ongoing during all three phases.

D_4 produced folding of S_3 , and occurs at a variety of scales, including large-scale folding within the terrane. D_4 may have overlapped with D_3 or may have occurred as a separate event associated with the unroofing of the terrane (Magloughlin, 1993), and at somewhat lower temperature than D_3 .

D_5 is a widespread pseudotachylite forming event which is not associated with any particular fault or shear zone and is parallel to S_3 (Magloughlin, 1993).

1.2.2.4. Petrology and metamorphic history

The Nason Terrane, from old to young, consists primarily of the Chiwaukum Schist (Tabor et al., 1987), the Nason Ridge Migmatitic Gneiss (Van Diver, 1967), and the Wenatchee Ridge Orthogneiss (Magloughlin, 1986), as well as the intrusive rocks associated with the Mount Stuart Batholith (Erikson, 1977). Although primary bedding can be difficult to ascertain due to several metamorphic and

deformational events, Magloughlin (1993) notes that various lithologies (amphibolite schist, metagraywacke, metapelites, marble, and calc-silicates) preserve primary layering. Additionally, mineralogical changes at the microscale, such as zoning of quartz-tourmaline-graphite layers are interpreted to be indications of original bedding (Magloughlin, 1993), as are layers of cotecule – metasedimentary units which are composed of > 90% Mn-rich garnet (Magloughlin, 1986, p. 98-101).

The Chiwaukum Schist is pelitic to semi-pelitic, containing zones which display increased concentrations of amphibole, graphite, quartz, or biotite, and compositional zoning is generally gradational (Getsinger, 1978). In the study area, the schist is within the staurolite-kyanite zone of the middle amphibolite facies (Getsinger, 1978) with peak metamorphic pressures >8.5 kb to the NE in the Wenatchee Ridge area (Magloughlin, 1987; Magloughlin and Evans, 1987). The Nason Ridge Migmatitic Gneiss (Tabor et al., 1987) is a name given to extensively tonalite-intruded Chiwaukum Schist. The Wenatchee Ridge Gneiss (Van Diver, 1964, p.131), renamed the Wenatchee Ridge Orthogneiss (WRO) (Magloughlin, 1986; Zaggale and Magloughlin, 2013) is mostly tonalitic to leucotrochhemitic (Getsinger, 1978). The WRO is a dominantly sill-like sheeted pluton which geochemically may act as an analog to Archean tonalite-trondhjemite-granodiorite crust (Zaggale and Magloughlin, 2013). Foliation in the WRO is approximately parallel to the Chiwaukum, and contacts between the two are generally sharp at the outcrop scale, but gradational at the map scale (Getsinger, 1978; Magloughlin, 1986), meaning there is usually a broad area of interfingering of schist and sills.

Descriptions by Evans (1986) note an earlier Buchan (contact) type metamorphism which was interpreted to have been caused by the MSB, followed by a Barrovian style event which is generally associated with metamorphism on a regional scale due to crustal thickening. Though there is no debate that crustal thickening occurred during the late Cretaceous at ca. 90 Ma, the tectonic cause, as well as the mode of thickening is still poorly constrained, with several possibilities offered, including thrusting

(Monger et al., 1982; Magloughlin, 1995; Stowell et al., 2007a), magma emplacement (Brown and Walker, 1993), and large scale folding (Miller et al., 2006; Stowell et al., 2007b).

The Nason Terrane has undergone at least three major metamorphic events (Magloughlin, 1993). The earliest of which (M_1 – ca. 118 Ma (Magloughlin, 1993, p. 255) ca. 120 Ma (Stowell and Tinkham, 2003)) produced the oldest metamorphic garnets which predate the intrusions of the Late Cretaceous plutons such as the MSB. M_2 is marked by andalusite and other associated minerals which occur in close proximity to Late Cretaceous plutons, and are interpreted to be of a contact metamorphic origin (Evans and Berti, 1986). The most recent metamorphic minerals include sillimanite and kyanite which postdate peak plutonism and indicate a regional M_3 event with pressures ranging from <5 kbar in the south to >8 kbar in the north (Brown and Walker, 1993). Three competing hypotheses accounting for the M_3 event and pressure gradient are 1) rigid tilting (Stowell et al., 2007a) 2) crustal loading from magma or a thrust sheet (McGroder, 1991; Brown and Walker, 1993) or 3) wedge thickening with variable shortening from NE to SW (Miller et al., 2006). After detailed analysis, Stowell et al. (2007b) conclude that fold-related crustal thickening is the preferred model, stipulating that thrusting by faulting/shearing is also a likely explanation, but that shearing is omitted on the basis of a lack of evidence.

1.2.2.5. Differences between the northern and southern parts of the terrane

Several studies have observed geologic differences between the northern (or northeastern) and southern (or southwestern) parts of the Nason Terrane (Magloughlin, 1990, 1993, 1995; Ague and Brandon, 1996; Miller et al., 2006; Stowell et al., 2007b). The fundamental difference between the northern and southern parts are dissimilar pressures, and therefore depths, of up to 9 kb in the north, and as low as 3 kb in the south (Magloughlin, 1995). Possible explanations for this pressure discrepancy include a large displacement of rock by folding (Miller et al., 2006), shearing (Magloughlin, 1993), or

crustal tilting (Ague and Brandon, 1996). Although tilting of massive crustal blocks on some scale is plausible, a number of authors have discounted the idea that a significant amount of tilting caused the discrepancies in pressures seen in the Cascades crystalline core (Beck Jr, 1992; Anderson, 1997; Butler et al., 2001; Stowell et al., 2007b).

The discrepancies in depth/pressure between the north and south areas of the terrane are reflected in different lithologies, metamorphic grades, deformational features, P-T-t paths, etc. Magloughlin (1990, 1993), describing the “split personality of the Nason Terrane”, observed 1) more abundant metagraywackes in the south, 2) more common occurrence of marble in the north, 3) differences in chemical composition (the reader is referred to the cited paper for details), 4) a lower prevalence D_3 fabrics in the south, 5) common pseudotachylyte in the north and none in the south, 6) evidence of more rapid cooling in the south, 6) more occurrences of tonalitic pegmatites in the north, and 7) evidence that plutons show different levels of crustal emplacement with wide contact aureoles in the south and very small or absent aureoles in the north.

1.3. The Rock Lake ‘Cryptic Zone’

1.3.1. Proposal/Discovery

Due to the various differences between the northern and southern parts of the Nason Terrane, Magloughlin (1990, 1993, 1994) hypothesized the presence of a large north-side-up structural discontinuity that would account for many of the discrepancies between the sides of the terrane. During mapping, Magloughlin discovered a zone centered on Rock Lake and crossing Nason Ridge. The zone is approximately 1 km wide and strikes roughly NW-SE, displaying steeply NE plunging mineral lineations, quartz vein hinges, and foliation hinges. Additionally, to the SE near Lake Ethel, similar structural features were found, as well as scattered evidence to the NW. It was concluded that these features represent a major reverse sense shear zone which he named the Rock Lake Shear Zone (RLSZ), and he

considered it at least partly responsible for the north-south discrepancies, although folding and tilting may have also played a role (Fig. 1.4).

Later studies showed a relatively sharp geobarometric discontinuity across the RLSZ (Magloughlin, 1994) as well as Ar-Ar dates on hornblende which show closure dates ranging from 86 to 90 Ma, shortly after the emplacement of the MSB. These dates also corresponded in timing to the White River Shear Zone (WRSZ) to the north. Ar-Ar dating on biotites from both sides of the RLSZ gave closure dates ranging from 83 to 86.5 Ma, implying rapid cooling of about 40-50° C/Ma (Magloughlin, 1995). This was interpreted to indicate that deformation along the RLSZ occurred at temperatures above the closure temperatures of hornblende, which is also supported by recrystallization of hornblende. It is because the RLSZ experienced thorough recrystallization at the same relatively high temperatures as the containing terrane, and therefore is not marked by any obvious lithological or textural discontinuities, the RLSZ was dubbed a “cryptic shear zone” (Magloughlin, 1995).

1.3.2. Fold hypothesis for the Rock Lake area

In a paper addressing the significance of composite lineations, Miller et al. (2006) examined in detail the lineations and structural features of the RLSZ and concluded “[...]detailed structural analysis indicates that local fold interference patterns control the structural morphology.” Here, Miller et al. attribute the subvertical lineations to local type-II fold interference. The claim that an asymmetric antiform which was overprinted by NW-trending folds is supported primarily by stereonet analysis showing the supposed earlier generation axial surface forming a great circle distribution near the perimeter whose pole lies on the axial surface of the later folds (Fig. 1.5).

Additionally, Miller et al. point to intrusive bodies as providing time constraints to deformation. It is noted that igneous intrusions are commonly boudinaged, which is interpreted to have been caused by the last increments of ductile deformation, along with the folding of other intrusive bodies.

1.3.3. Closing remarks

Because of the conflicting interpretations of the structures in the central part of the Nason Terrane, for the purposes of this study, this area will be referred to as the Rock Lake Cryptic Zone (RLCZ). It is the goal of this project to use the RLCZ as a case study for similar instances where the major deformational processes at work are not well constrained or kinematic features are not fully explained by the available data. Evaluating these two competing hypotheses regarding the RLCZ is the central focus of this study. It is the goal of this study to better understanding the processes of strain which occurred at the RLCZ, a better understanding of the structural history of the North Cascades can be achieved.

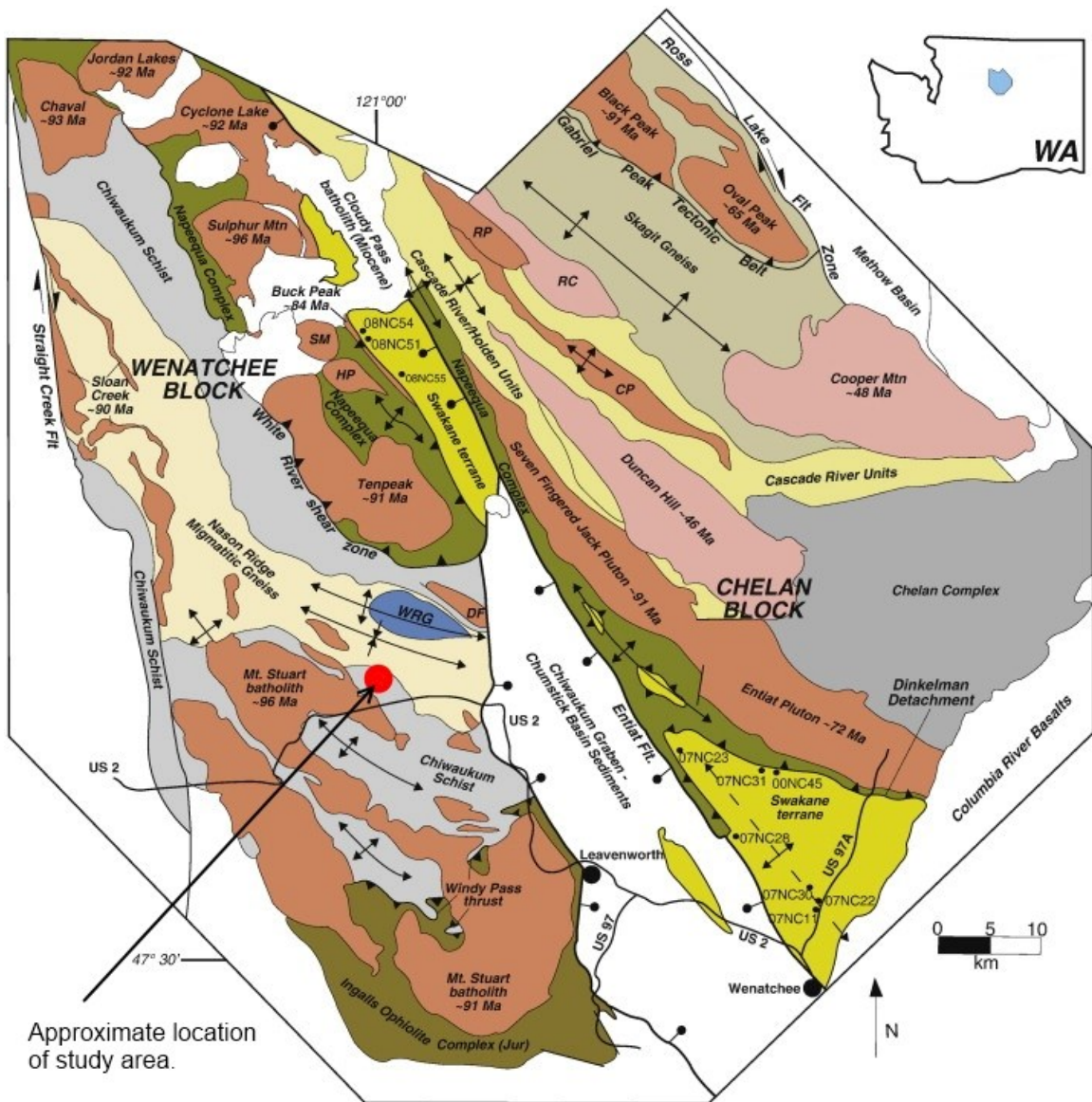


Figure 1.1: A portion of the North Cascades Crystalline Core, illustrating the position of the Chelan and Wenatchee Blocks, as well as other local data such as roads, towns, and structural features (after Tabor et al., 1989).

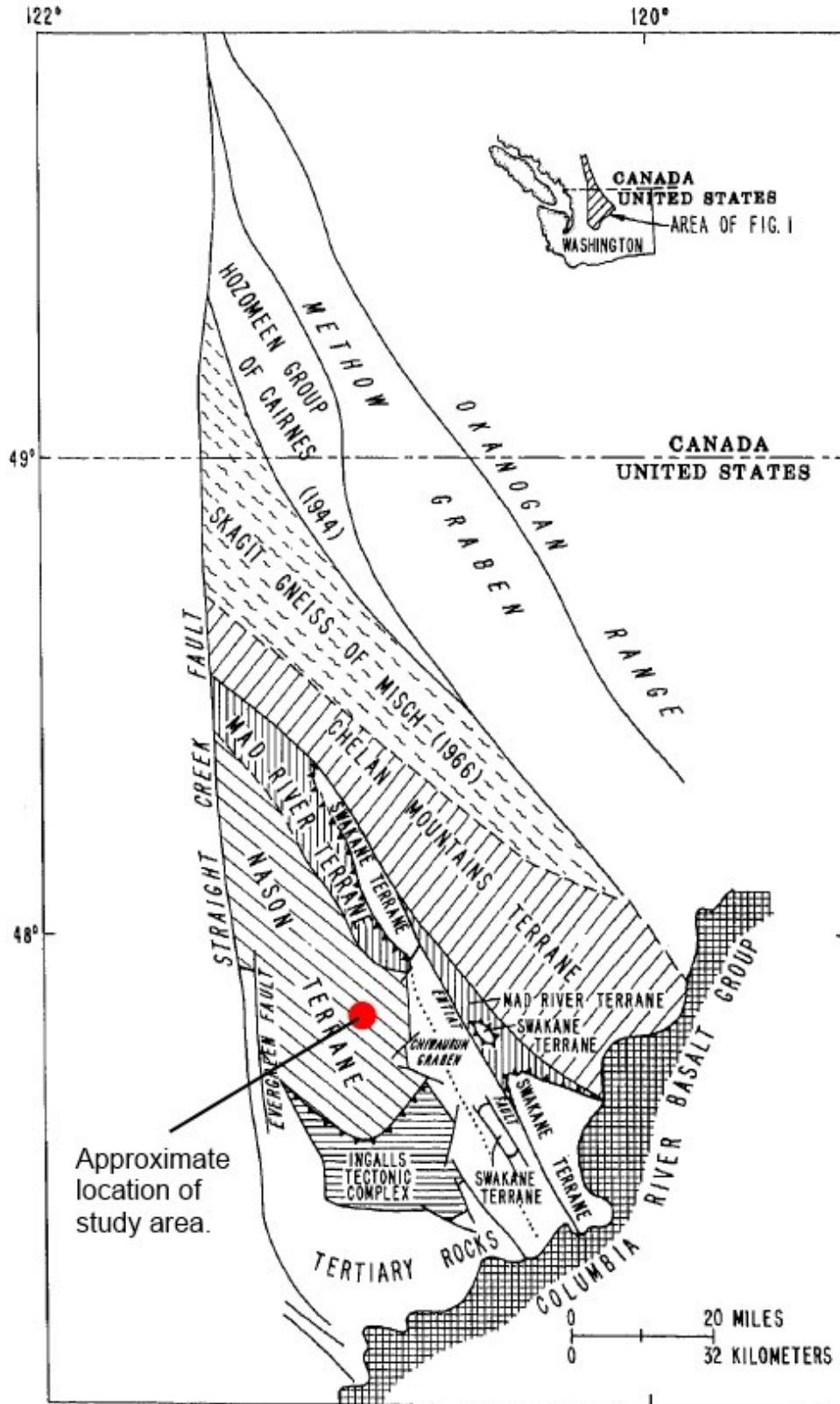


Figure 1.2: Map showing the various terranes, and structural and geologic features of the North Cascades Crystalline Core, including the Nason Terrane (from Tabor, 1987).

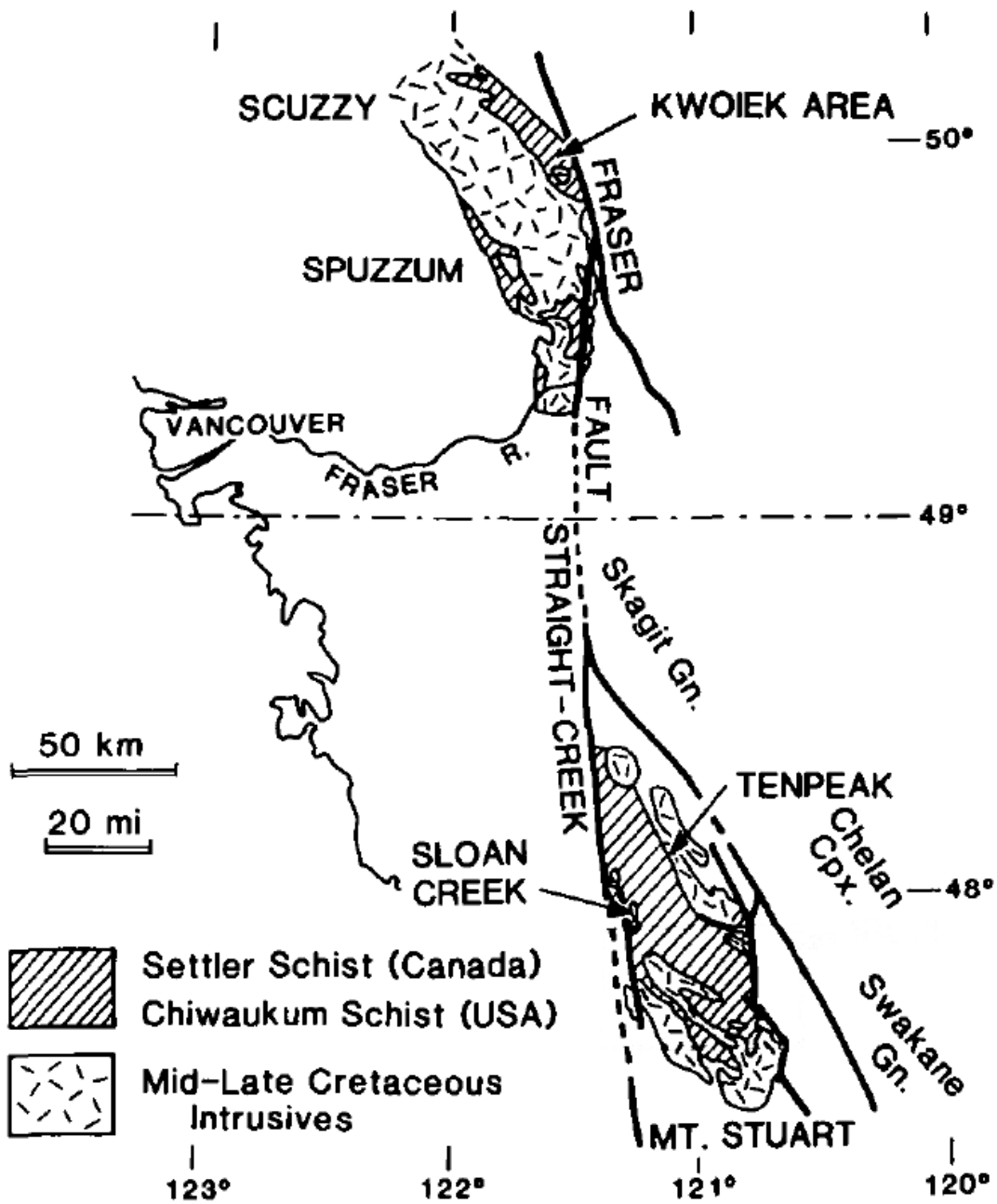


Figure 1.3: Map showing the lithological relations and offset along the Straight-Creek Fault. It can be seen that the Chiwaukum Schist and the Settler Schist were once a single continuous unit (after Evans, 1986).

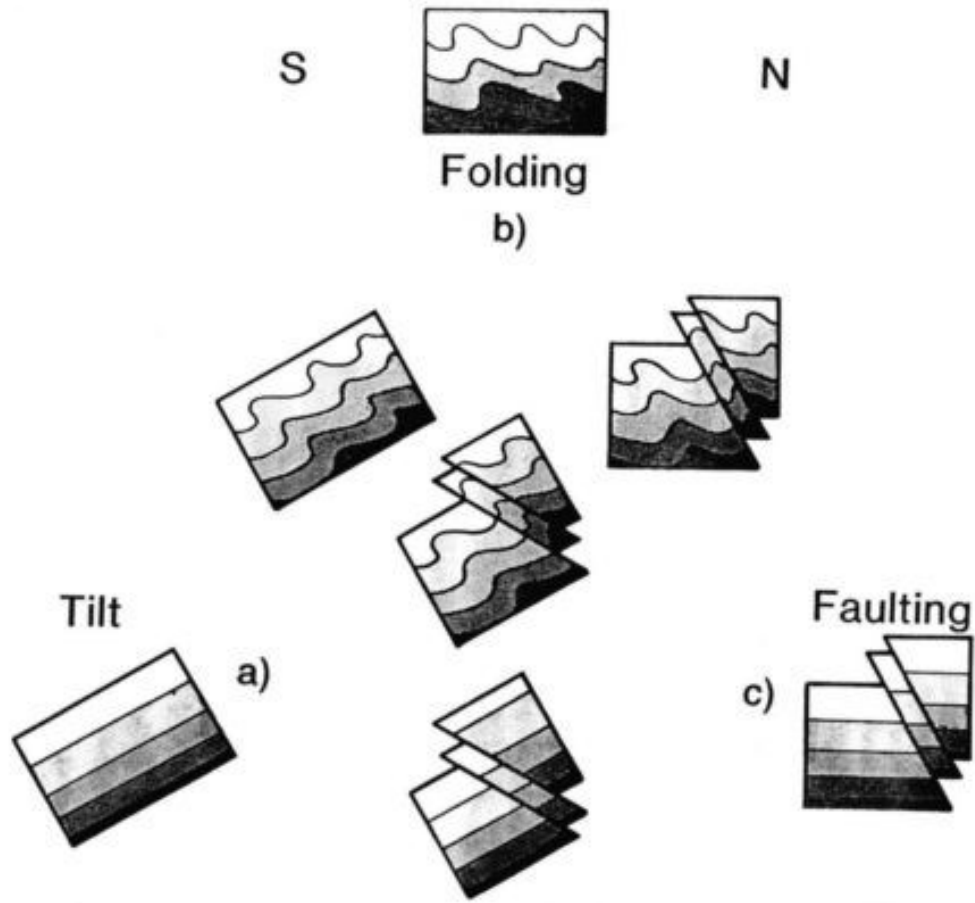


Figure 1.4: Diagram showing the possible combinations of tilt, folding, and faulting for the Nason Terrane that could explain the N-S pressure dichotomy (from Magloughlin, 1993, p. 121).

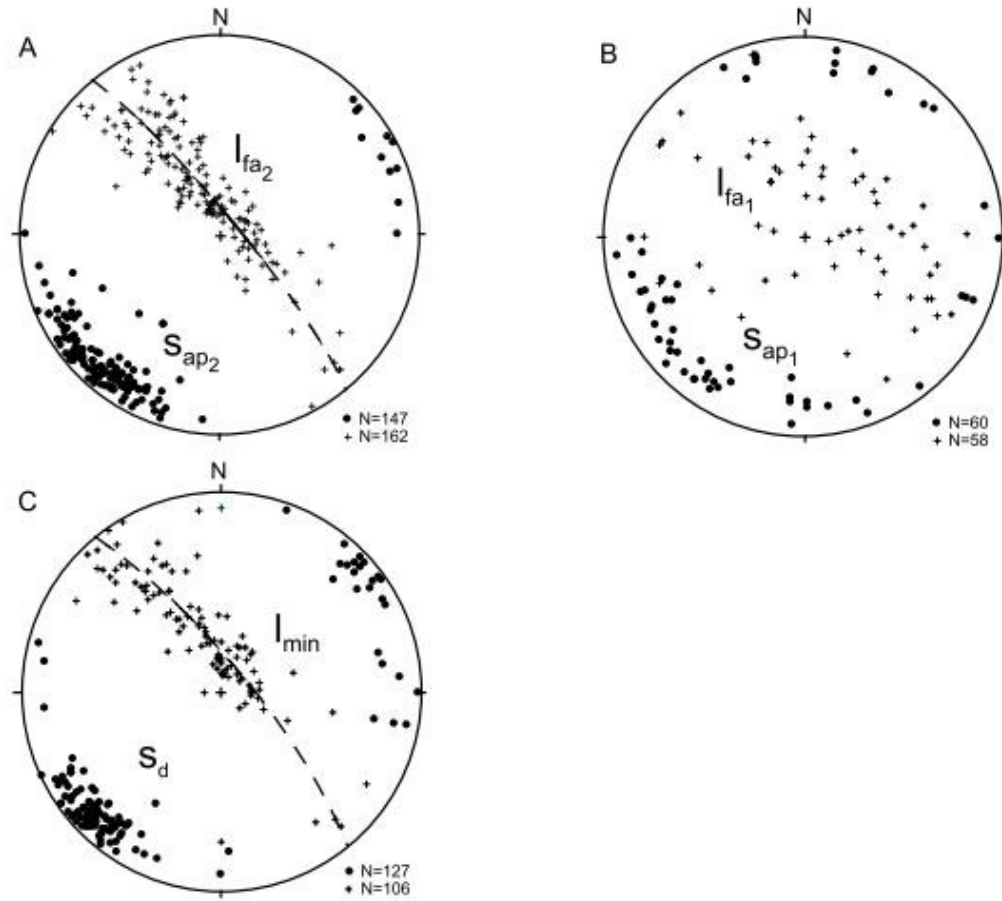


Figure 1.5: Stereonets from the Nason ridge area. Miller et al. interprets dashed great circle as approximate for the bulk axial plane of last generation folds. (A) I_{fa2} - and S_{ap2} -axes and axial planes of late upright folds. (B) I_{fa1} - and S_{ap1} -axes and axial planes of early folds. (C) I_{min} -mineral and elongation lineation, S_d -dominant foliation (from Miller et al., 2006).

2. Methods

2.1. Field methods

2.1.1. Travel and access

Field work for the study was done between August 1st and August 22nd 2011 along Nason Ridge in the Nason terrane, Washington. Rock Mountain is located 42 km northwest of Leavenworth, Washington. Travel to the field area was conducted by car and hiking. From the base of Rock Mountain, the Rock Mountain hiking trail was utilized, with an ascent of approximately 3400 feet (1,036 meters).

2.1.2. Equipment

For the purpose of collecting samples for anisotropy of magnetic susceptibility (AMS) analysis, a paleomagnetic rock drill from ASC Scientific was employed in the field. The bits used were Hoffman high performance diamond drill bits with stainless steel shanks. The use of stainless steel was necessary for protecting against corrosion which could alter the magnetic properties of the samples. Cores taken were 2.5 cm in diameter, and varied in length from 2.5-13 cm.

For navigation and cataloging each site location, a Garmin Oregon 450 GPS unit was utilized. The unit was set to use UTM coordinates derived from the WGS84 geoid. With its high-sensitivity, WAAS-enabled GPS receiver, the unit's accuracy is less than 3 meters. The alpine environment and generally good weather allowed for a strong satellite signal, and the accuracy of the GPS was close to its maximum throughout the project. A standard 360° Brunton Pocket Transit with the magnetic declination adjusted to 16.5° was used for orienting samples, cores, and collecting structural data.

2.1.3. Data collection

The majority of the work done and data collected was in the immediate vicinity of the cirque, which is approximately one square kilometer in area (Fig. 2.1) and contains Rock Lake, a tarn. Significant

effort was employed in order to sample along a transect which covered both inside and outside of the RLCZ. More specifically, the zone of interest strikes roughly NW-SE; therefore special consideration was given in sampling perpendicular to the zone, i.e. NE-SW. In addition to working in and in close proximity to the cirque, field work was also conducted along strike at the base of Nason Ridge along Highway 2. This was done with the hopes of correlating the results both along and perpendicular to strike.

All structural measurements were taken in degrees azimuth from north, and degrees from horizontal using the “right-hand-rule” method. Hand samples and drilled cores were also oriented in the same manner.

To produce stereonet, the program OpenStereo was used.

2.2. Analytical work

2.2.1. Magnetic techniques

Analyses on rock magnetism were done at the University of Minnesota’s NSF-funded Institute for Rock Magnetism (IRM) during the fall of 2011. Analyses were carried out on 43 samples. Sample preparation involved cutting drilled cores to approximately 2.5 cm lengths. Hand samples were also analyzed by cutting specimens into cubes with the smallest being 3 cm³ and the largest 16 cm³ in volume. Cataloging of specimens is done automatically by the IRM’s custom database software once sample IDs and orientation data are entered. The database also includes measurements of mass and volume which were not relevant for this study. Samples analyzed included a variety of locations along the Wenatchee Ridge, including at its base along Highway 2. All rock types obtained were analyzed which includes pelitic to semipelitic schist, metatonalite, amphibolite, and quartz-rich veins from within the schist.

To better understand the magnetic properties of the samples, four different techniques were used. First, AMS was done using both the Magnetic Anisotropy Bridge (affectionately known as the

“Roly-Poly”) (Fig. 2.2) which is a custom designed AMS bridge, and the Geofyzika KLY-2 KappaBridge AC Susceptibility Bridge (more simply, “KappaBridge”) (Fig. 2.3). Both of these instruments operate at room temperature by taking several measurements of the magnetic susceptibility in different positions, rotating along three axes. The alignment of the samples during analysis was done semi-manually, guided by a specimen orienting device specific to each machine (Fig. 2.4). These data can then be used to calculate other parameters such as degree of anisotropy, lineation parameter, foliation parameter, and shape factor. The Roly-Poly works by taking 600 measurements and then calculating the best-fit tensor by the method of least-squares. The applied field for the Roly-Poly ranged from 0.01 to 1 mT, with a sensitivity of 1.2×10^{-6} SI. The KappaBridge works by taking only 15 measurements (5 measurements per axis), yet is more accurate than the Roly-Poly and also less affected by irregularities in the shape of the sample and has a sensitivity of 4×10^{-8} SI.

In addition to standard room temperature susceptibility measurements, the KappaBridge is also capable of doing a temperature sweep from room temperature to 1000 K. For the purpose of this study, samples were heated to 700°C (974 K). In this mode, rather than a drill core or cube, the KappaBridge takes a small amount (a few hundred milligrams) of powdered sample in a glass pipette. This is because the purpose of this procedure is to identify the mineralogy responsible for giving the magnetic fabric rather than the orientation of the fabric. By progressively heating the samples, while simultaneously measuring the magnetic susceptibility, a curve plotting temperature versus magnetic susceptibility can be matched against known mineral samples to determine the magnetically susceptible minerals in the sample (Fig. 2.5). The approximate time to measure one sample with this method is 2.5 hours. Six samples were analyzed.

For the purpose of finding magnetically susceptible minerals, in addition to the high temperature KappaBridge measurements, a low temperature Quantum Design Superconducting Susceptometer (MPMS-5S) was also employed. This device cooled the samples down to 2.1 K, applying a

magnetic field ranging from 0 to 5 T. By cooling minerals to within a few degrees of absolute zero, crystallographic transitions take place, similar to when minerals are heated, and the magnetic susceptibility is measured, generating a curve which is compared to a known sample. Also similarly to the high temperature measurements, only a small amount of powdered sample is needed, which is then placed into a small pill-sized capsule to be analyzed.

2.2.2. Microscopy

Thin sections cut along the presumed X-Z plane (parallel to lineation, orthogonal to foliation) were examined primarily for structural fabrics and microtectonic features giving insight into coaxial versus non-coaxial deformation. Features characteristic of particular deformation mechanisms or strain history include deformation lamellae, recrystallized mantled clasts, inclusion trails, mineral fish, quarter-structures, S-C fabrics, microboudinage, domino-fractured clasts, strain shadows, crystallographic preferred orientation, and overall monoclinic symmetry. Additionally, petrologic relationships, such as mineralogy and alteration reactions, were examined to better understand the metamorphic conditions.

Microscopy was done on standard 30 μm polished thin sections. The petrographic microscope used was a Leica DM 2500P connected to a Clemex camera which allowed for image capturing (Fig. 2.6). The Clemex Captiva software (version 5.0.013j) enabled thin sections to be viewed on a Windows XP computer in real time, in addition to automatically adding a scale to each captured image.

In some cases, the field of view was too narrow, and multiple photographs were taken and stitched to create a mosaic, with the aid of Microsoft's free Image Composite Editor (ICE) software (version 1.4.4). When stitching together multiple photos, this program automatically chooses from 4 different algorithms to create the best result while minimizing distortion.

2.2.2.1. Photo analysis and editing

Photo editing was performed using the open-source software program Paint.NET. In all cases, editing was minimal and consisted of changes to resolution, brightness, contrast, gamma levels, white balancing, and other minor aesthetic changes. In cases where angles and distances were measured, the software used was the open source program GIMP. Finally, drawing of lines to indicate or highlight important features was performed using Adobe Illustrator.

2.2.2.2. Vorticity analysis

Vorticity analysis was done using the same Clemex Captiva software as was used for taking photomicrographs. Several methods for estimating vorticity have been proposed, including the use of deformed sets of veins or dikes, rigid porphyroclasts, porphyroblasts, quartz c-axis fabrics, macroscopic foliation, grain-shape foliation, shear bands, tension gashes, and several others (Xypolias, 2010). Due to the constraints upon many of these methods, the two best suited for this study are those that employ rigid porphyroclasts and quartz c-axes.

The theoretical framework for the use of rigid porphyroclasts as a vorticity gauge assumes that particles are rigid ellipsoids, particles are perfectly bonded to the matrix, and that the matrix behaves as a Newtonian linear-viscous fluid (Jeffery, 1922). Of the several methods which use rigid porphyroclasts, many require the ability to distinguish between σ - and δ -type tailed clasts. However, the porphyroclast aspect ratio (PAR) method (Passchier, 1987) as modified by Wallis et al. (1993), treats ϕ -, σ -, and δ -type tailed clasts as tailless, allowing for ambiguity in the type of clast (Wallis et al., 1993). This model predicts that for simple shear flow, all ellipsoidal particles rotate continuously and synthetically to the shear direction, and for general shear flow, rigid objects are not free to rotate continuously nor are objects required to rotate synthetically to the shear direction (Passchier, 1987).

The PAR method, as modified by Wallis et al. (1993) relies on the relation between the mean kinematic vorticity number (W_m), the aspect ratio of the porphyroclast (R =long axis/short axis), and the angle between the long axis of the clast and the flow plane (ϕ) where backwards rotating clasts (antithetic motion) have a positive angle for ϕ and forward rotating clasts (synthetic motion) have a negative value for ϕ (Fig. 2.7). By plotting a population of these clasts in relation to the XZ plane, it is possible to differentiate between clasts which are infinitely rotating (that is, given continued deformation, rotation would continue) and those which have limited rotation. The critical aspect ratio (R_c) delineates these two fields and defines $W_m = ((R_c^2-1)/(R_c^2+1))$ as demonstrated in Fig. 2.8 (Wallis et al., 1993; Xypolias, 2010). In this case, W_m is also equal to the critical shape factor (B_c) (Xypolias, 2010) by the equations:

$$B = ((R^2-1)/(R^2+1))$$

and

$$B_c = ((R_c^2-1)/(R_c^2+1))$$

therefore

$$B_c = W_m.$$

2.2.3. Electron Backscatter Diffraction (EBSD)

Electron backscatter diffraction (EBSD) was performed on quartz, biotite, muscovite, amphibole, and plagioclase at the University of Colorado in Boulder, Colorado. Because the behavior of quartz slip systems are well understood (Law, 1990), the orientations of quartz c-axes and a-axes were the primary target for analyses. However, biotite, plagioclase, garnet, and hornblende were also indexed. Standard (approximately 46 x 27 mm) polished petrographic thin sections were used, with additional sequential polishing, down through the use of 0.02 μm colloidal silica.

The instrument used is a JEOL low vacuum scanning electron microscope (JEOL LV-SEM), housed within and managed by the Nano Characterization Facility (NCF). The use of a LV-SEM is advantageous (as opposed to a high vacuum SEM) due to the low vacuum chamber's ability to prevent "charging" – the

effect of the electron beam negatively charging the sample – which degrades the quality of the image. Because of this, it was not necessary to coat the sample with a conductive material such as carbon or gold (Augenstein and Burg, 2011; Annis, 2012).

The JEOL LV-SEM in the NCF is equipped with an Oxford Labs EBSD camera. For data collection, the low vacuum chamber was set to 14 Pa, with an accelerating voltage of 20 KV. For one sample (RM-36) a step size (the spacing between spot measurements on the minerals surface) of 10 μm was used and found to be of higher resolution than required, and so samples RM-04 and RM-41 were analyzed with a 20 μm step size. Finally, for the purpose of maximizing the number of grains analyzed while minimizing the number of duplicate measurements per grain, samples RM-14 and N251-4 were analyzed with a 100 μm step size. All samples analyzed are from roughly the center of the RLCZ along a NW-SE line, with exception to RM-41, which is near the NE edge of the zone. For the detection of backscatter Kikuchi patterns (Fig 2.9), also known as electron backscatter diffraction patterns (EBSP), the mean angular deviation (MAD) was set to 1.3° for all samples except RM-14 which was allowed a MAD value of 2.0. This number controls the allowable angular deviation of the Kikuchi bands from the expected position for a given mineral phase, in essence allowing for a lesser or greater degree of error in the identification of different mineral phases. For data analysis, including stereonet plotting, the Oxford Labs Channel 5 software suite was utilized.

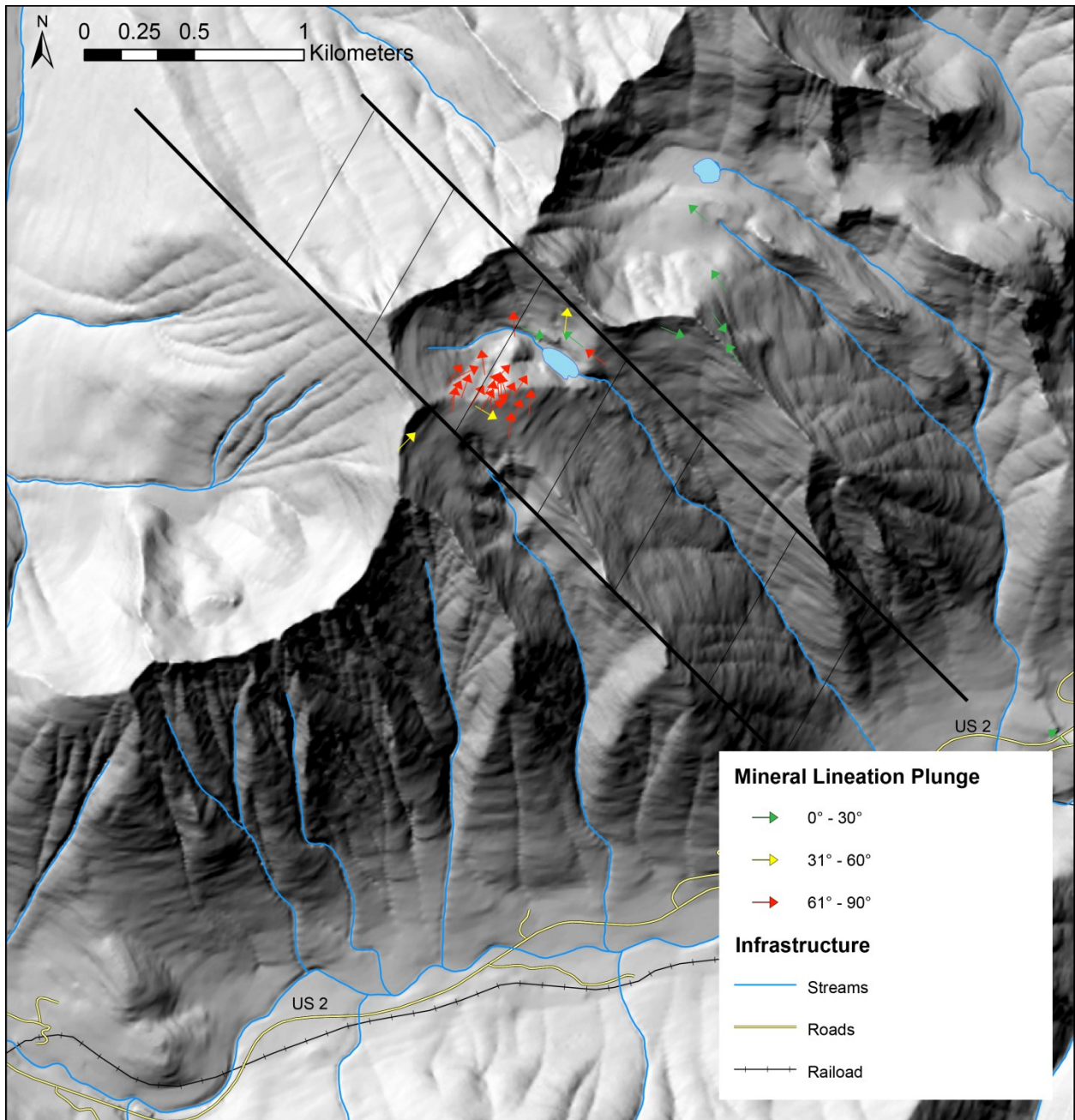


Figure 2.1: An ArcGIS generated hill-shade showing the study area with lineation trend and plunge data. The crosshatched area represents the approximate boundaries of the RLCZ.



Figure 2.2: Image of the “Roly-Poly” from the IRM – one of the machines used for measuring AMS of a rock sample.



Figure 2.3: Image of the KappaBridge from the IRM –used to measure AMS.



Figure 2.4: Photograph of the sample orienting device for the KappaBridge. Rock samples were aligned by hand using this device as a guide.

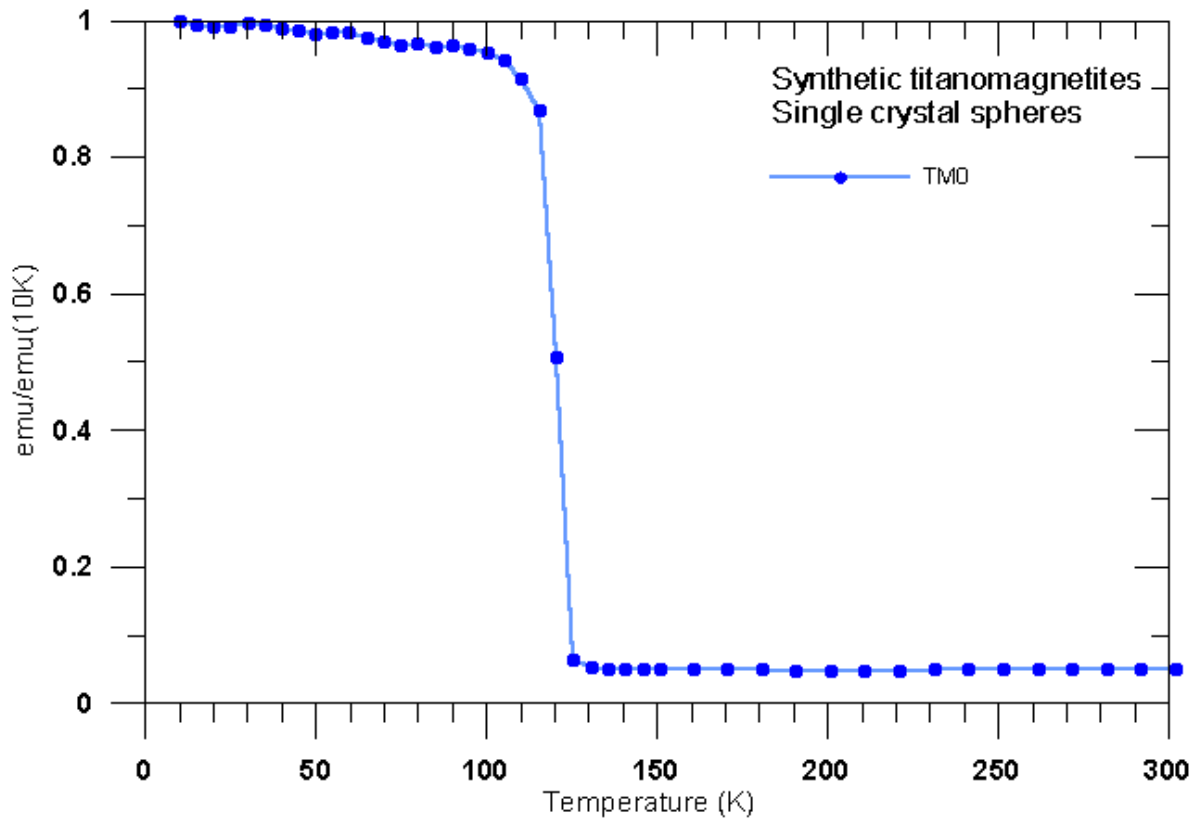


Figure 2.5: Chart showing an example of a known magnetic susceptibility curve for titanomagnetite heating. The temperature at which the drop in magnetic susceptibility occurs is indicative of a titanomagnetite phase. Known curves are used to compare against unknown data to aid in determining mineralogy. Image credit: <http://www.irm.umn.edu/bestiary/>



Figure 2.6: The petrographic microscope used for analyzing thin sections. See text for details.

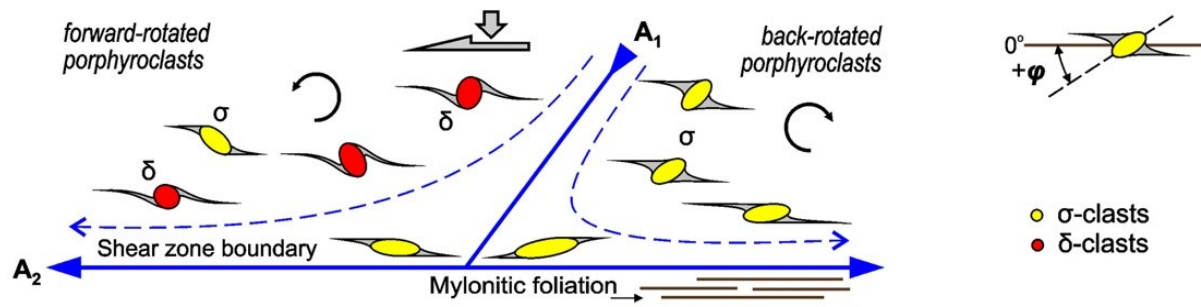


Figure 2.7: Diagram demonstrating how ϕ is calculated for back-rotated and forward-rotated clasts (after Xypolias, 2010).

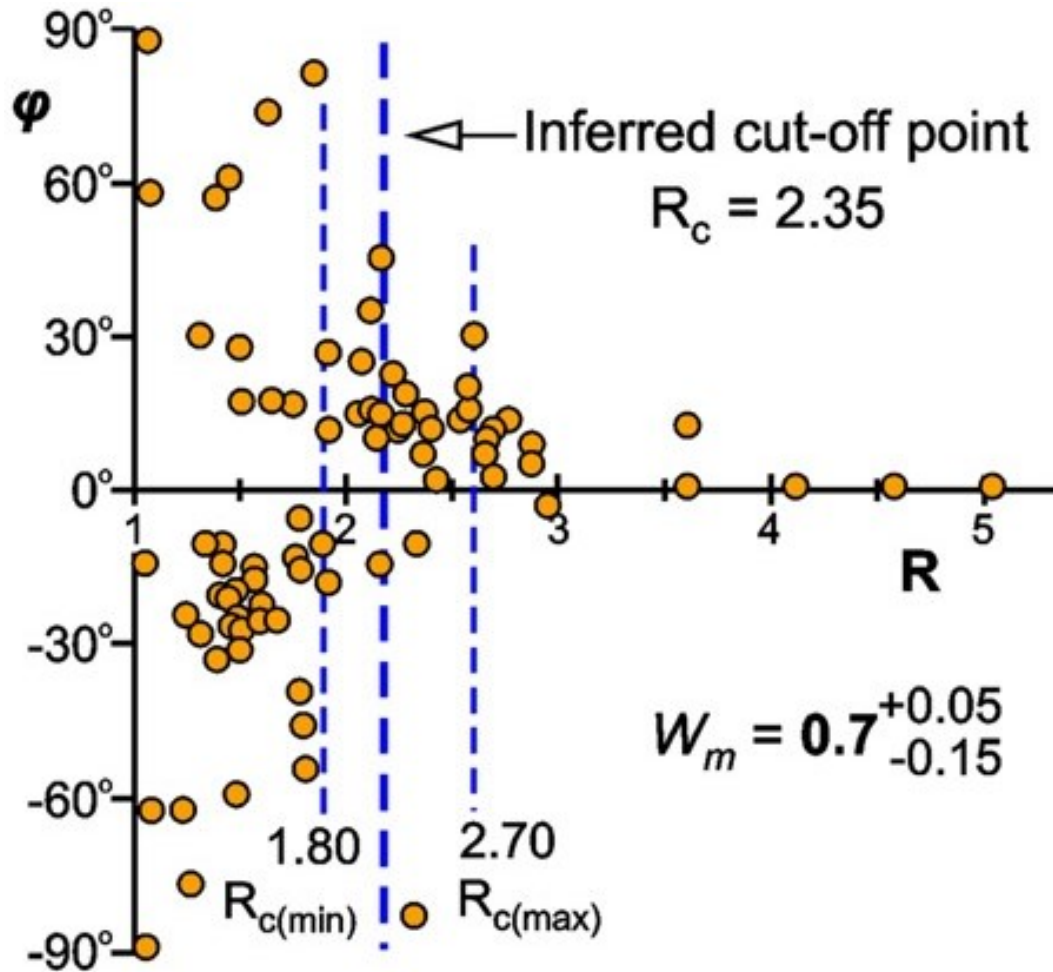


Figure 2.8: Diagram demonstrating the PAR method as modified by Wallis et al., 1993. Note that for R_c a range is given, determined by the inferred cut-off point between infinitely and finitely rotating clasts (from Xypolias, 2010).

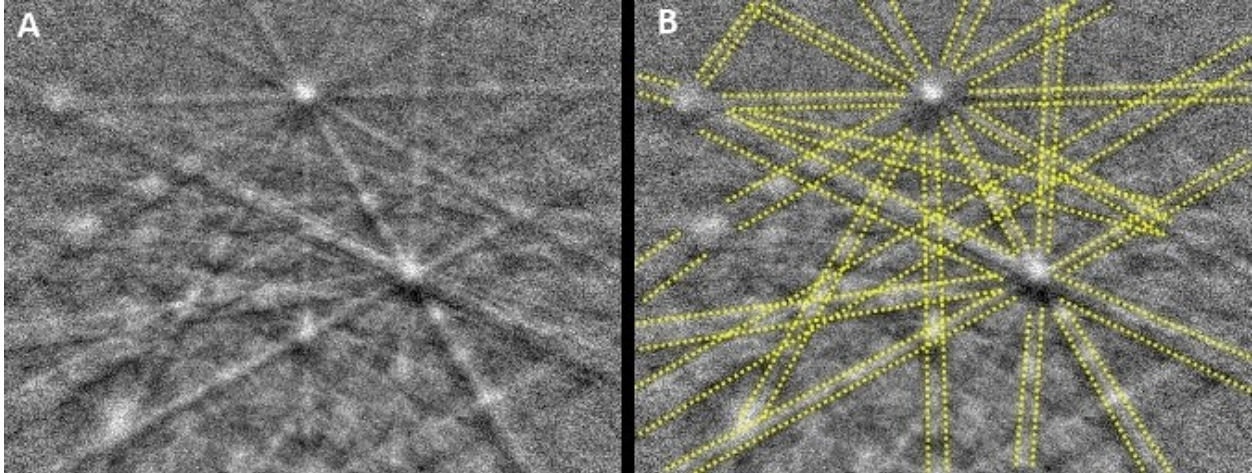


Figure 2.9: Image of a Kikuchi pattern. 'A' represents the unprocessed image. 'B' shows how the software detects and indexes the bands. Angles between Kikuchi bands are measured to identify the mineral phase and orientation of the crystal at a given spot.

3. Results

3.1. Field work and structural data

3.1.1. Petrology

3.1.1.1. Schist

The amphibolite-facies Chiwaukum Schist on Nason Ridge may be subdivided into a dark pelitic schist and medium to light-gray semipelitic schist. Both types contain biotite, quartz, plagioclase, minor muscovite, garnet, and accessory minerals. Additionally, both schist types contain thin quartz-rich layers which aid in highlighting the outcrop-scale structures (Fig. 3.1). In hand sample, generally only the latest foliation (S_3) is evident. Although the schist is intruded by the MSB on Nason Ridge, no obvious indications of contact metamorphism were found along the southwest side of the area closest to the batholith.

Also present are amphibolite-bearing schists with quartz, hornblende, plagioclase, and varying amounts of garnet and biotite. The dark amphibole bearing schist acts as an important lithologic marker within the otherwise continuous pelitic schist, and parentage of this schist is believed to be calcareous pelites, marls, and/or tuffaceous siltstones (Magloughlin, 1986, p.82).

3.1.1.2. Orthoamphibolite

Orthoamphibolites derived from basaltic marine volcanic flows have been reported in the Settler Schist (Lowe, 1972) and Chiwaukum Schist (Magloughlin, 1986, p. 83). These units are oriented parallel to S_3 and are cut by metatonalite. The primary constituents are hornblende, plagioclase, and quartz. Garnet, biotite, zoisite, and oxides are also present in varying amounts.

3.1.1.3. Metatonalite

Sill-like and generally metamorphosed and deformed tonalitic intrusions tend to follow the foliation of the schist, and are locally folded, although the lack of internal markers and the high degree of recrystallization obscure the degree to which deformation has occurred on these intrusive bodies.

The metatonalite on Nason Ridge is generally only weakly deformed compared to the schist and quartz veins. The metatonalite is variably deformed on Nason Ridge, but is generally concordant with the zone. The metatonalite is foliated and lineated similarly to the Chiwaukum Schist, having undergone the same D_3/D_4 event.

Metatonalite ranges from mm-scale veinlets to thick sill-like masses up to 5 meters thick that run for several hundreds of meters across the cirque, but collectively the metatonalite makes up only a small percentage of the rock within the zone.

3.1.2. Structural geology

3.1.2.1. Foliation

The orientation of foliation within, at the boundaries, and outside the RLCZ is fairly consistent, agreeing with previous observations (Getsinger, 1978; Magloughlin, 1993; Miller et al., 2006). The dominant foliation, originating from the D_3 event of Magloughlin (1993), strikes primarily NW-SE and dips on average 80° NE (Figs. 3.2 & 3.3). Poles to planes (Fig. 3.2) show a very tight clustering, emphasizing the consistent and steeply dipping orientation of the foliation.

3.1.2.2. Folds

Due to the lack of stratigraphic markers and the geometric complexity of the folding due to at least four major deformational events, tracing folds is normally impossible. D_3/D_4 folds ranging from isoclinal to gentle are common, and are highlighted by the quartz veins that are commonly <2 cm thick.

Folds maintaining a relatively consistent thickness across the folded surface (class 1B parallel folds) are present, although the majority of folds are similar (class 2) and class 3 folds, which are characterized by thickening at the fold hinge (Figs. 3.4 & 3.5). The similar folds may have a different origin than the dominant parallel folds, indicating different tectonic processes occurring at different times.

Fold hinge measurements show that the majority of the local hinges have been reoriented from the regional NW-trending subhorizontal orientation into a NW-trending subvertical orientation, forming a NW-SE girdle with a best-fit girdle calculated at 313-86 (i.e., 133 86N, Fig. 3.6). A scatterplot of the hinge line plunges across the zone indicates a steepening progression to the SW, in the direction of the MSB (Fig. 3.7).

Floating fold hinges are prevalent throughout the RLCZ, indicating a high degree of strain (Fig. 3.1). Equally prevalent are asymmetric folds (Fig. 3.8). In combination, these features may imply at least some degree of simple shear, potentially caused by flexural flow and/or passive folding or refolding (Bell and Hammond, 1984; Carreras et al., 2005; Fossen, 2010), however, a robust interpretation would require detailed analysis of fold vergence and orientation. In addition, sheath folds are present (Fig. 3.9) which aid in determining the displacement direction in cases where simple shear is present (Hudleston and Treagus, 2010). Magloughlin (1993) also reported the presence of sheath folds.

3.1.2.3. Mineral lineations

Mineral elongation lineations (MELs) are another prevalent structural feature in the RLCZ. The majority of data were collected from rocks containing prismatic amphiboles and to a lesser extent from biotite grains. To a lesser extent, the long axes of quartz stretching lineations were also measured. MEL orientations are similar to the orientations of fold hinge lines. However, in contrast to hinge lines, mineral lineations clustered more tightly in the NW-trending subvertical orientation, rather than fanning out along a NW-SE girdle (Fig. 3.10). This would seem to indicate that the lineations are not b-lineations

as has been proposed, but may be newly developed lineations formed close to their present orientation. Also in common with the hinge lines, mineral lineations tend to steepen to the SW in proximity with the MSB (Fig. 3.11).

3.1.2.4. Boudinage

Quartz veins within the schist are invariably boudinaged on some scale, with the boudins in the same plane as the regional foliation. This relationship indicates that there has been shortening perpendicular (or oblique) to the foliation. Additionally, many of the boudins are asymmetric (Fig. 3.12), suggesting transpressive deformation forces (Goscombe, 2003). The metatonalite intrusions, however, are not commonly boudinaged, suggesting that they intruded after (or at the end of) significant flattening.



Figure 3.1: Photograph showing the dark pelitic schist with interspersed quartz veins helping to highlight the outcrop-scale structures. Several floating/rootless fold hinges are present. Rock hammer for scale. Photograph orientation: 56→295.

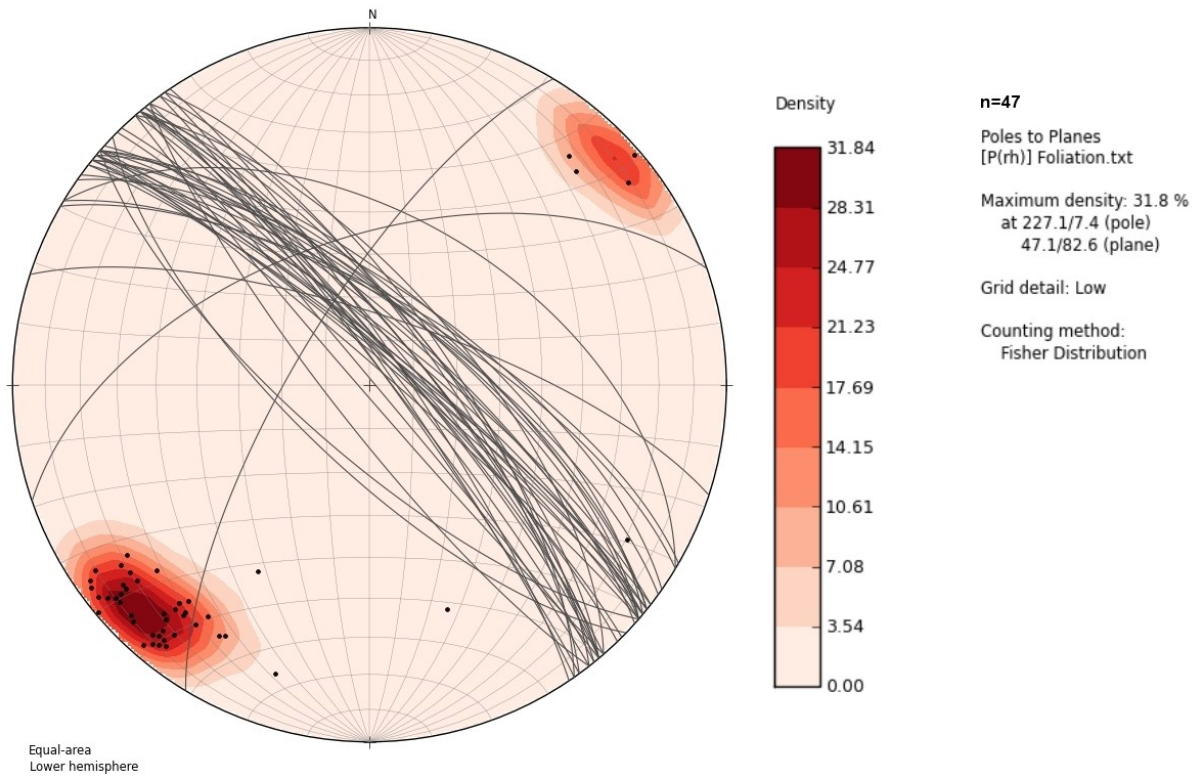


Figure 3.2: Contoured stereonet showing great circles and poles for foliation. Mean plane is 314-79 with mean pole at 11→224.

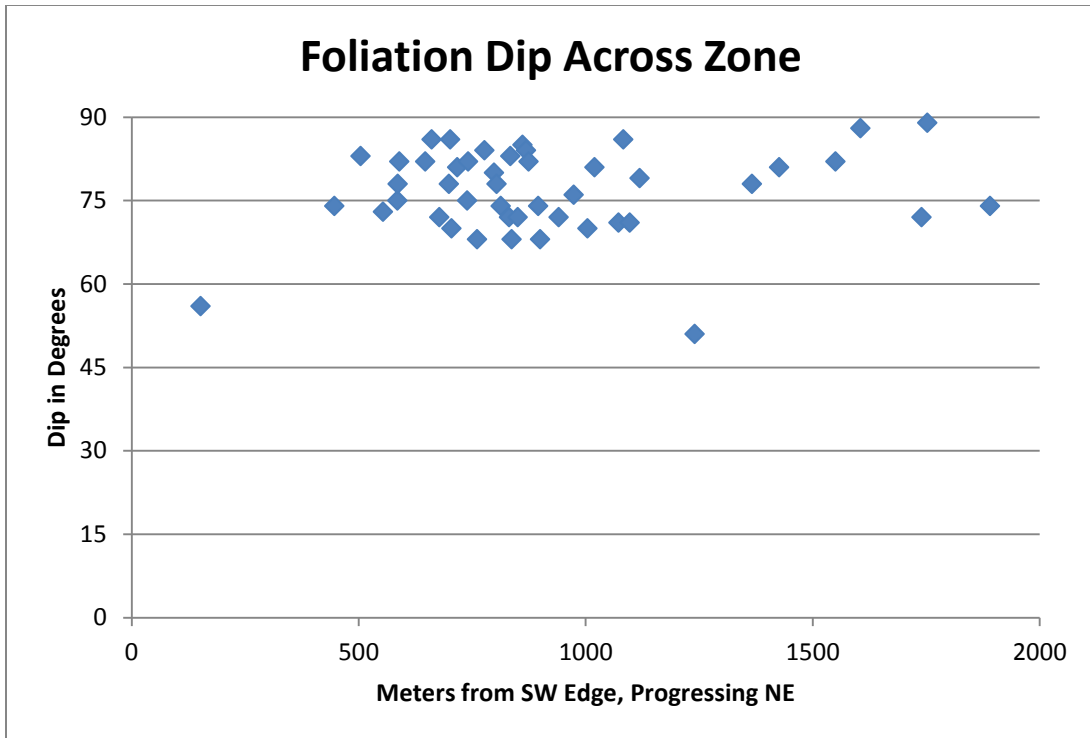


Figure 3.3: Scatterplot showing the dip of the foliation with distance across the study area.



Figure 3.4: Folded quartz vein showing a fairly consistent thickness across the folded surface, forming a class 1B or parallel fold. Photograph orientation: 72→331.



Figure 3.5: Photograph of folds showing variable thickness from hinge to limb. Thicker fold hinges indicate class 2 (similar) or class 3 (those with diverging isogons) folds. Orientation: 56→283.

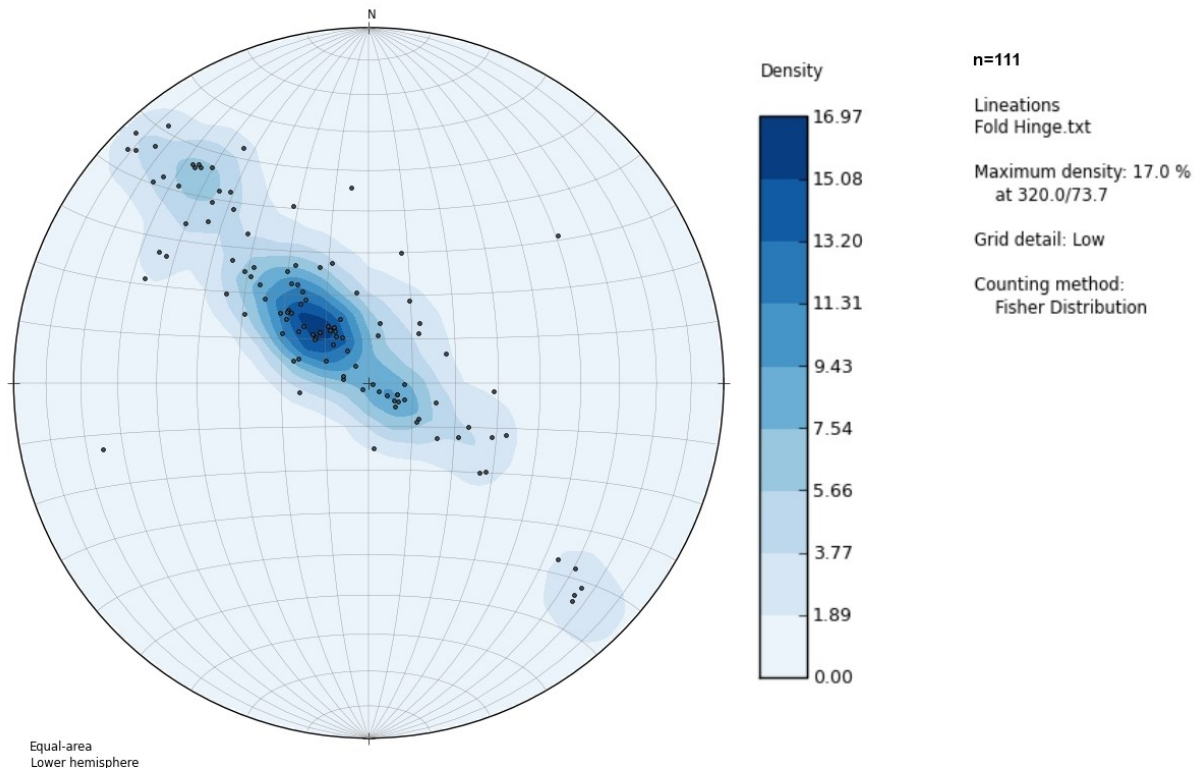


Figure 3.6: Stereonet of fold hinge lines (dots) showing a dominant, subvertical, NW orientation with a NW-SE oriented girdle. Girdle best fit plane is oriented 313-86. Mean point is 69→324.

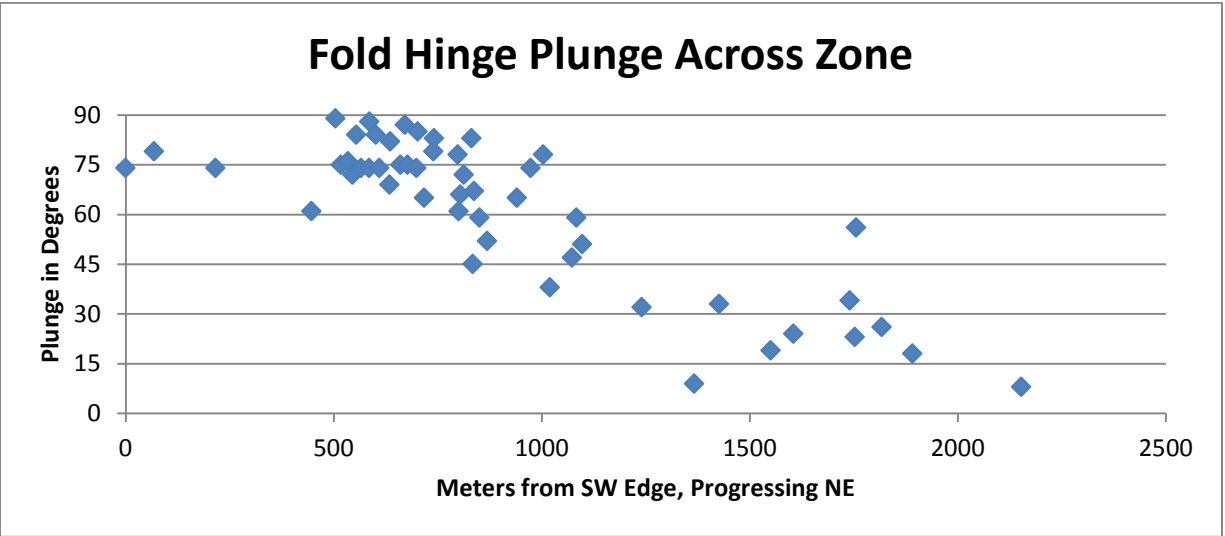


Figure 3.7: Scatterplot of hinge line plunges across the RLCZ.



Figure 3.8: Photograph of asymmetric folding in a quartz vein within the schist. Ruler is 15 cm long. Photograph orientation: 74→216.



Figure 3.9: Photograph taken of a sheath fold with dime for scale. Photograph orientation: 74→000.

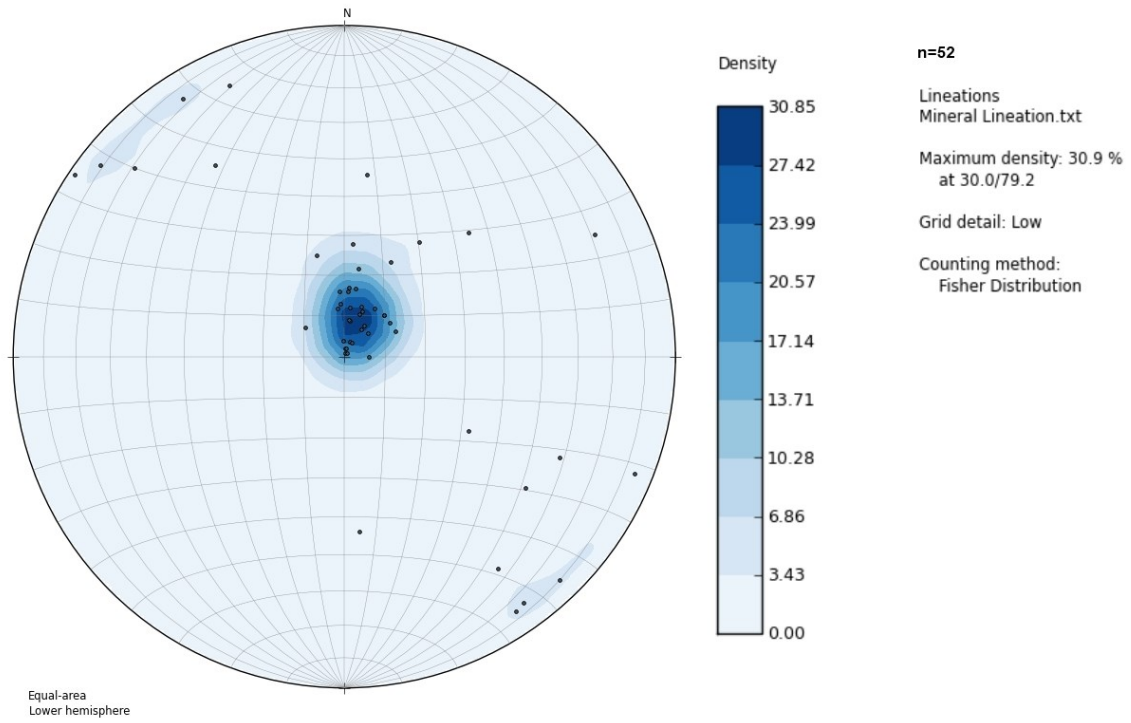


Figure 3.10: Stereonet of mineral lineations (dots) within and immediately adjacent to the RLCZ. Mean is 78→026.

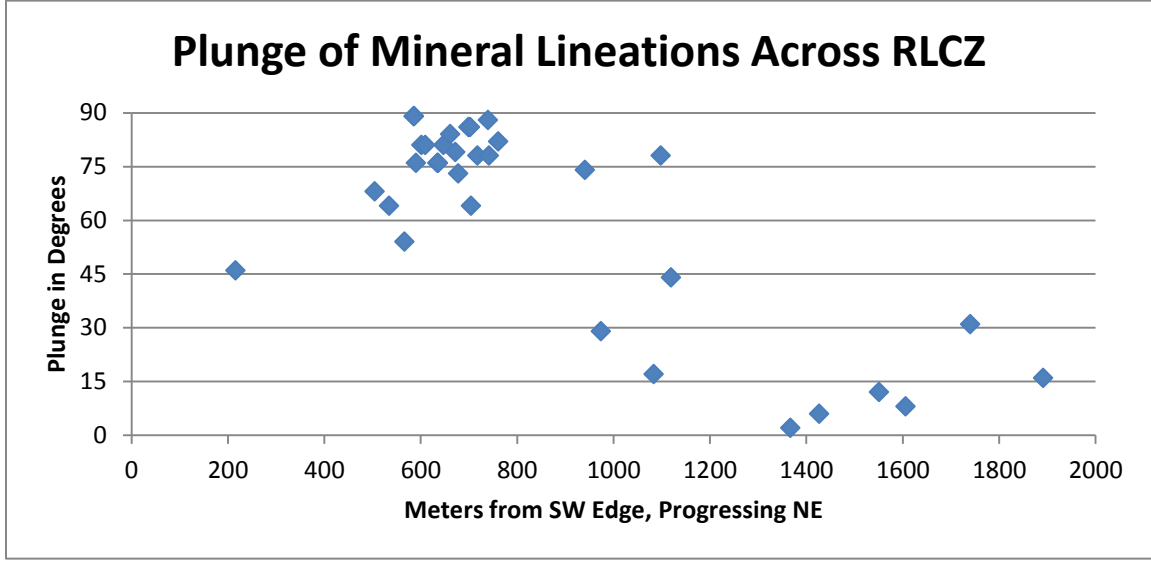


Figure 3.11: Scatterplot illustrating a steepening trend of mineral lineations to the SW, across the RLCZ. The 'O' line is oriented NW-SE.



Figure 3.12: Photograph of asymmetric quartz boudins within the Chiwaukum Schist. Orientation: 75→224.

3.2. Analytical Results

3.2.1. Magnetic data

3.2.1.1. Room temperature AMS

The magnetic data collected includes 1) the susceptibility in μSI (units of Henry/meter) for the maximum, intermediate, and minimum eigenvectors; 2) the lineation parameter L , calculated as the maximum eigenvalue/intermediate eigenvalue; 3) the foliation parameter F , calculated as the intermediate/minimum eigenvalue; 4) the corrected degree of anisotropy P_j ; 5) the shape factor T ; 6) the declination of the minimum and maximum eigenvector *in situ* denoted as D_{\min} (*in situ*) and D_{\max} (*in situ*) respectively; and 7) the inclination of the minimum and maximum eigenvector *in situ* denoted as I_{\min} (*in situ*) and I_{\max} (*in situ*) respectively. The spatial orientations of the maximum, intermediate, and minimum directions of magnetic susceptibility are also commonly given as K_{\max} , K_{int} , and K_{\min} . These parameters together are referred to as the principle susceptibility axes (Jelinek, 1981).

Lineation and foliation orientations for each sample have been plotted on stereonet to show spatial relations for individual and among samples (Figs. 3.13 through 3.18).

The magnetic lineation stereonet (Fig. 3.13) shows a girdle along a NW-SE orientation with the largest number of samples showing subvertical orientations. Statistical analysis within the program "OpenStereo" yields a best-fit girdle at 309-81. Figure 3.14 shows the same lineation data with statistical bootstrapping applied. Bootstrapping is a resampling technique which, in this case, calculates what a statistically normalized data set of n points would look like. It does this by taking a random sampling of points, calculating their mean, plotting the result, and repeating that process a designated number of times. For the given dataset, the number of repetitions was kept at the IRM default value of 1000. Because the statistical technique produces random data, it is used here primarily as a visual aid for better understanding the distribution of the magnetic lineation. The mean and normalized mean for the

magnetic lineation data are calculated as 71→345 and 79→001, respectively. Additionally, Fig. 3.15 shows the error ellipses for the magnetic lineation data.

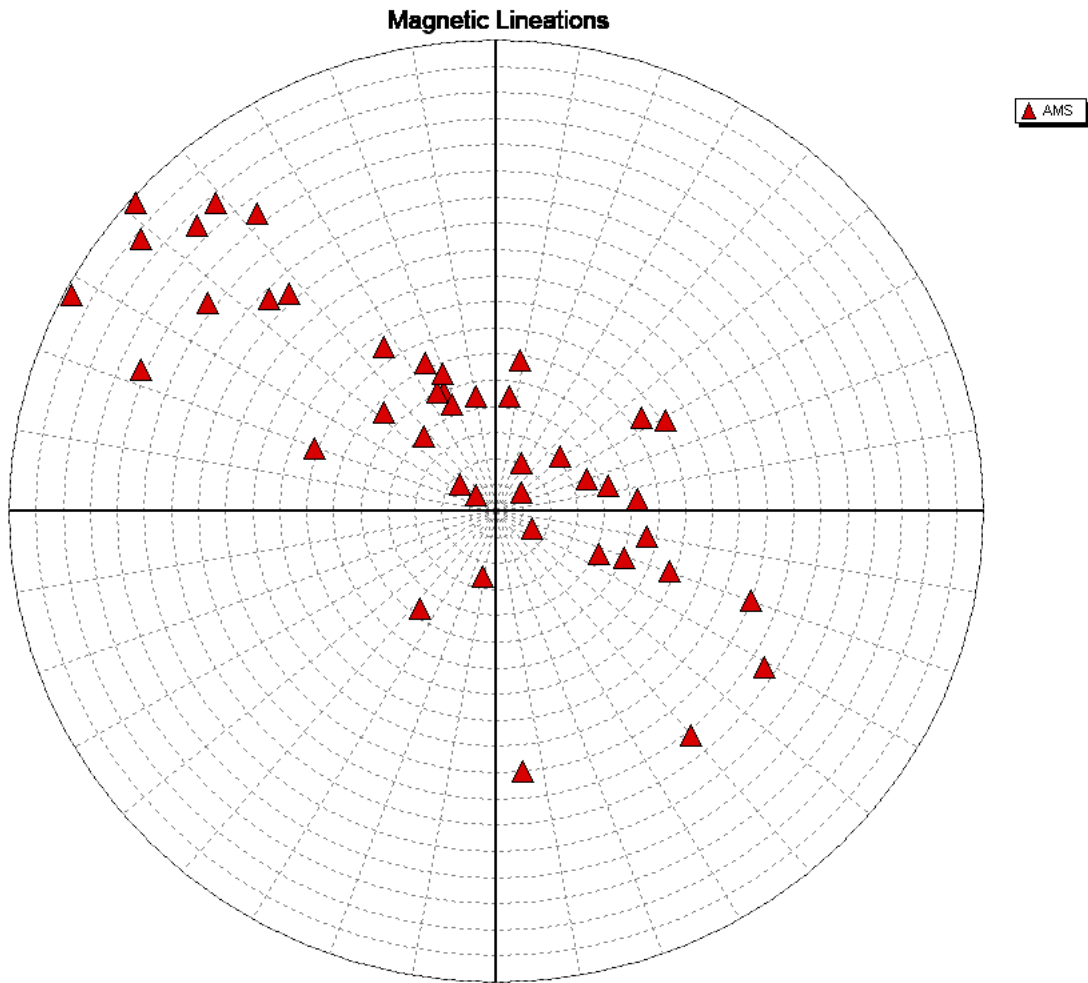


Figure 3.13: A stereonet showing magnetic lineation orientations. Red triangles show individual samples from various localities across Nason Ridge. Best-fit girdle is 309-81.

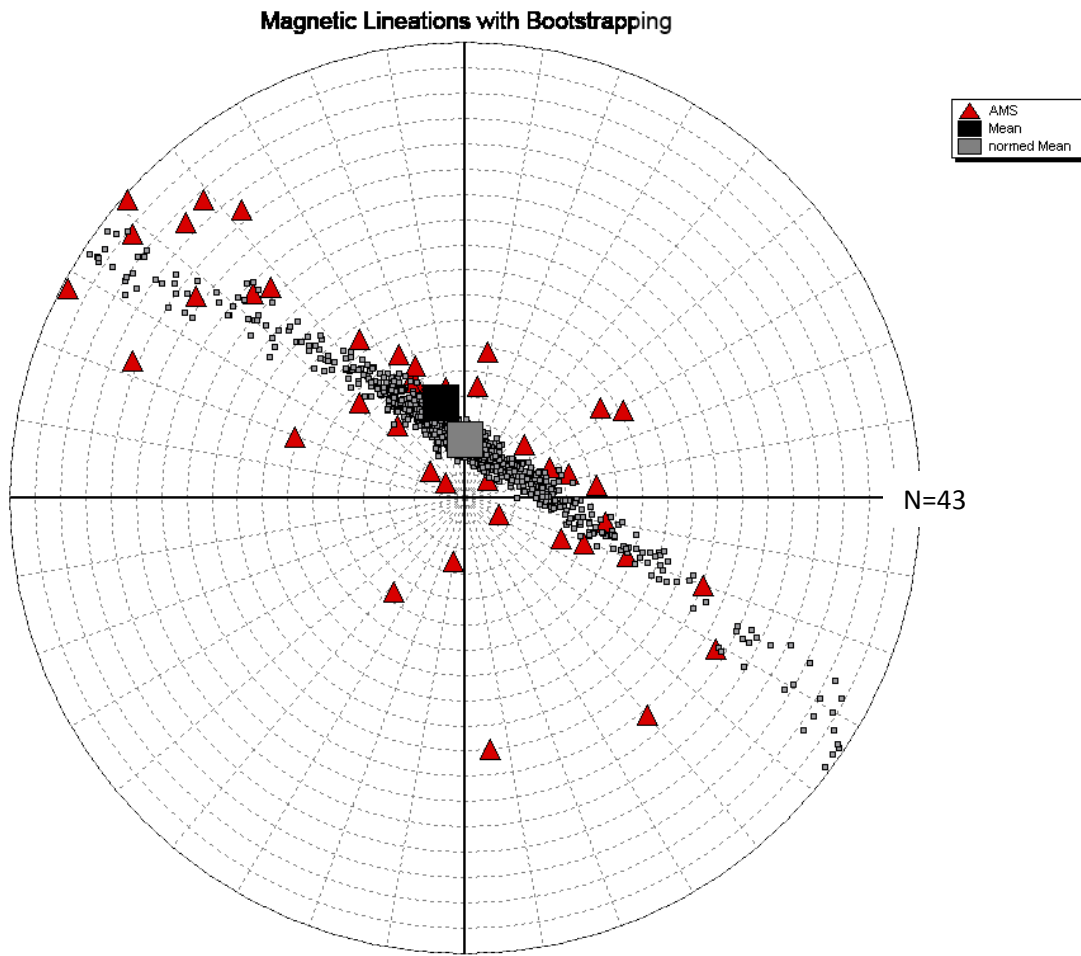


Figure 3.14: A stereonet of magnetic lineation orientations with means and bootstrapping applied. The black box indicates the mean value (71→345), and the gray box indicates the mean normalized for error (79→001).

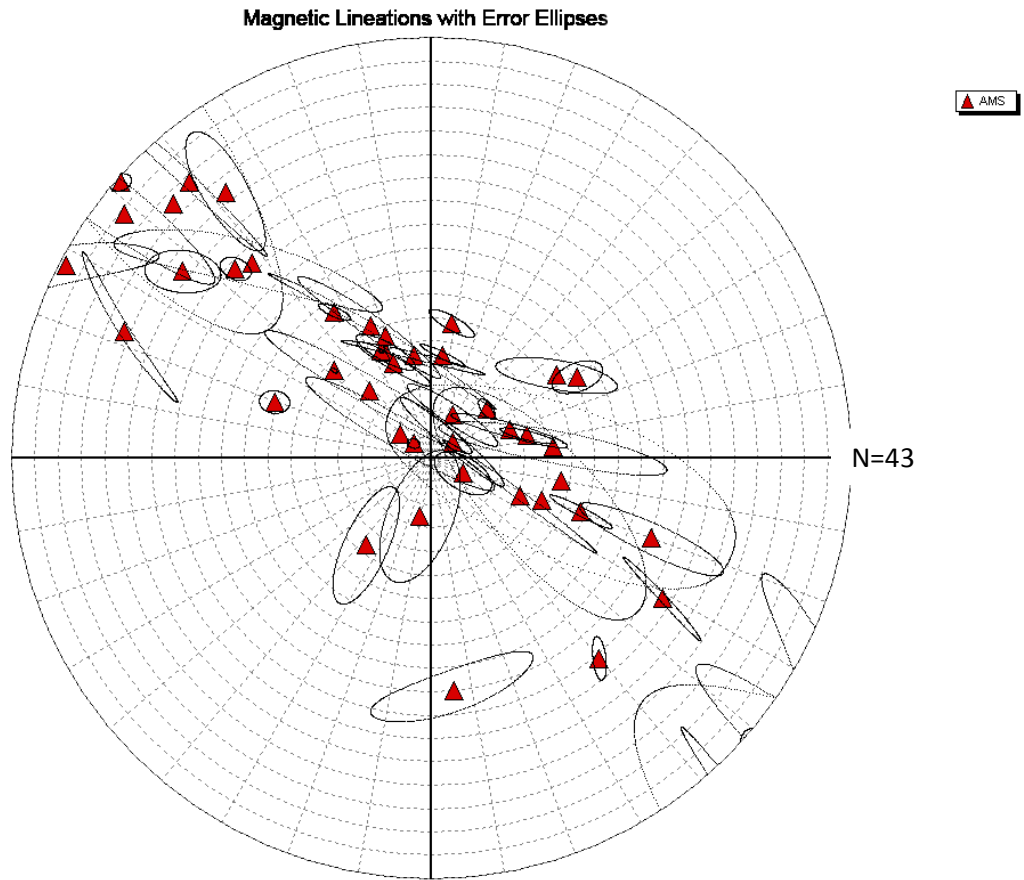


Figure 3.15: A stereonet of magnetic lineation orientations with error ellipses (black circles) applied.

The magnetic foliation is plotted as poles to planes (Fig. 3.17), and shows the foliation as strongly concentrated with a steep dip striking NW. The mean and normed mean are 13→217 and 10→211 respectively. Bootstrapping, shown in Fig. 3.18, again helps to demonstrate the concentrated nature of the data. Error ellipses for the magnetic data have been applied in Table 3.19.

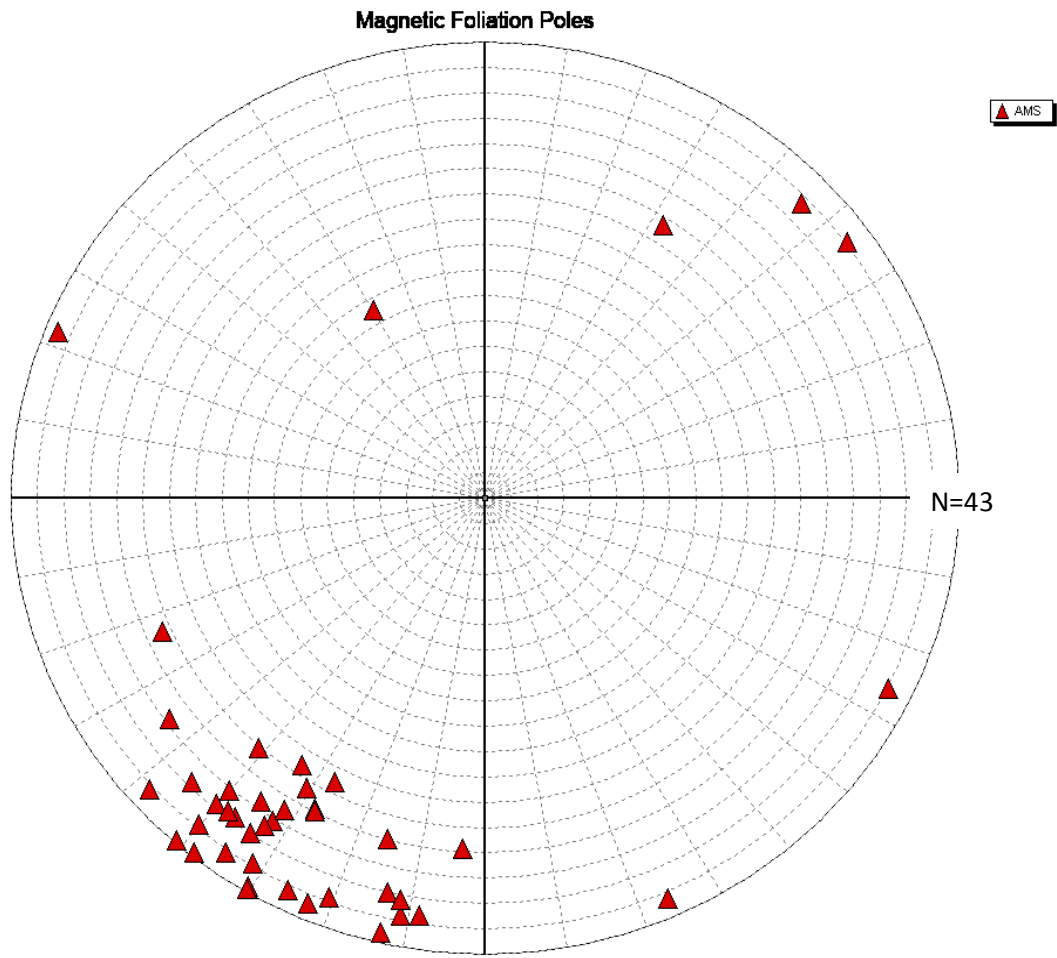


Figure 3.16: A stereonet showing poles to magnetic foliation planes. Red triangles show individual samples from various localities across Nason Ridge.

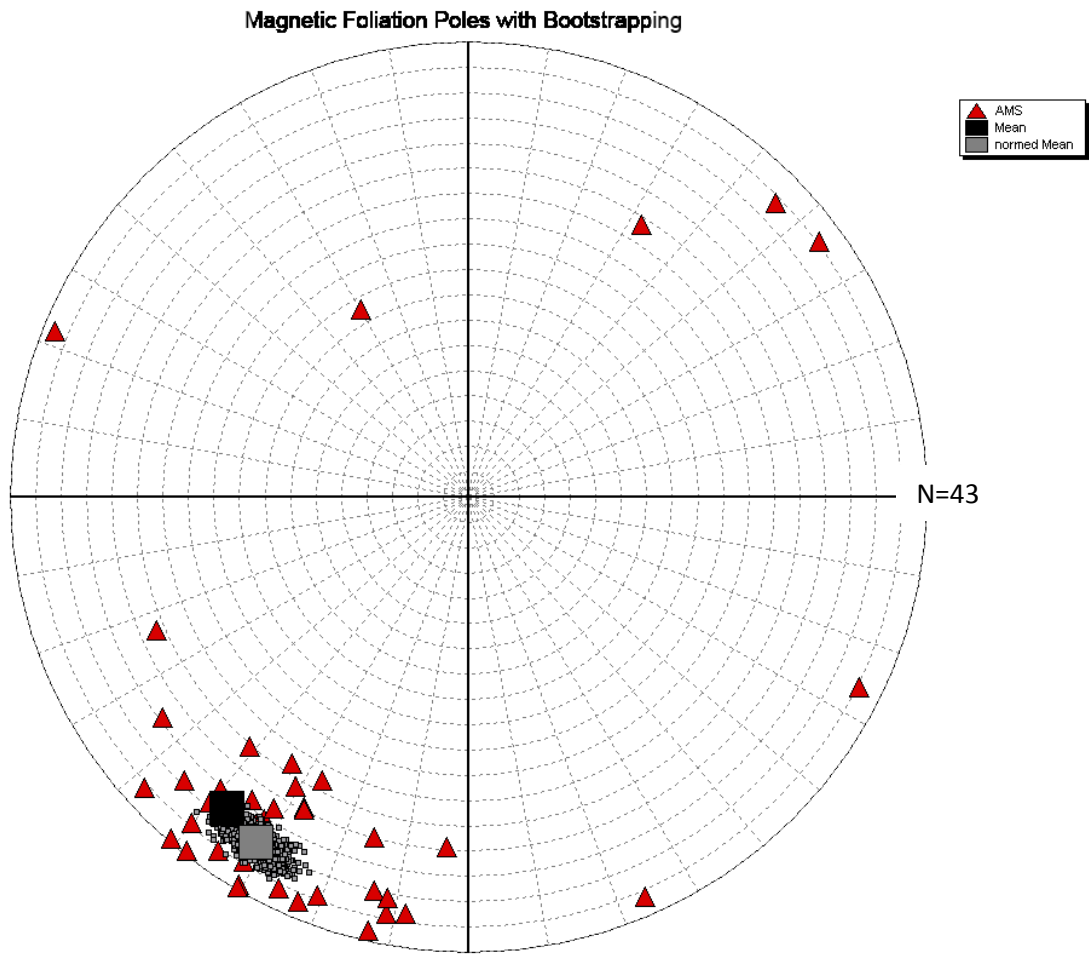


Figure 3.17: A stereonet of poles to magnetic foliation planes with means and bootstrapping applied. The black box indicates the mean value (13→217), and the gray box indicates the normed mean (10→211).

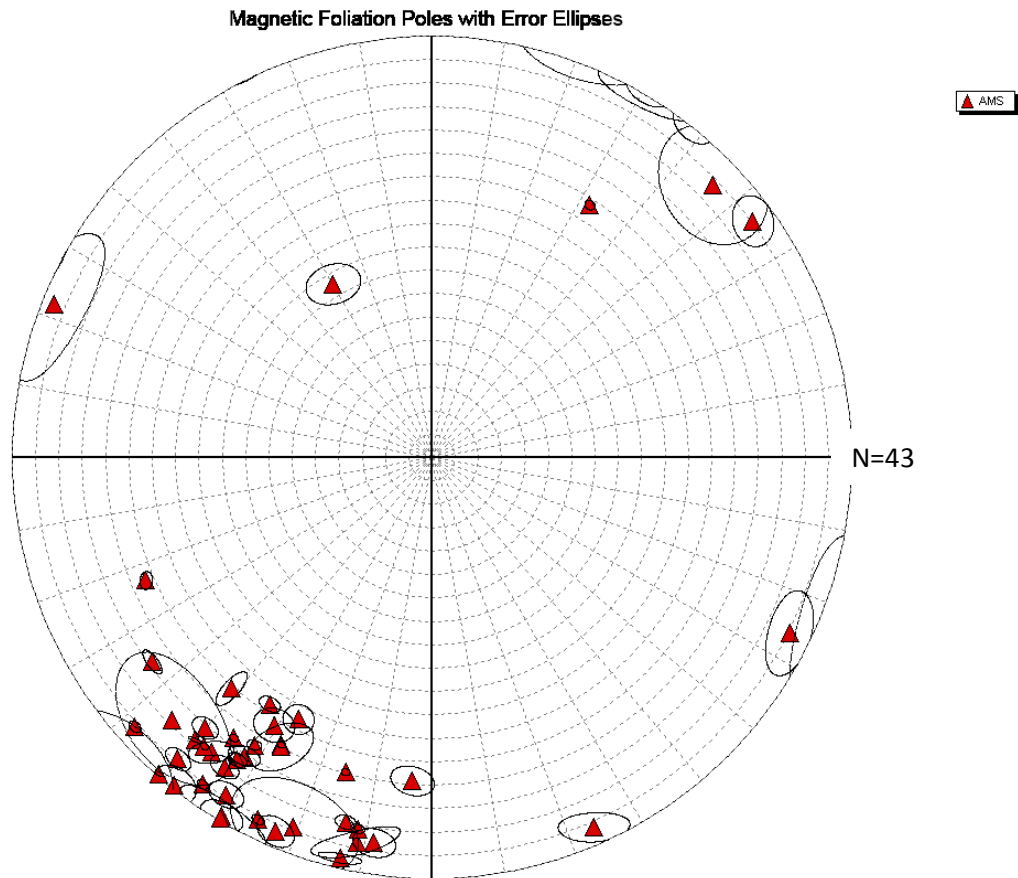


Figure 3.18: A stereonet of poles to magnetic foliation planes with error ellipses (black circles) applied.

A comparison between the AMS data and structural data reveals several similarities (Table 3.19). Both the magnetic and structural lineations show a concentration steeply plunging to the north. Additionally, the best-fit girdle for the fold hinges (313-86) is similar to the best-fit girdle for the magnetic lineations (309-81). The orientation of the magnetic girdle created by the magnetic lineations is similar to the orientation of the structural foliation, demonstrating that the individual grains creating the magnetic lineations are within the same plane as the foliation. Like the magnetic foliation, the local structural foliation is oriented in a NW-SE subvertical plane (Fig. 3.6). The agreement between field measurements and magnetic analyses indicates that the minerals responsible for the regional metamorphic fabric are either the same, or in the same orientation, as the minerals defining the

magnetic foliation. Additionally, it should be noted that outlier data points are more quartz rich metatonalites and quartz veins.

Principle susceptibility orientation data may be visualized as an ellipsoid, with the principle K components forming the axes (Fig. 3.20) (Pares and van der Pluijm, 2002). Plotting the lineation parameter (L) against the foliation parameter (F) creates the AMS analog to a Flinn Diagram (Fig. 3.21). As in a Flinn Diagram, the upper field represents prolate ellipsoids, and the lower field represents oblate ellipsoids. The points plotted are very near the 1:1 (plane strain) line, though the majority tend to be slightly into the flattening (oblate) field. It is generally agreed that although magnetic data of this type are not quantitatively identical to traditional strain measurement methods, they qualitatively demonstrates the same properties in that an oblate magnetic spheroid is representative of flattening (Aubourg et al., 2000).

Table 3.19: Table comparing field data and magnetic data.

	Mean Foliation (pole)	Mean Lineation	Lineation Girdle
Field Data	11→224	78→026	313-86
Magnetic Data	10→211	79→001	304-82

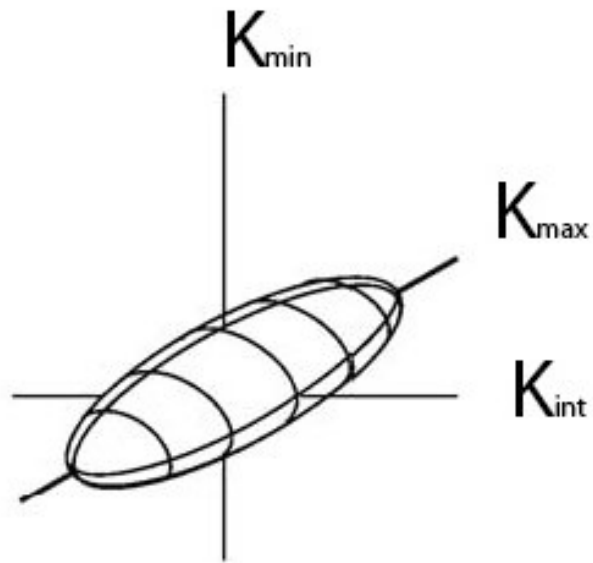


Figure 3.20: Visualized AMS ellipsoid showing the principle K orientations (after Pares, 2002).

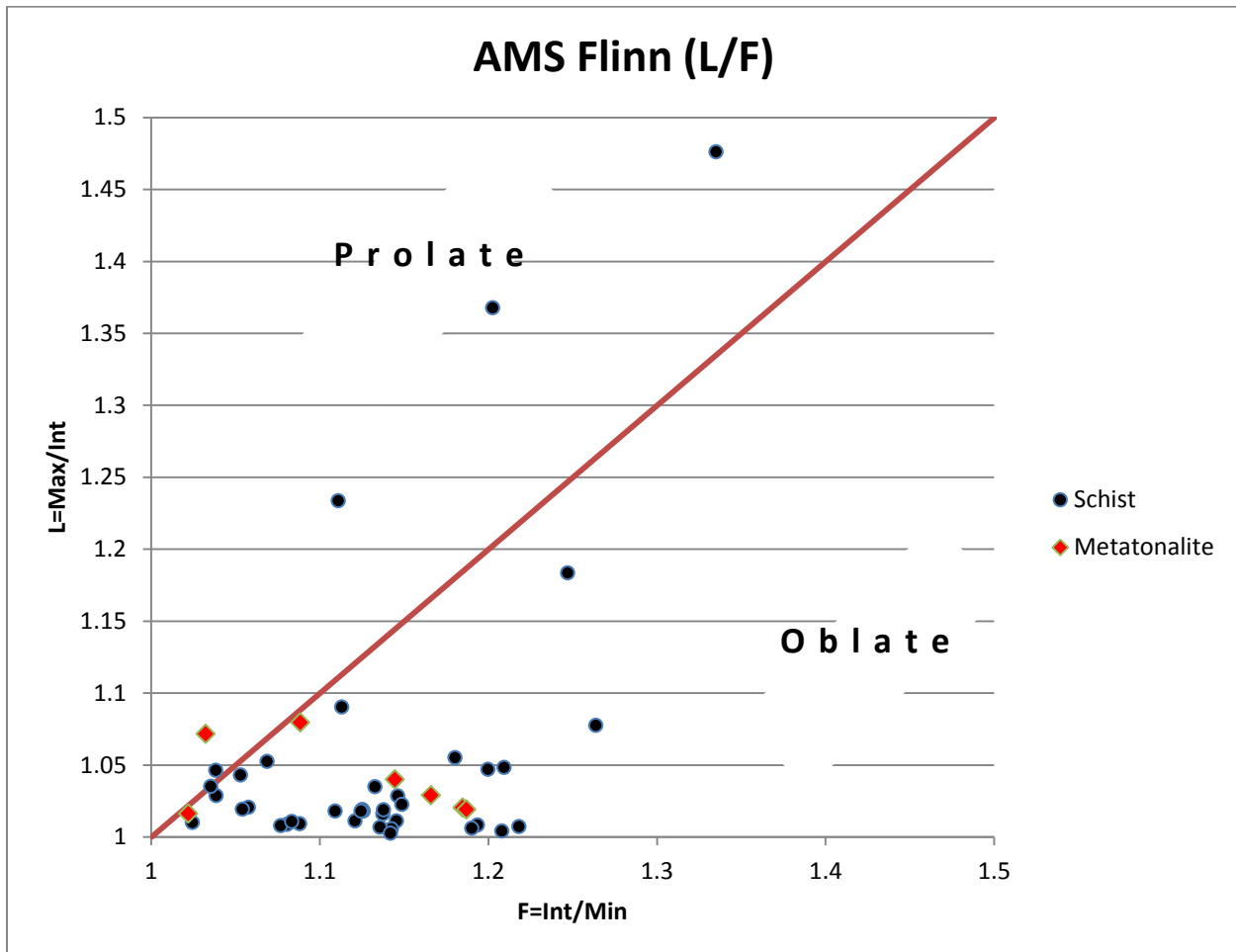


Figure 3.21: Flinn Diagram analog from AMS data. The red line indicates a 1-to-1 relationship (plane strain). The “L” parameter (y-axis) is the ratio of the magnitude of K_{\max} and K_{int} . The “F” parameter (x-axis) is the ratio of K_{int} and K_{\min} . Diagram shows 43 analyses.

3.2.1.2. High temperature magnetic susceptibility

Because analyses done on the high temperature kappa-bridge use a powdered sample, the data collected are much simpler due to the lack of any directional component. The only data collected are the degree of susceptibility as a function of temperature. Thus, the data are best presented as graphs, e.g., Fig. 3.22. In such figures, the red line represents magnetic susceptibility while the sample is heated, whereas the blue line represents susceptibility while the sample is cooling back to room temperature.

By comparing the graphs from Fig. 3.22 to magnetic data from well-constrained samples, the type of magnetism (either ferromagnetic or paramagnetic) can be determined, which in turn is used to infer the mineralogy that produces the magnetic signature. The majority of the high temperature data indicate a dominantly paramagnetic signature, which based on the known mineralogy of the Chiwaukum schist, likely originates from the abundance of biotite. This suggests that the AMS data dominantly reflects the anisotropic magnetic fabric of the biotite grains (M. Jackson, personal communication, 2012).

Samples RM-08, RM-11, and RM-40 (Fig. 3.22) show a strong paramagnetic signature with little or no input from ferromagnetic sources. Typically, the heating curve has an overall higher magnetic signature than the cooling due the breakdown of phases at high temperatures. However, it is not unusual for the heating process to create new ferromagnetic phases which then increase the magnetic susceptibility during cooling (Park et al., 2005).

A few samples, however, clearly indicate a ferromagnetic signature which tends to overprint the weaker paramagnetic signature. RM-55 (Fig. 3.22), which has a Curie temperature of approximately 630°C, corresponds to a low-Ti titanohematite (Bascou et al., 2002). The titanohematite solid solution ranges from ilmenite to hematite, and the combination of ilmenite found in thin section along with weathering products may explain the titanohematite magnetic signature (Bascou et al., 2002). RM-21 (Fig. 3.22) displays a shallow slope with a drop at approximately 320°C on heating, which is representative of biotite. However it is thermally unstable which is evident by a final susceptibility which is much higher than the initial, indicating the presence of Fe-bearing phases which formed new magnetite during heating. Finally, RM-31 (Fig. 3.22) has a rather weak and noisy pattern, though it is possible to identify two ferromagnetic phases with Curie temperatures near 580°C, which is indicative of magnetite, and 630°C, which (again) is likely titanohematite (M. Jackson, personal communication,

2012). Inspection of samples RM-55 and RM-31 revealed the presence of weathering. This explains why these two samples had a much stronger titanohematite signature than the other samples.

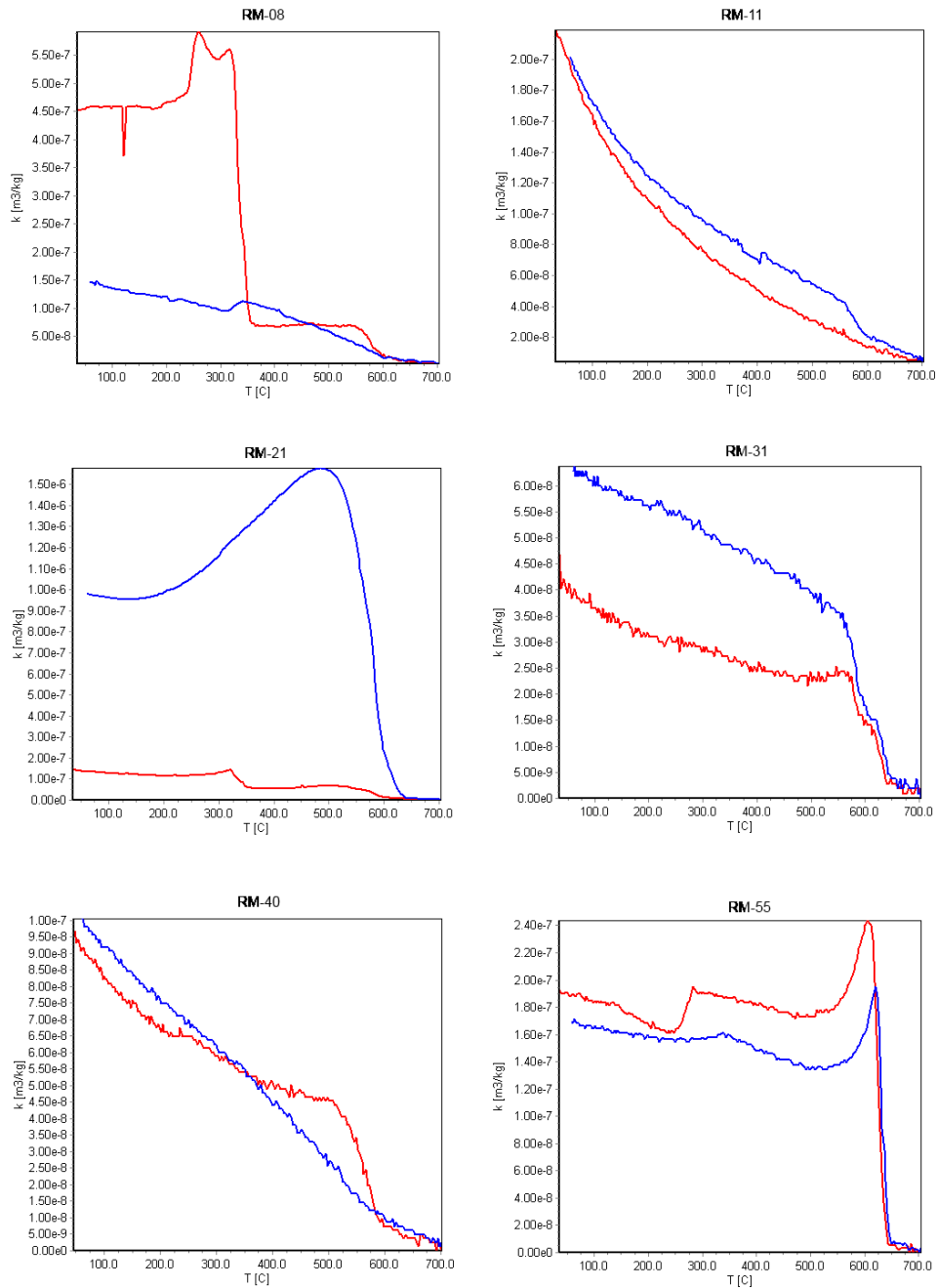


Figure 3.22: Graphs of the magnetic susceptibility versus temperature for six samples of pelitic schist from Nason Ridge. Red curves represent susceptibility during heating, and blue curves show susceptibility during cooling. The y-axis is the measured magnetic susceptibility, and the x-axis is the temperature in $^\circ\text{C}$. Note that the scales of the y-axes are different so that the data can be more easily displayed. The purpose of these plots is to help identify inflection points relative to temperature.

3.2.1.3. Low temperature susceptibility

Very much like high temperature data, low temperature measurements show how magnetic susceptibility varies with temperature. Due to time constraints, only two samples were run using the low temperature technique to compare with the high temperature experiments (Fig 3.23). The data from Fig. 3.23 demonstrates that, as in the case of the high temperature data, the magnetic susceptibility indicates an overwhelmingly paramagnetic source, as seen by the inverse relationship of susceptibility with temperature which is a characteristic indicator of paramagnetic susceptibility (Parés, 2002). This result independently supports the conclusion of a paramagnetic signature drawn from the high temperature data.

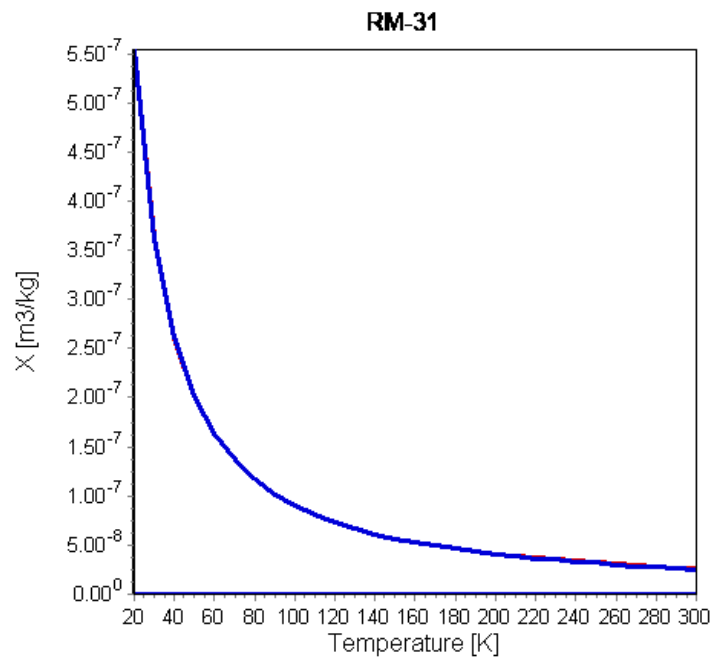
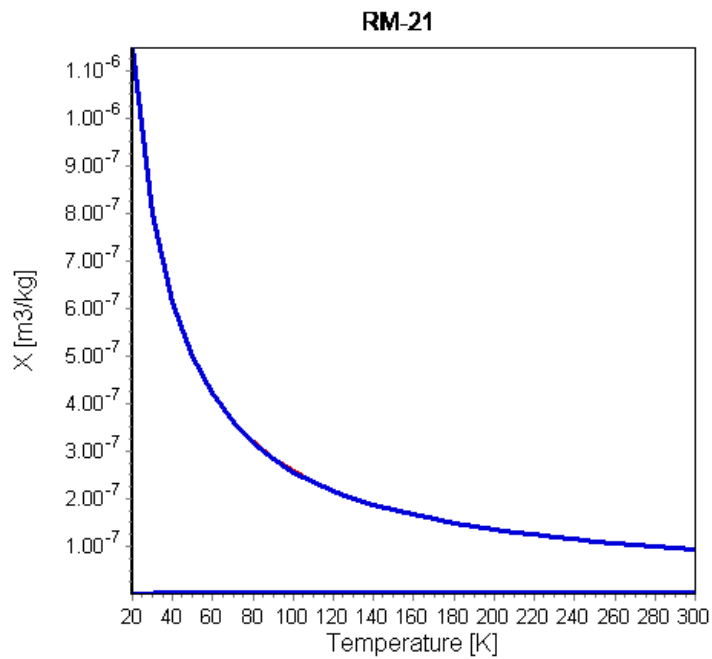


Figure 3.23: Graphs of samples RM-21 and RM-31 using Low T Ferresis measurements showing increasing paramagnetic susceptibility with decreasing temperature. This indicates a primarily paramagnetic source for the magnetic signal. The y axis is the measured magnetic susceptibility, and the x axis is the temperature in Kelvins.

3.2.2. Microscopy

3.2.2.1. Microstructures and fabrics

The foliation in the Chiwaukum Schist is defined dominantly by a preferred orientation of biotite. Quartz and plagioclase is also elongate parallel to foliation to varying degrees (Fig. 3.24). Q domains and M domains range in width from 1–6 mm. Cleavage domains with abundant mica range in volume from 30% – 70% and are parallel to anastomosing.

The foliation of the metatonalite is well developed throughout the RLCZ, continuous in the same orientation as the schist, and defined by biotite and muscovite. Quartz and plagioclase in the metatonalites are noticeably more equant than those in the schist, and plagioclase matrix in the metatonalite lacks albite twinning. Rarely however, larger (>1 mm) plagioclase porphyroclasts preserve magmatic zoning (Fig. 3.25).

Samples commonly display recovery by grain boundary area reduction (Passchier and Trouw, 2005, p. 51) (Fig. 3.26) as well as dynamic recrystallization such as bulging (Passchier and Trouw, 2005, p. 42) (Fig. 3.27).

Mineral lineations in the schist are marked by elongate crystals of biotite and amphibole. Within the metatonalite, the lineation is marked by elongate biotite grains; however the presence of elongate plagioclase porphyroclasts also define the lineation.

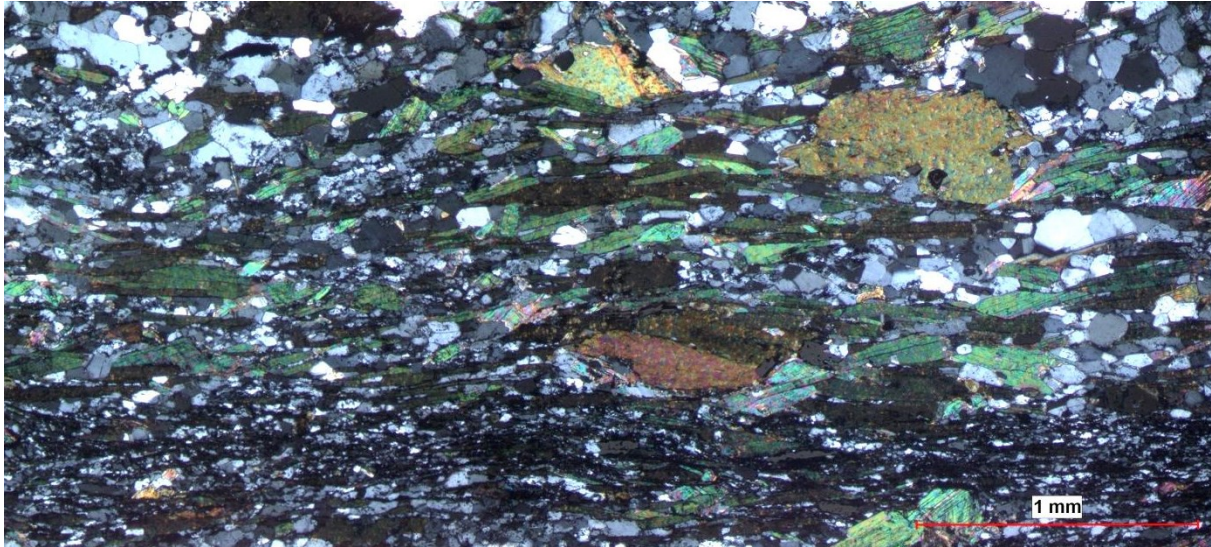


Figure 3.24: Photomicrograph of pelitic schist from the RLCZ showing the foliation defined by biotites and elongate quartz grains. XPL. Sample RC-02. View 00→139; rotated 61° counterclockwise.



Figure 3.25: Photomicrograph showing the preserved magmatic zoning in a plagioclase porphyroclasts with mica inclusions, presumably relict phenocrysts in the metatonalite. XPL. Sample RM-04. View 00→130; rotated 5° clockwise.

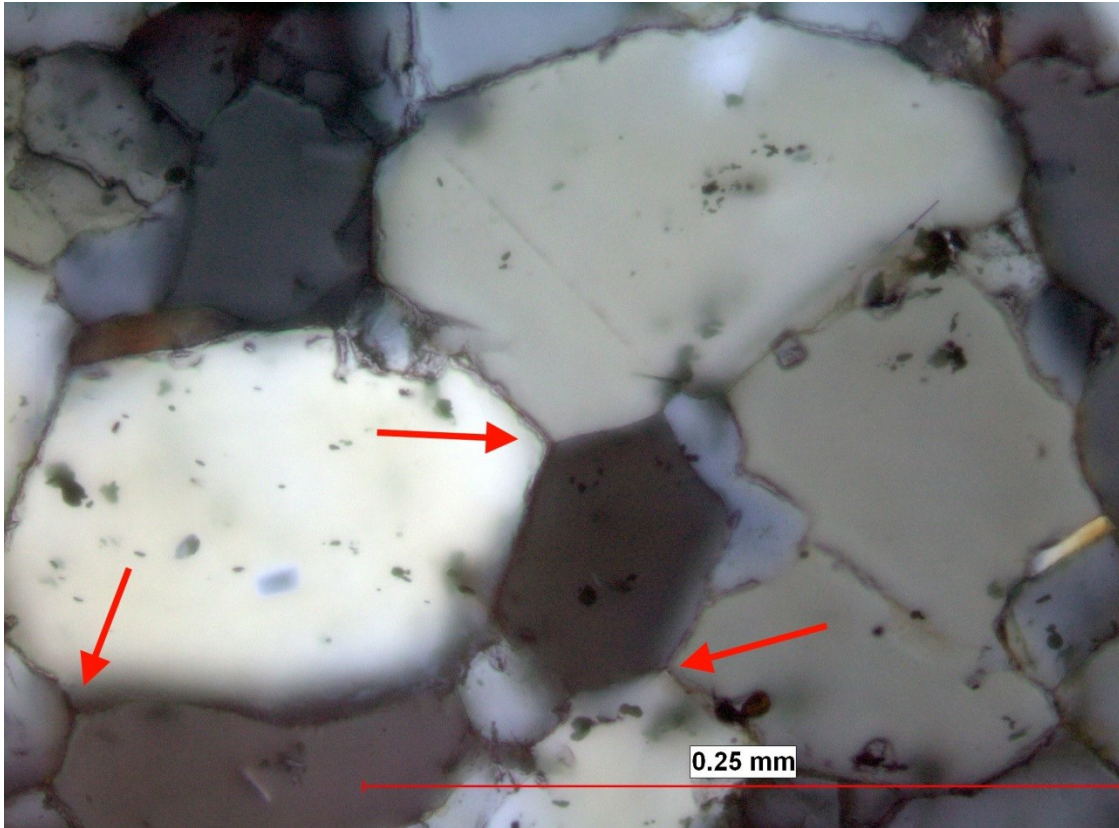


Figure 3.26: Photomicrograph showing grain boundary area reduction as seen by triple junction. XPL. Sample RM-36. View -30→024; rotated 113° clockwise.

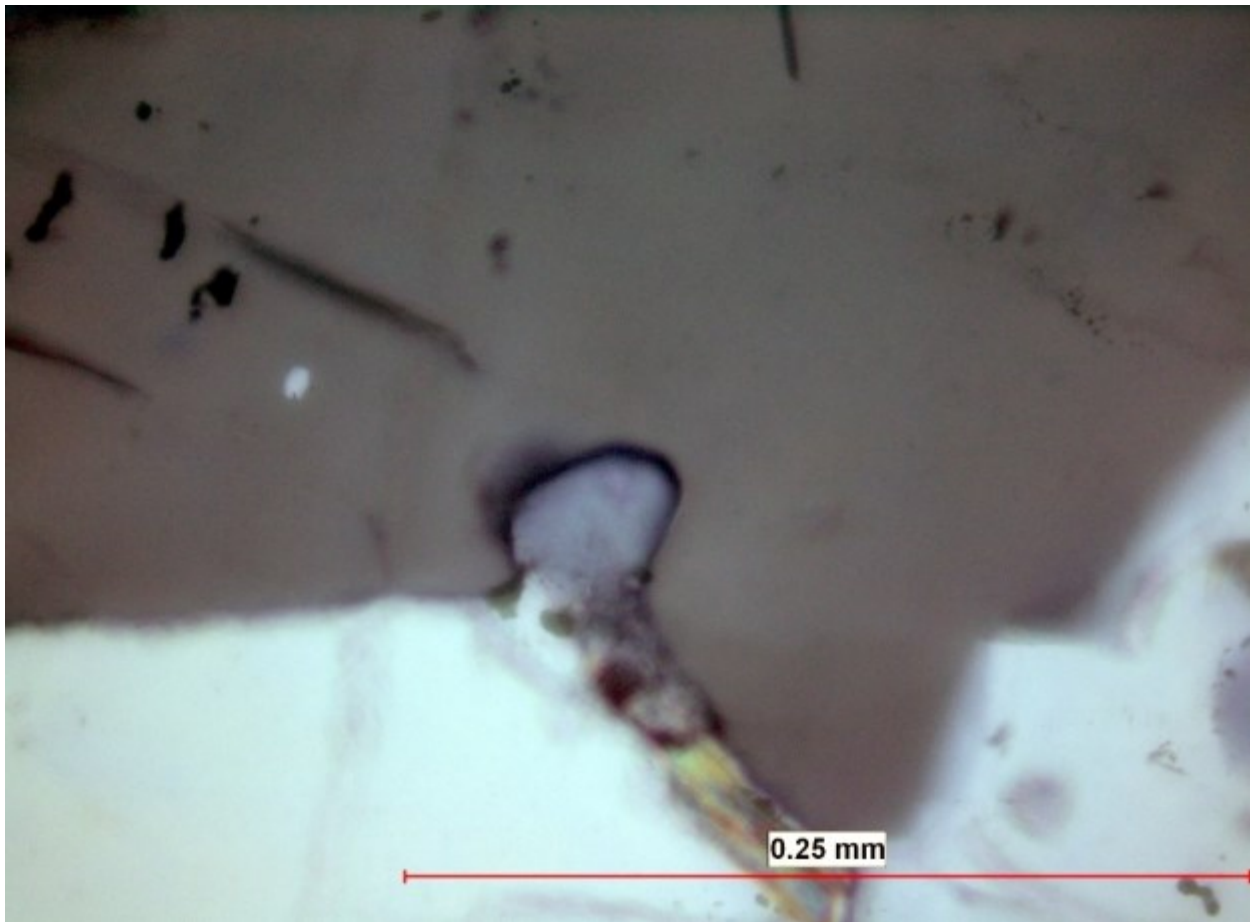


Figure 3.27: Photomicrograph of preserved grain boundary bulging. XPL. Sample RM-40. View -30→036; rotated 99° clockwise.

Also present are several microstructural features including ϕ -, σ -, and δ -type tailed porphyroclasts, mica and quartz fish, and microboudinage. Both the schist and metatonalite contain tailed porphyroclasts consisting of the matrix minerals in which the tails have been highly recrystallized and are outlined and best seen by biotite grains.

Schist samples dominantly have garnet as porphyroclasts with inclusions that do not align with the current external foliation (Fig. 3.28), i.e., $S_i \neq S_e$. Metatonalites, conversely, have larger plagioclase porphyroclasts. These also have highly recrystallized tails that are delineated by biotite grains. It is often difficult to distinguish between delta- and sigma- type tailed clasts; however, a distinction can usually be made between those and ϕ - type clasts (Fig. 3.29).

Mineral fish are present in both schist and metatonalites, generally formed by biotite and muscovite (Fig. 3.30). Mica fish are predominately group 4 type mica fish, displaying antithetic slip along the (001) axis (Passchier and Trouw, 2005, p. 142). Rarely, quartz aggregates take on the shape of mineral fish, and may represent the recrystallized relicts of former deformed grains (Fig. 3.31). Biotite grains in both the schist and metatonalites are also seen as pull-apart structures (Fig. 3.32). The recrystallized nature of the quartz grains ensures that there are few remaining grains which preserve indicators of deformation; however, structures which appear to be pull-apart clasts can be found (Fig. 3.33).

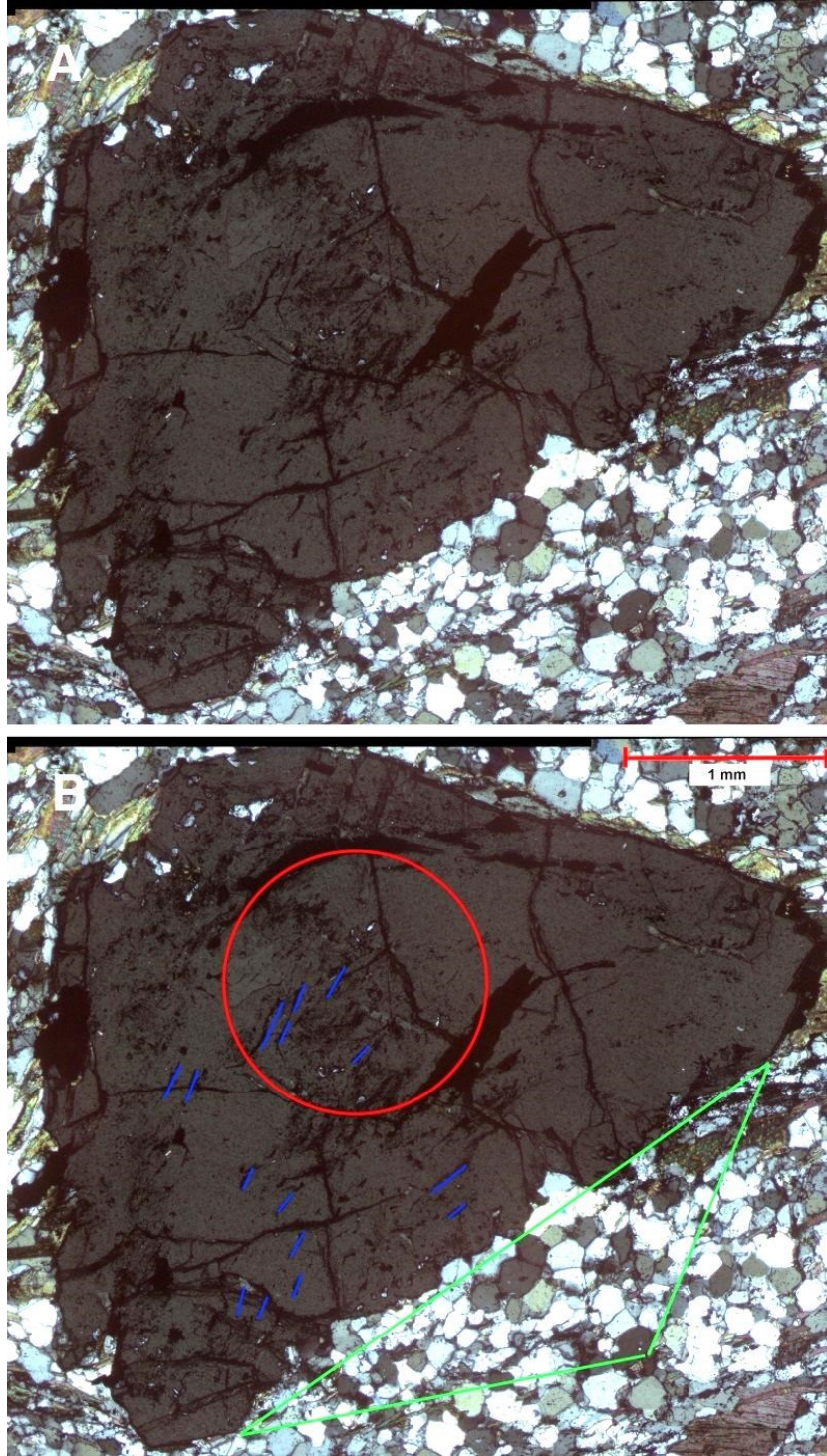


Figure 3.28: A) Photomicrograph showing garnet porphyroclasts in pelitic schist. B) The red circle indicates the possible approximate size and shape of the original garnet as defined by inclusions. Blue lines indicate the orientation of the inclusions within the garnet which define an earlier fabric. The green triangle indicates a potentially missing part of the garnet which may have broken off after the growth event that defines the internal foliation. XPL. Sample RM-36. View $-30 \rightarrow 024$; rotated 113° clockwise.

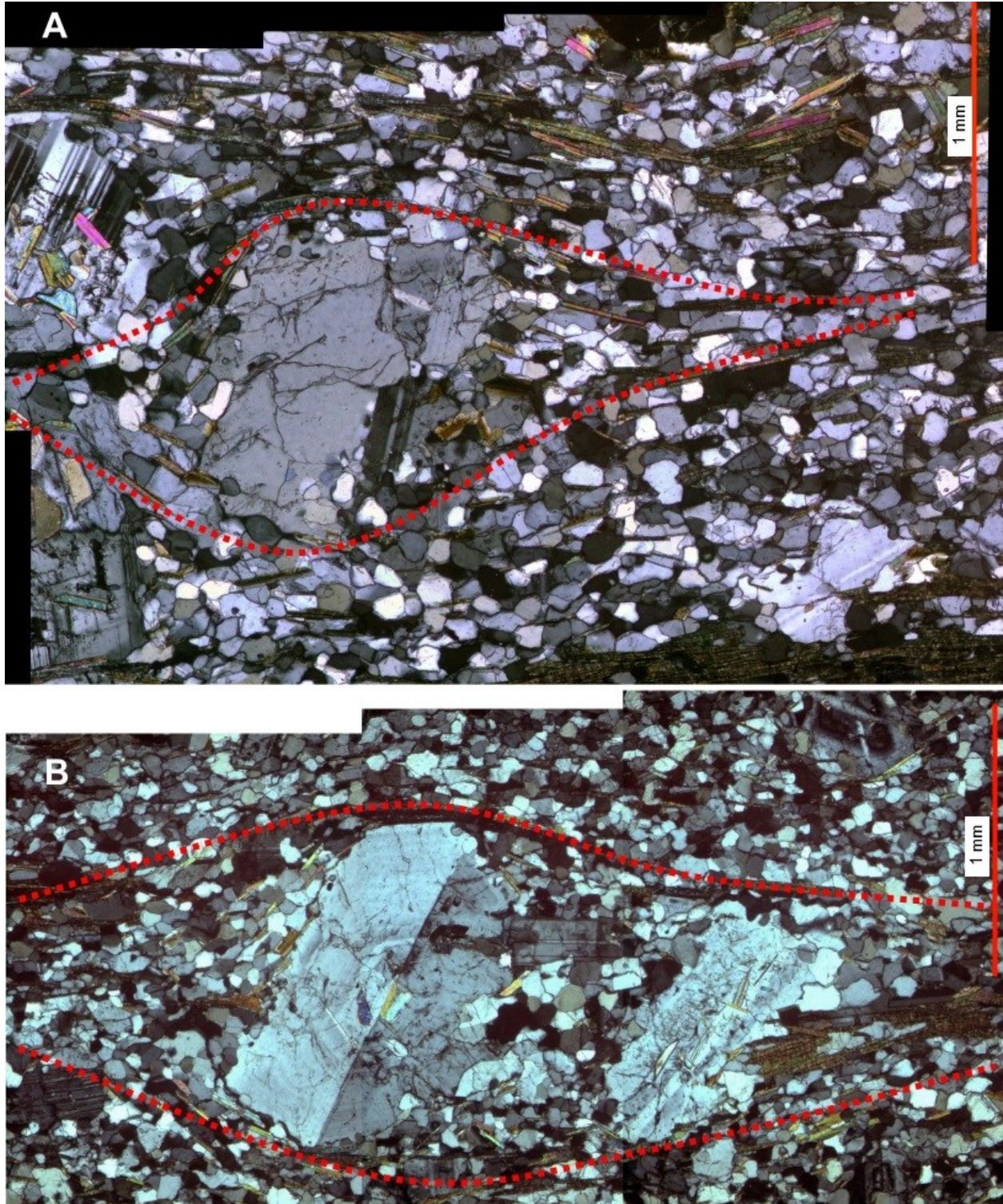


Figure 3.29: A) Photomicrograph of a plagioclase σ -clast with recrystallized tails. Relict tails are defined by biotite orientation highlighted with dotted red line. B) Photomicrograph of ϕ -clast. XPL. Sample RM-04. View 00 \rightarrow 130; rotated 5 $^\circ$ clockwise.

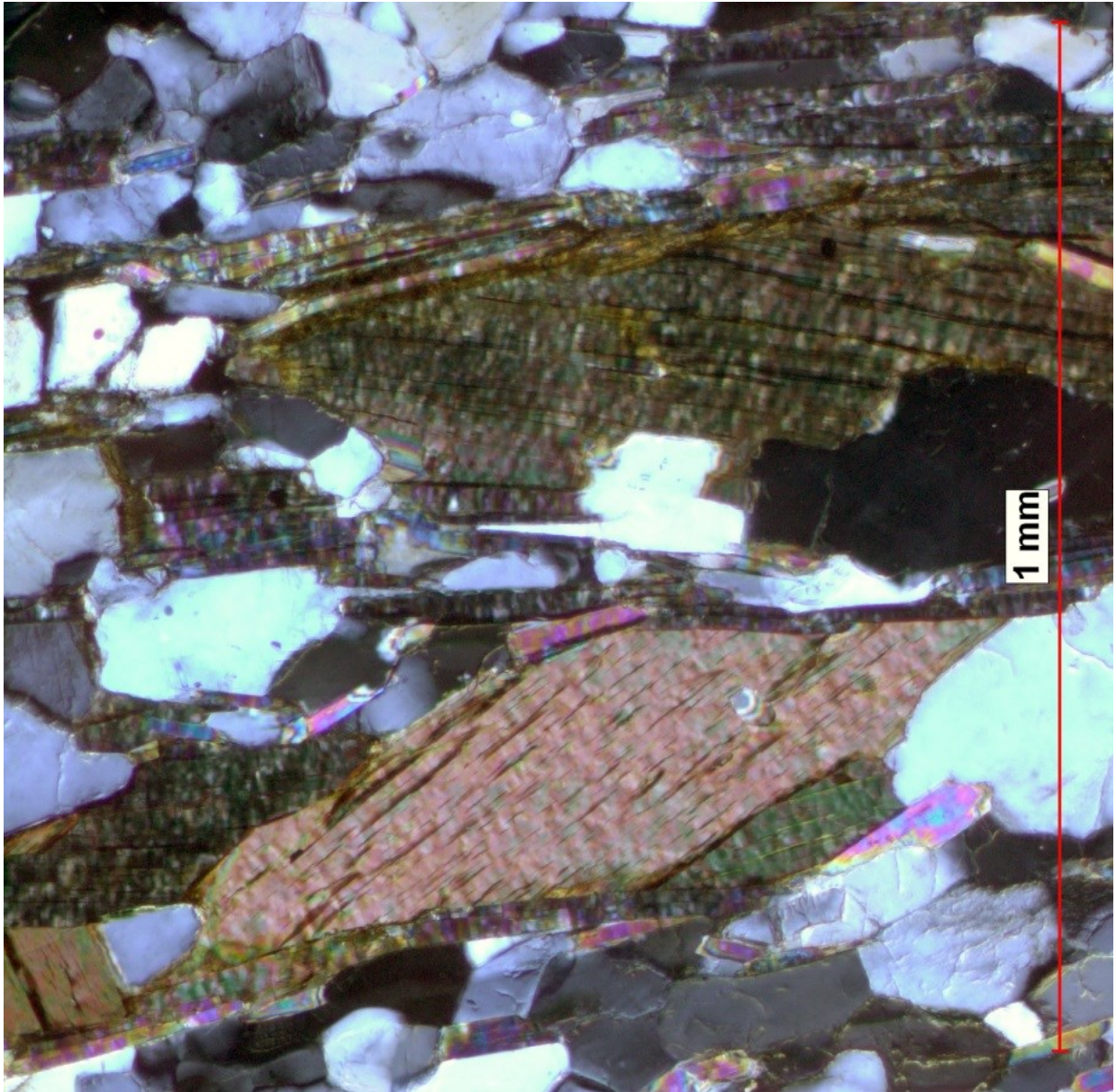


Figure 3.30: Photomicrograph of biotite-fish grain in metatonalite. XPL. Sample RM-41. View 00→290; rotated 10° counterclockwise.

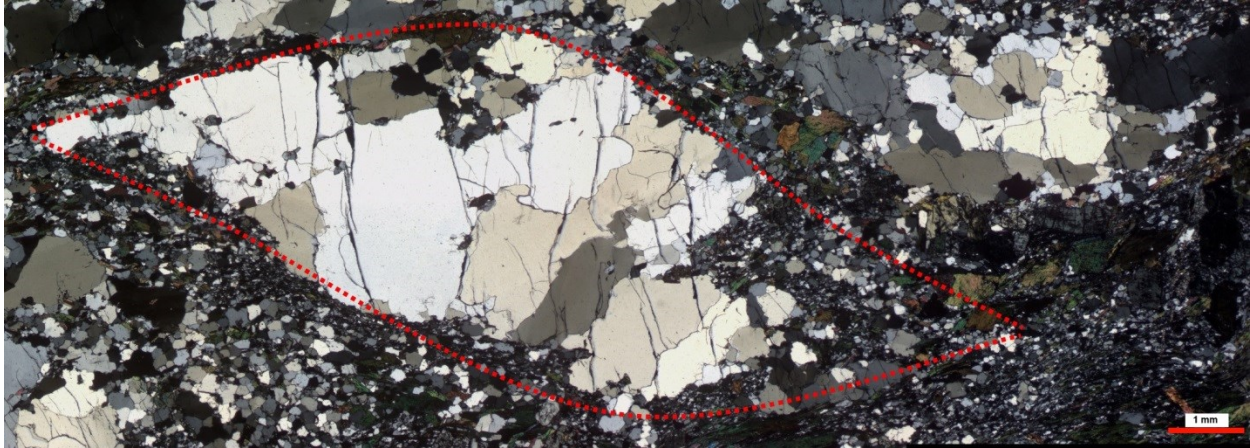


Figure 3.31: Photomicrograph of sigmoidal partly recrystallized quartz aggregate. XPL. Sample RC-02. View 00→139; rotated 61° counterclockwise.

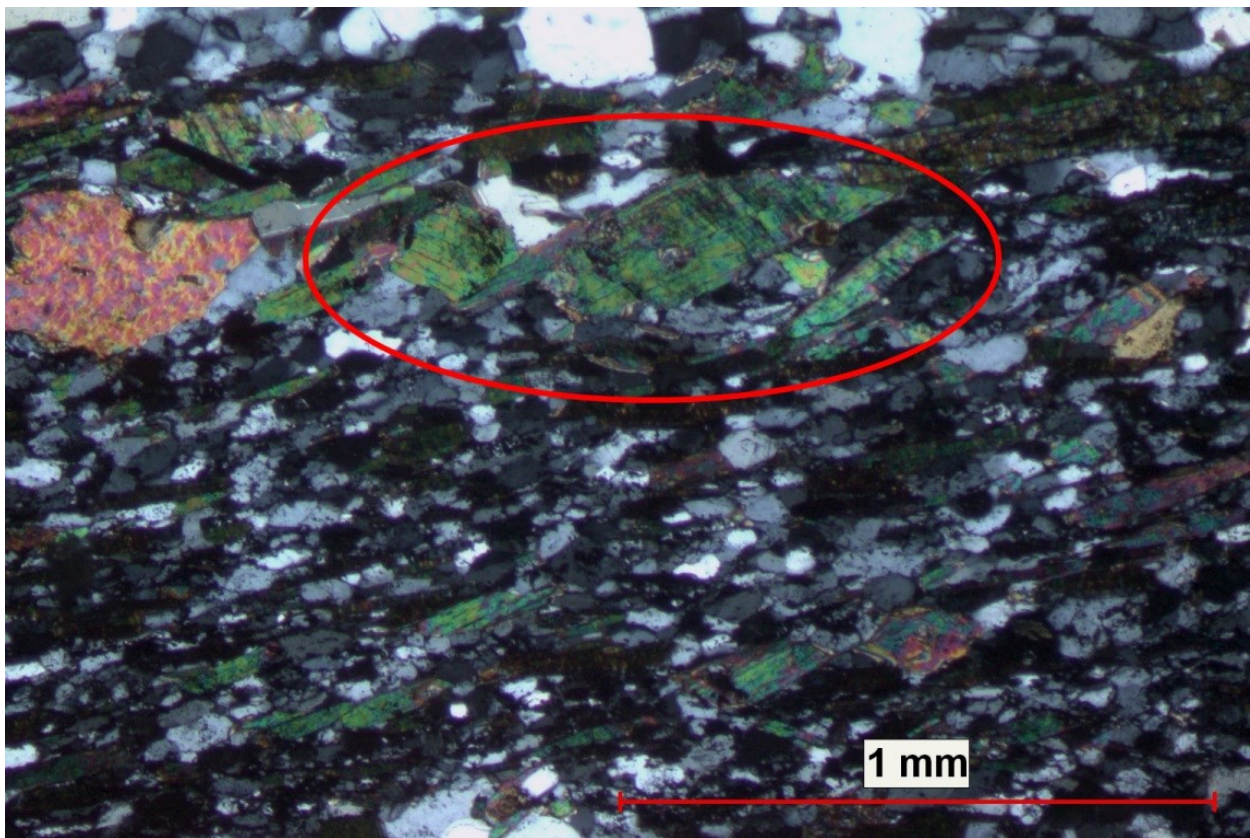


Figure 3.32: The biotites circled in red indicate an extensional pull-apart structure. XPL. Sample RC-02. View 00→139; rotated 61° counterclockwise.

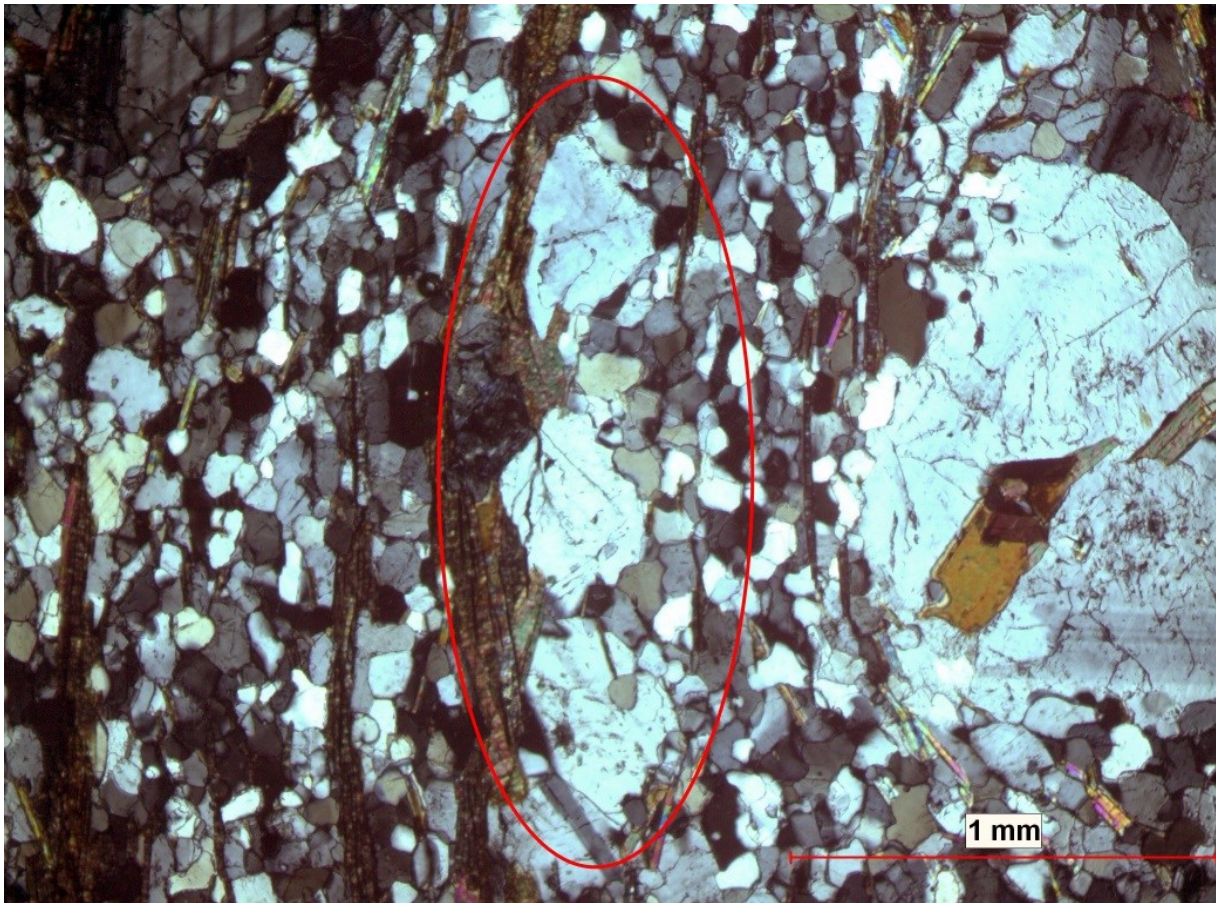


Figure 3.33: The three grains circled in red are spread out along the plane of foliation, and may have once been a single plagioclase grain which has been pulled apart. XPL. Sample RM-04. View 00→130; rotated 5° clockwise.

The above features, with exception to ϕ -type porphyroclasts, can be used to determine sense of shear (SOS). Because each thin section was taken from different locations transecting the RLCZ, SOS analysis was done one thin section at a time. A degree of confidence was given to each thin section based on how well developed the SOS indicators were, in addition to the agreement between all SOS indicators present in a thin section. For samples containing very few SOS indicators, or slides which showed often conflicting SOS indicators, a confidence level of 'Low' was assigned. Slides that contained some conflicting SOS indicators were assigned a confidence level of 'Medium'. Finally, slides that had very little or no ambiguity to their SOS were assigned a confidence level of 'High'. Figure 3.34 shows the results of this analysis, indicating that there is a strong tendency toward a NE-side-up SOS.

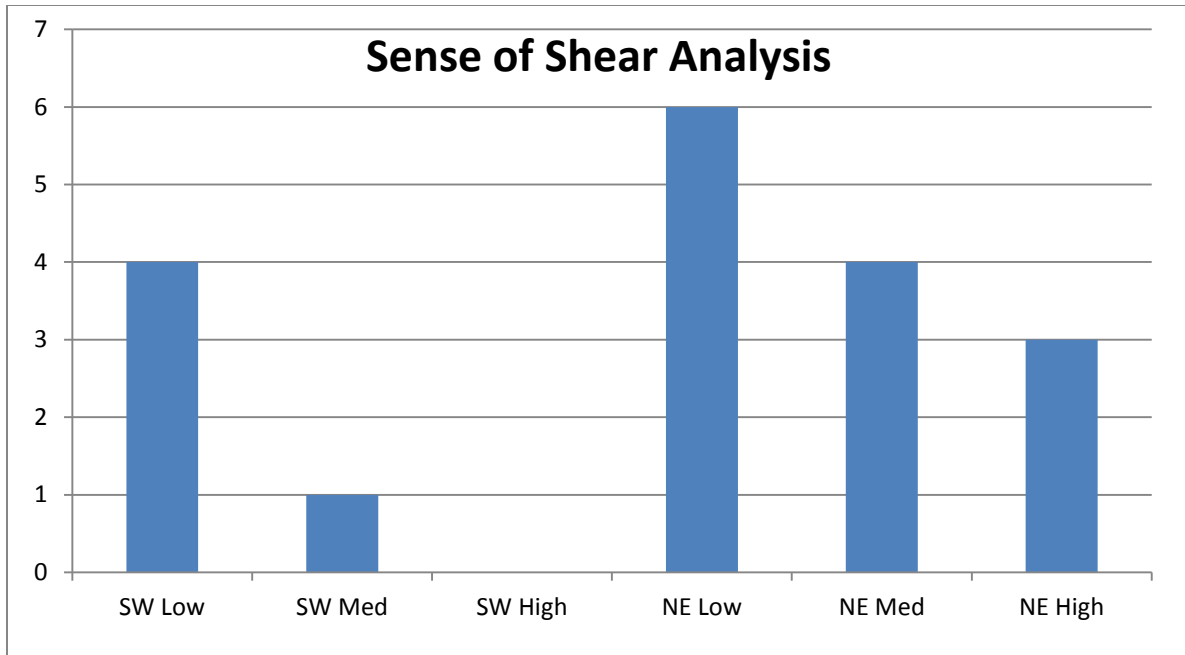


Figure 3.34: Histogram showing the results of sense of shear analysis on 18 thin sections. Direction indicates the up-thrown side and low, med, or high refers to confidence.

3.2.2.2. Vorticity

Vorticity measurements were conducted on schist and metatonalite using the modified PAR method (Passchier, 1987; Wallis et al., 1993) (Figs. 3.35-3.37). Vorticity in the metatonalite samples give a critical aspect ratio (R_c) of 1.93 (Fig. 3.35). This corresponds to a critical shape factor (B_c) of $0.58^{+0.04}_{-0.05}$ which is equal to the mean vorticity number ($B_c = W_m$) (Xypolias, 2010). Schist vorticity analysis shows $R_c = 1.68$ (Fig. 3.36). This corresponds to $W_m = 0.48^{+0.07}_{-0.07}$. Finally, combining the data for schist and metatonalite into a single chart results in an $R_c = 1.96$ and a $W_m = 0.59^{+0.05}_{-0.12}$; thus within error, all three obtained W_m values overlap each other, ranging from 0.41 - 0.64.

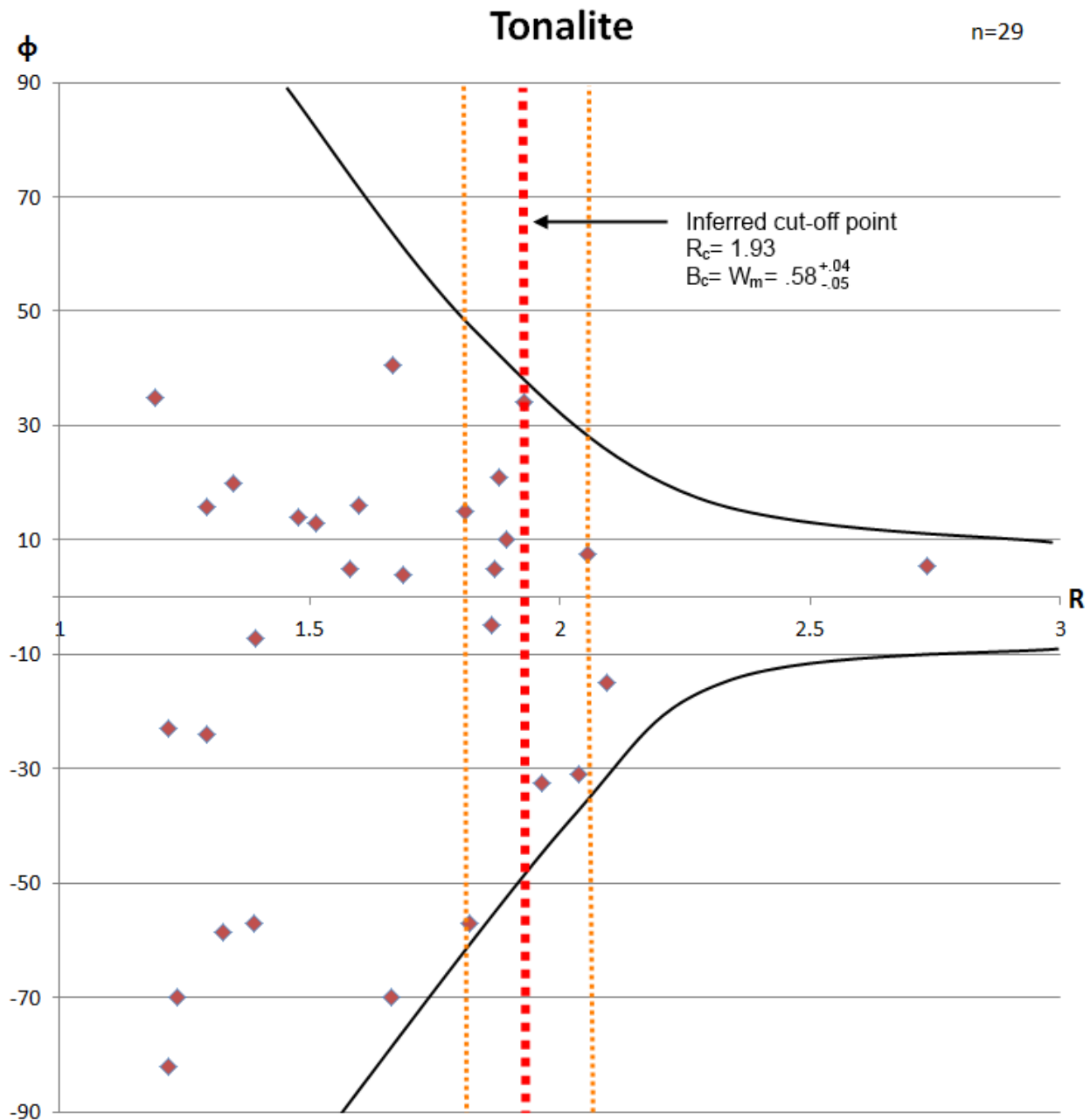


Figure 3.35: Scatter plot showing the distribution of porphyroclasts in the metatonalite. ϕ represents the angle between the long axis of the porphyroclast and the local foliation. R is the aspect ratio of the porphyroclast. Black lines are hand drawn trend lines, demonstrating the populations approach toward $\phi = 0$. The red dotted line represents the inferred cut-off point between ‘infinitely rotating’ clasts versus those that rotated toward a stable sink orientation. The orange dotted lines represent the estimated error.

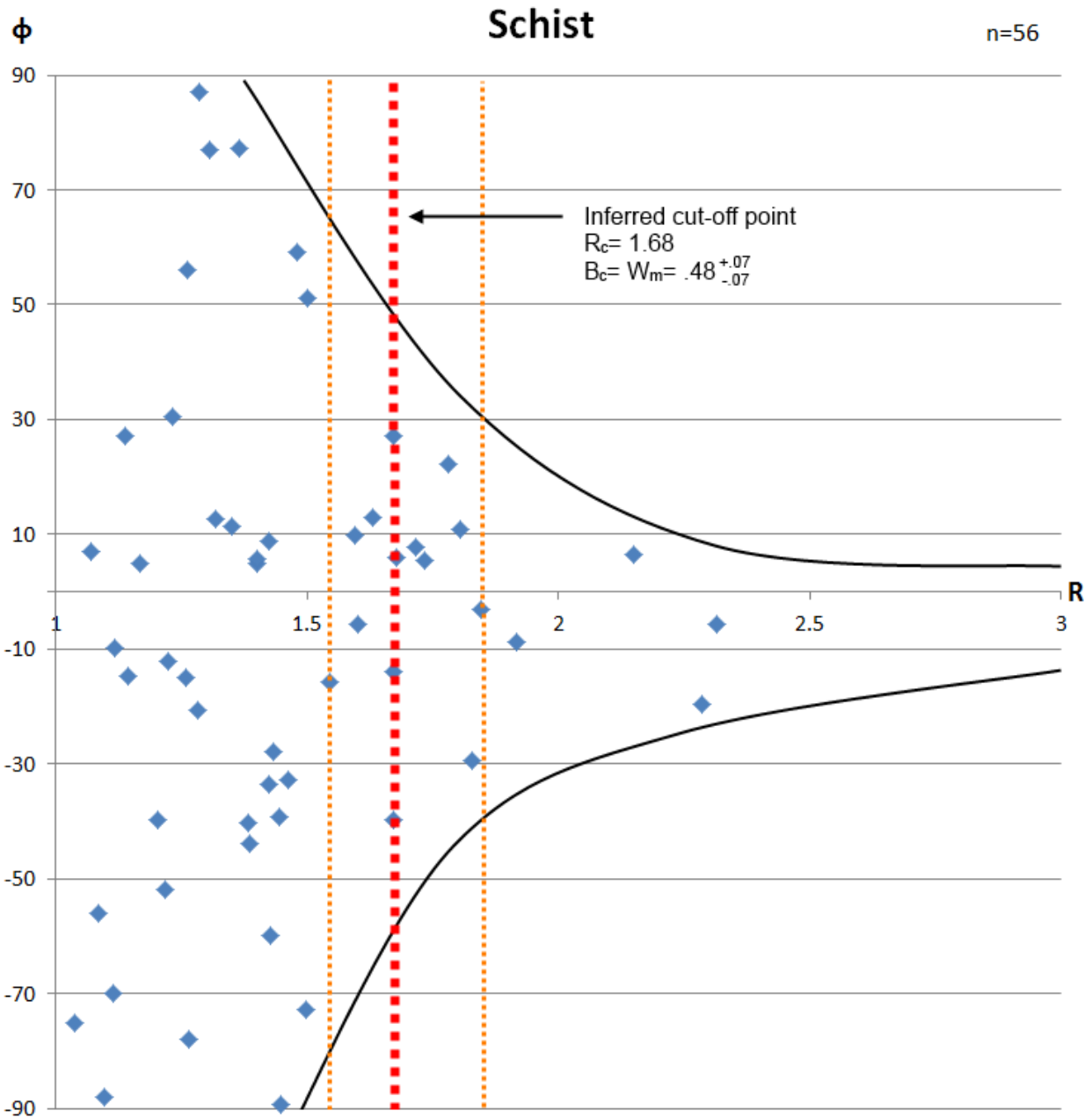


Figure 3.36: Scatter plot showing the point distribution of porphyroclasts in the schist of the RLCZ. ϕ represents the angle between the long axis of the porphyroclast and the local foliation. R is the aspect ratio of the porphyroclast. Black lines are hand drawn trend lines, demonstrating the populations approach toward $\phi = 0$. The red dotted line represents the inferred cut-off point between ‘infinitely rotating’ clasts versus those that rotated toward a stable sink orientation. The orange dotted lines represent the estimated error.

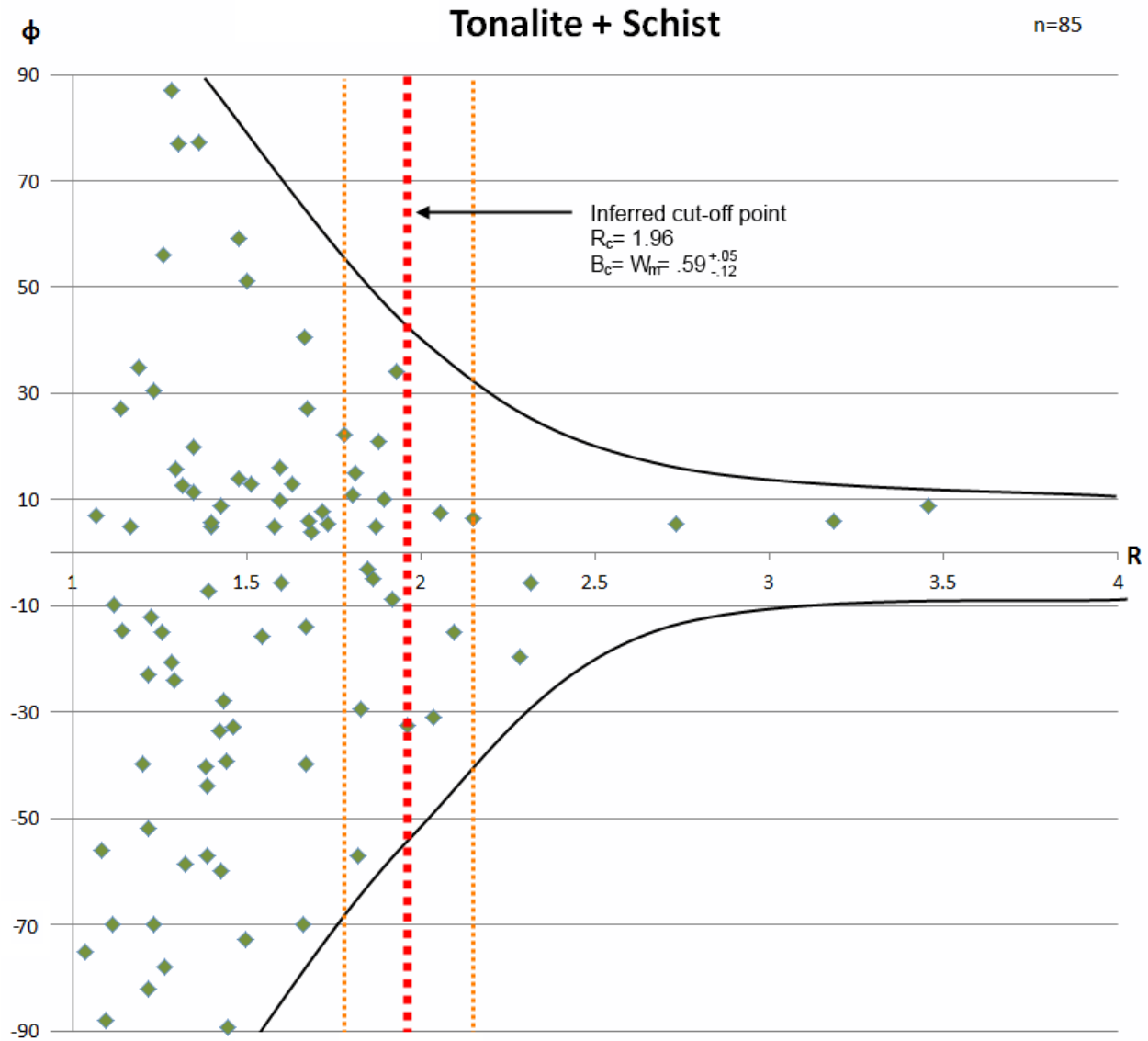


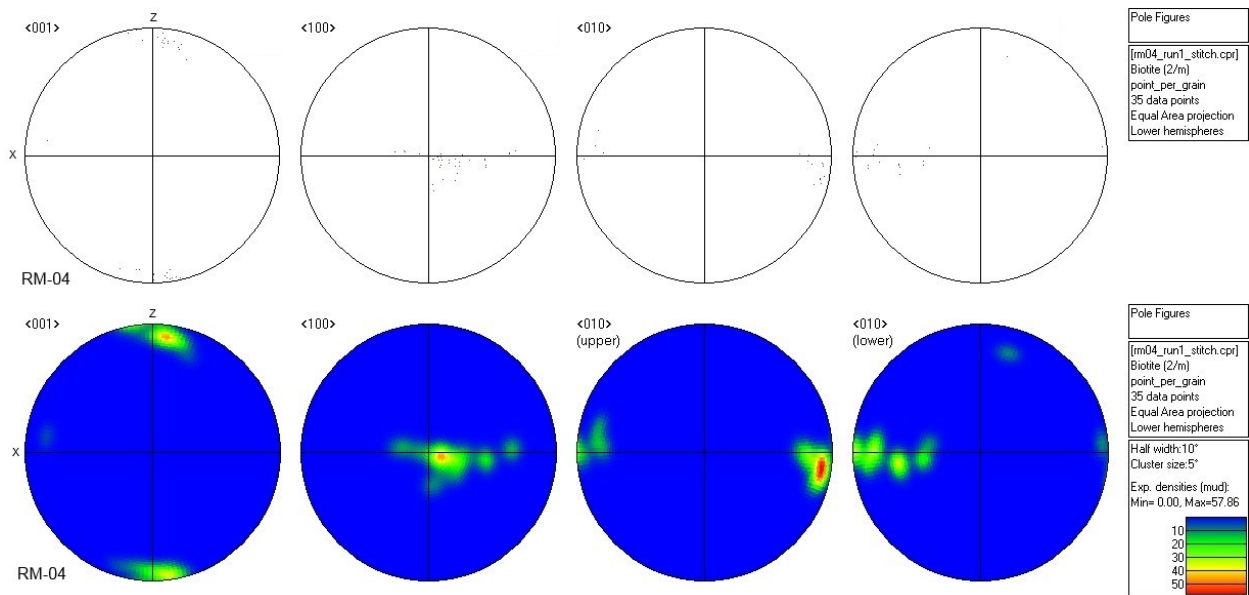
Figure 3.37: Scatter plot showing the point distribution of porphyroclasts combining the metatonalite and schist lithologies of the RLCZ. ϕ represents the angle between the long axis of the porphyroclast and the local foliation. R is the aspect ratio of the porphyroclast. Black lines are hand drawn trend lines, demonstrating the populations approach toward $\phi = 0$. The red dotted line represents the inferred cut-off point between ‘infinitely rotating’ clasts versus those that rotated toward a stable sink orientation. The orange dotted lines represent the estimated error.

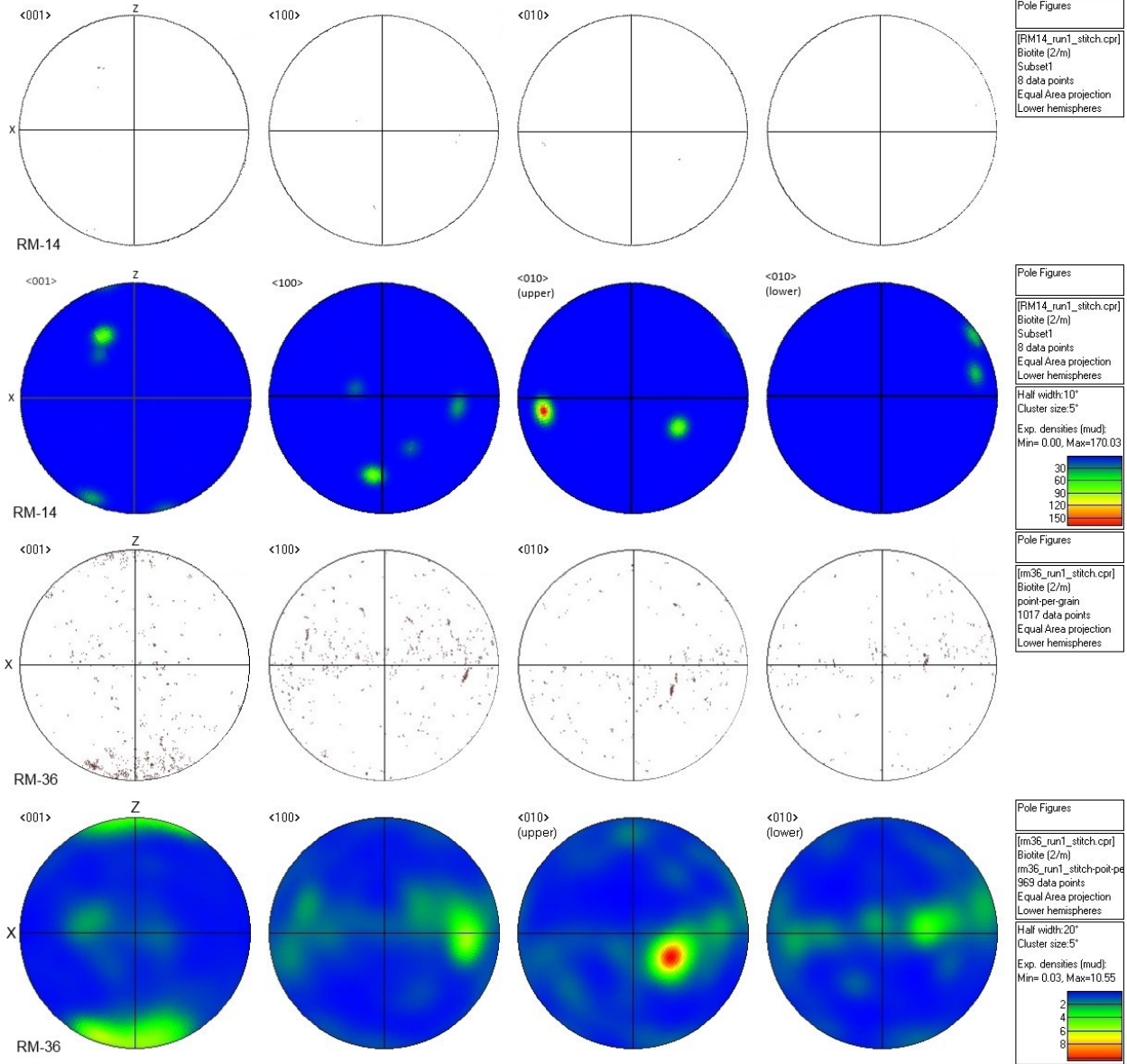
3.2.3. Electron Back Scatter Diffraction (EBSD)

EBSD was performed on five polished thin sections, and crystallographic orientations were obtained for quartz, plagioclase (as albite), biotite, garnet (as almandine), and hornblende (as

hastingsite). Of these indexed phases, quartz, biotite, and hornblende showed signs of lattice preferred orientation (LPO). For plagioclase, garnet, and hornblende, the software was set to detect the phases albite, almandine, and hastingsite (respectively) as these phases tend to have a high index percentage for their respective mineral groups.

Biotite LPO (Fig 3.38) shows some maxima at the poles of the Z tectonic direction for the $\langle 001 \rangle$ crystallographic axis, which indicates that biotite flakes dominantly are aligned parallel to the foliation. The $\langle 100 \rangle$ axis ranges from being concentrated at the intersection of the X and Z tectonic direction (equivalent to the Y tectonic direction) to forming a slight girdle along the X direction. Similarly, the $\langle 010 \rangle$ axis ranges from a girdle along the X direction to being concentrated at the intersection or the poles.





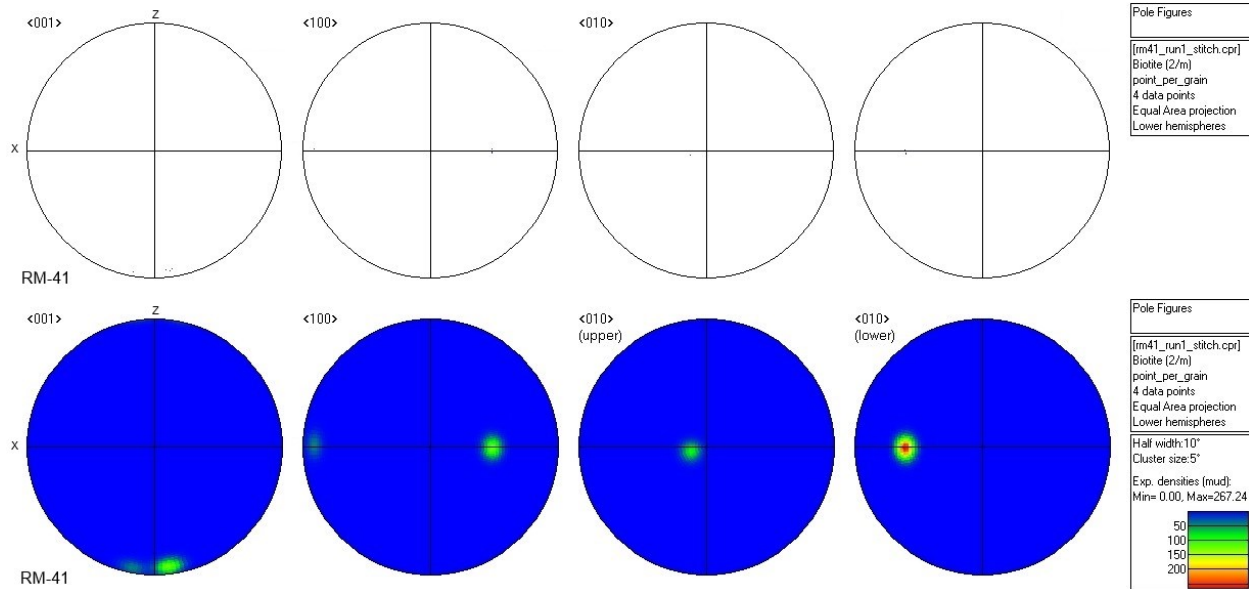


Figure 3.38: Stereonets of pole figures and contouring showing biotite LPO for samples RM-04, RM-14, RM-36, and RM-41 (respectively). All plots are equal area lower hemisphere projections of the $\langle 001 \rangle$, $\langle 100 \rangle$ and $\langle 010 \rangle$ directions. The axes labeled 'Z' and 'X' are the tectonic Z and X directions. Colors represent the multiples of uniform density (MUD) value. The half width value controls how much the pole is spread out over the surface of the project sphere, and the cluster size value speeds up calculations by finding clusters of the same orientation and replacing them with a single orientation with increased weighting. These values were left at default (as recommended by the software manual) values of 10° and 5° respectively.

Hornblende pole figures were obtained from sample N251-4, an amphibolite from near the peak of Rock Mountain (pers. comm. J. Magloughlin, 2013). Figure 3.39 shows that the $\langle 001 \rangle$ axis has maxima at the poles of the X direction, with a slight clockwise rotational asymmetry. Similarly, the $\langle 100 \rangle$ axis shows maxima near the poles of the Z direction, also with a clockwise rotational asymmetry. The $\langle 010 \rangle$ axis has a more random distribution, though there is a weak concentration at the intersection of the X and Z directions.

The $\langle 001 \rangle$ and $\langle 100 \rangle$ axes define the plane along which hornblende experiences intracrystalline glide at high temperatures (Yuanchao, 1999). It has been determined that the asymmetry of these axes from the X and Z directions, as well as their varying concentrations in opposing directions, is the result of simple shear (Yuanchao, 1999). The denser maximum direction of hornblende $\langle 001 \rangle$ axis is perpendicular to the quartz c-axis single girdles, which is at a right angle to the shear plane. Additionally,

the denser maximum direction in hornblende $\langle 100 \rangle$ axis is parallel to the direction of quartz c-axis single girdle (Yuanchao, 1999), giving a dextral, or SW-side-up sense of shear for sample N251-4.

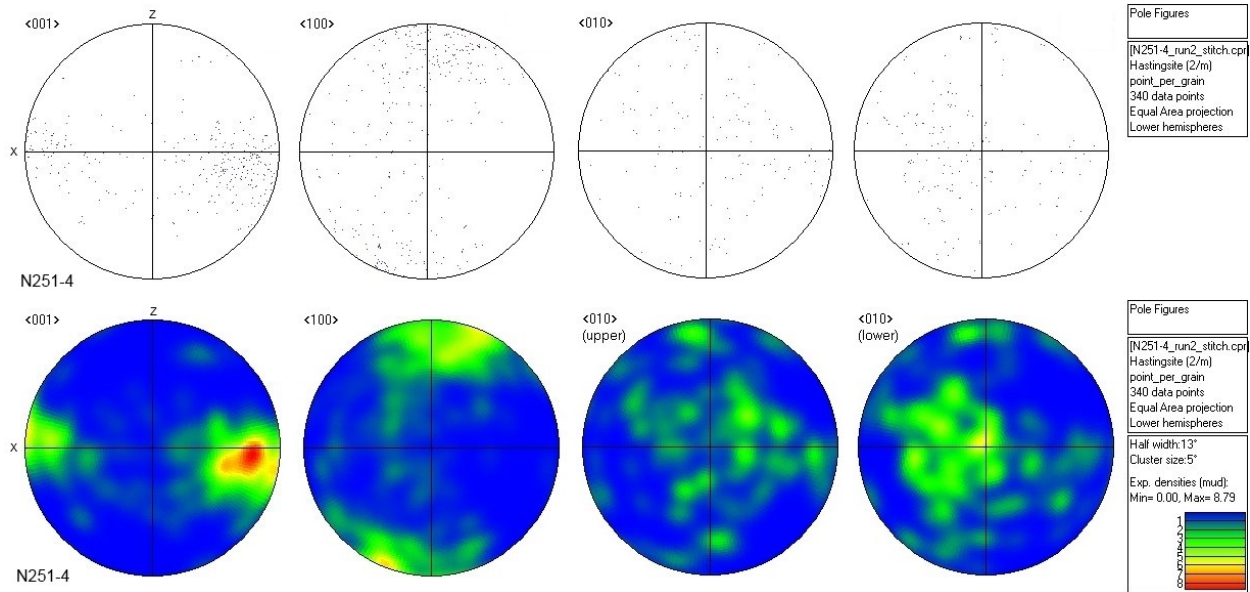
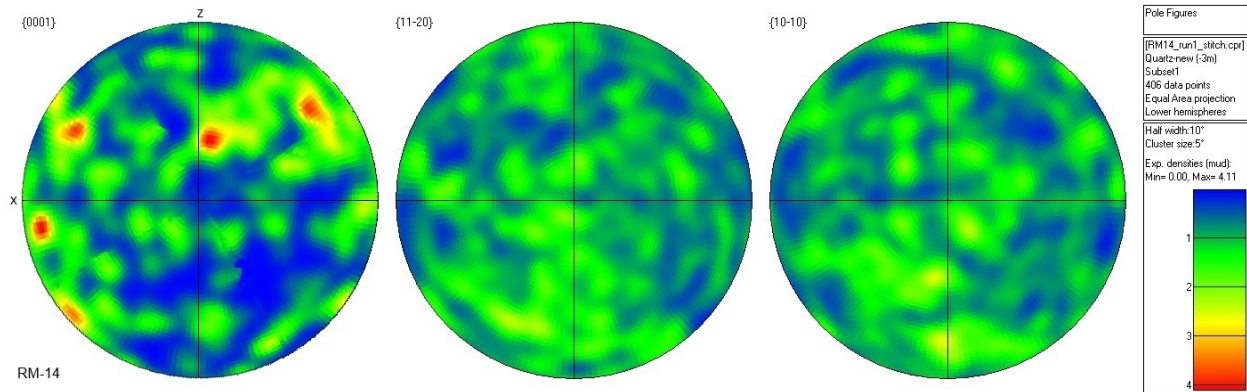
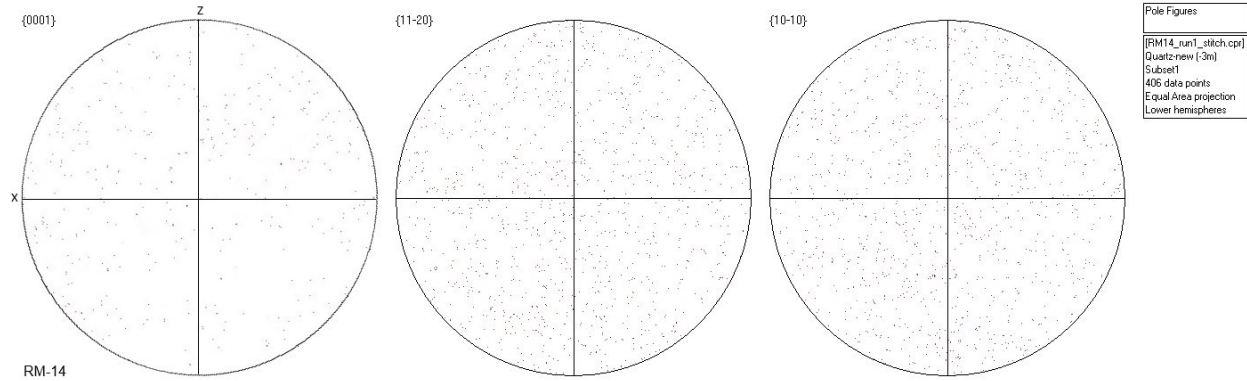
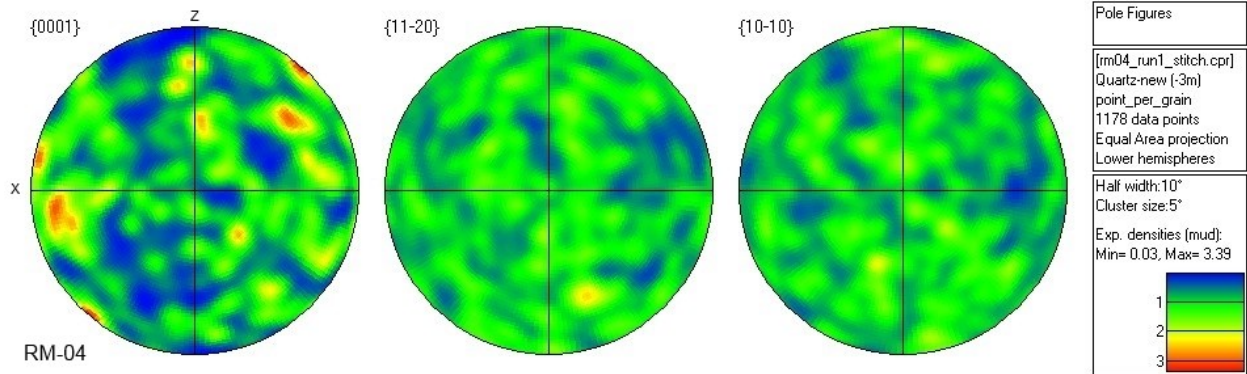
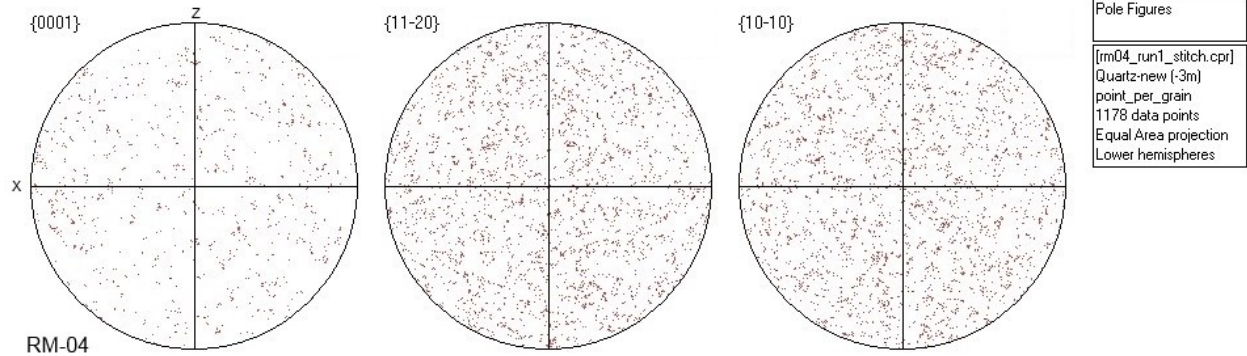
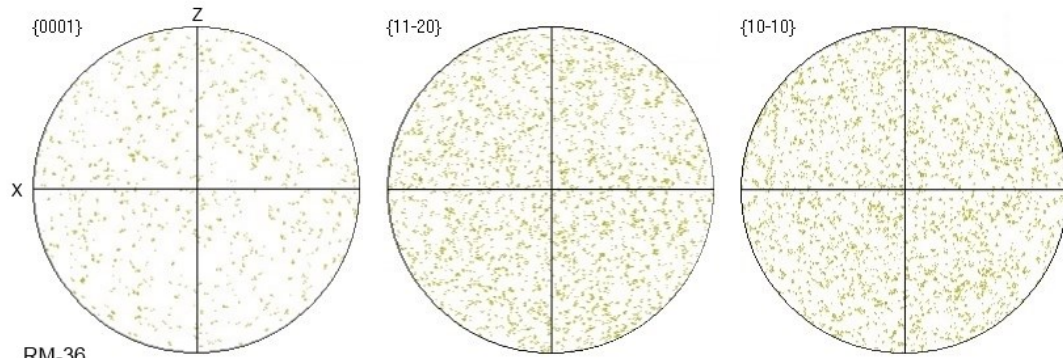


Figure 3.39: Stereonets of pole figures and contouring showing hornblende LPO for N251-4. All plots are equal area lower hemisphere projections of the $\langle 001 \rangle$, $\langle 100 \rangle$ and $\langle 010 \rangle$ directions. The axes labeled 'Z' and 'X' are the tectonic Z and X directions.

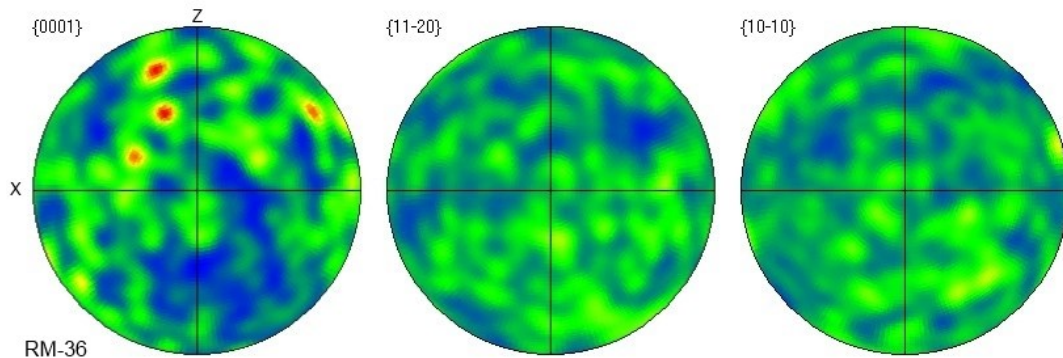
Pole figures and contoured figures for quartz are shown in Fig. 3.40. Although the a-axes of the quartz show a random distribution, the c-axes $\{0001\}$ display weak preferred orientations. Because of the high degree of recrystallization in these samples, these small clusters LPO concentrations may be the remnants of a previously stronger fabric.





Pole Figures

[rm36_run1_stitch.cpr]
 Quartz-new (-3m)
 point-per-grain
 3282 data points
 Equal Area projection
 Lower hemispheres

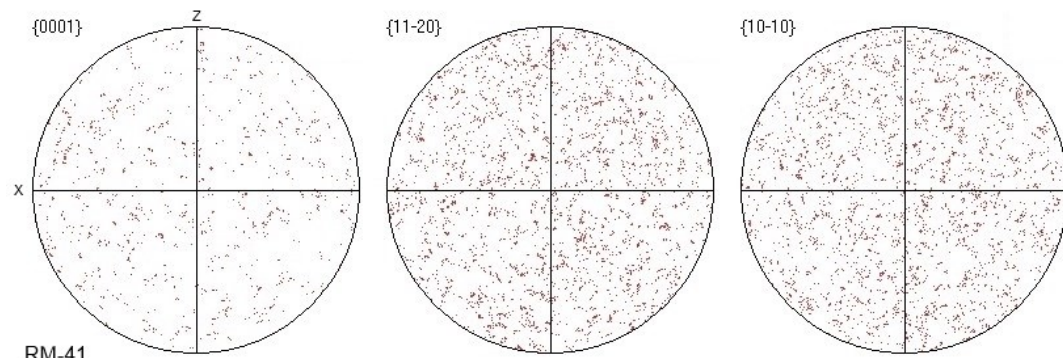


Pole Figures

[rm36_run1_stitch.cpr]
 Quartz-new (-3m)
 point-per-grain
 3282 data points
 Equal Area projection
 Lower hemispheres

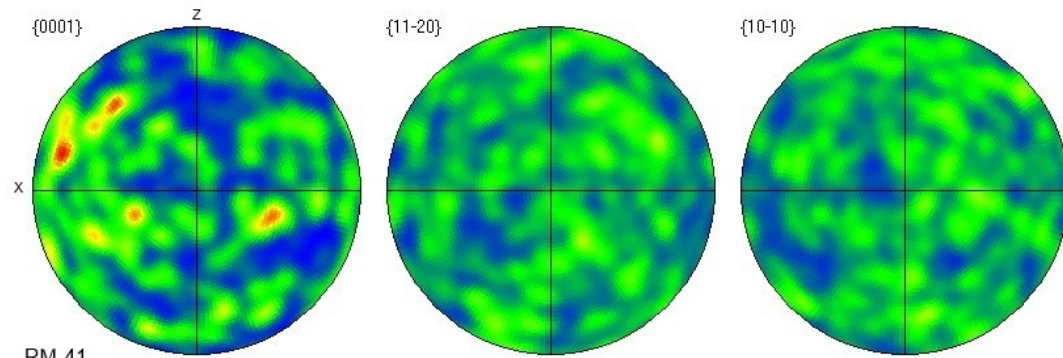
Half width: 10°
 Cluster size: 5°

Exp. densities (mud):
 Min= 0.08, Max= 3.87



Pole Figures

[rm41_run1_stitch.cpr]
 Quartz-new (-3m)
 point_per_grain
 1180 data points
 Equal Area projection
 Lower hemispheres



Pole Figures

[rm41_run1_stitch.cpr]
 Quartz-new (-3m)
 point_per_grain
 1180 data points
 Equal Area projection
 Lower hemispheres

Half width: 10°
 Cluster size: 5°

Exp. densities (mud):
 Min= 0.09, Max= 3.83

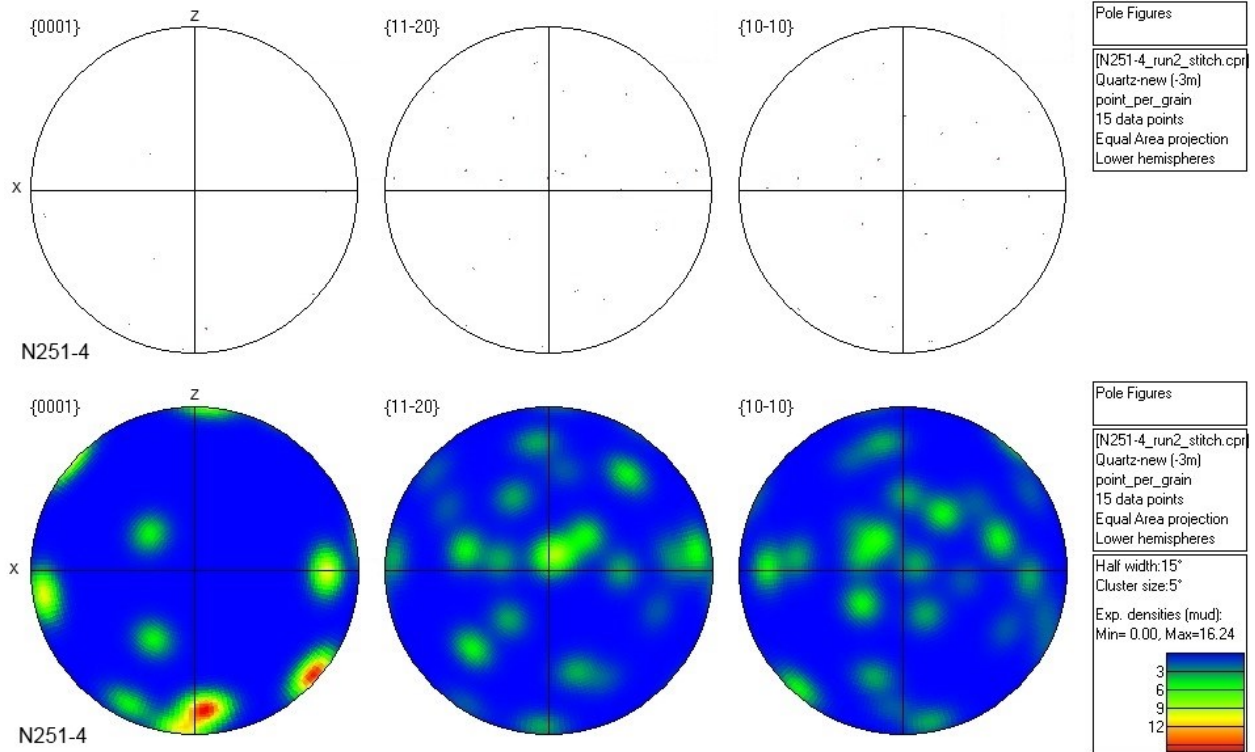


Figure 3.40: Stereonets of pole figures and contouring showing quartz LPO for RM-04, RM-14, RM-36, RM-41, and N251-4 respectively. All plots are equal area lower hemisphere projections of the {0001}, {11-20} and {10-10} directions. The axes labeled 'Z' and 'X' are the tectonic Z and X directions.

4. Interpretation and discussion

Here will be discussed the various aspects and results of the study, their interrelations, and interpretations of their meaning and relevance. Analysis of field, AMS, microstructural, and EBSD data shows a highly consistent structural fabric within the cryptic zone which clearly deviates from that of the surrounding area. Field and structural data demonstrate the unique fabric of this zone in comparison to much of the Nason Terrane. AMS data independently confirm the current structural fabric and shows no indication that foliation has been reoriented due to its consistency throughout and adjacent to the zone. Microstructural data are useful in determining SOS as well as vorticity, and therefore, helps in the understanding of strain history. And, finally, EBSD shows that a crystallographic preferred orientation has been preserved, and is useful in determining SOS.

4.1. Field and structural data

The foliation of the RLCZ is extremely consistently dipping steeply to the NE with very little change over the 1 km width of the zone (Figs. 3.2 & 3.3, Magloughlin, 1993; Miller et al., 2006). The variability in foliation orientation that would be expected from a type II superposed folding event was not observed on Nason Ridge. Rather, the highly consistent foliation orientation is more typical of that which would be created in a zone dominated by simple shear (Bell, 1981) in which the regional foliation rotates into alignment with that of the mylonitic foliation (Passchier and Trouw, 2005), or in which the regional foliation is reactivated forming a new but essentially identically oriented foliation. Additionally, the proposed older NE-SW trending superposed fold by Miller et al., 2006, should be expected to be a major tectonic event. However, this model fails to explain why indications of an earlier foliation are not present both within the zone and across the terrane, oriented orthogonal to the current foliation, as would be expected (Lebit et al., 2002). It should also be noted that simple shear can create complex fold patterns that look similar to multiple phases of folding in outcrop (Carreras et al., 1977).

The orientation of the fold hinge lines (Figs. 3.6 & 3.7) and mineral lineations (Figs. 3.10 & 3.11) are also indicative of simple shear deformation. Mineral elongation (stretching) lineations (MEL) cluster tightly. Miller et al., 2006, interpreted the lineation as a b-lineation, that is, lineations which follow fold hinge lines. However, if the MELs are b-lineations, a significant degree of orientation variability would be expected. However, such a tight clustering of lineations is consistent with the expected mineral lineations present in simple shear regimes (Bell, 1981). These lineations, especially the very consistent orientations, are more simply explained by formation in simple shear, perhaps in part due to rotation of elongate minerals such as amphibole (Piazolo, 2002).

Fold hinge lines cluster in approximately the same orientation as mineral lineations, although they are more dispersed, forming a girdle along the RLCZ foliation. Miller et al., 2006, interpreted this girdle to indicate the presence of older NE-SW trending hinges which have been reoriented by younger folds with NW-SE trends and sub-horizontal hinges. However, this interpretation does not explain the abundance of sub-vertical hinges and very few sub-horizontal hinges. Additionally, the uneven distribution of the girdle, as well as the tendency of fold hinge lines to plunge shallowly to the NW, is not explained by an overprinted NE-SW fold.

Instead, when viewed as the result of simple shear, the girdle of fold hinge lines is interpreted as quartz veins resisting rotation by simple shear (Bell, 1978; Carreras et al., 2005). In this case the uneven distribution of fold hinges is due to the majority of folds being rotated into near parallelism with the shear direction, whereas some are more resistant to this rotation. Additionally, the preference for fold hinges to approach horizontal to the NW is interpreted as the initial plunge direction of the folds created by the D3/D4 event.

Also left unexplained by the superposed folding model is the highly focused nature of these structural features which are only present for 1 km across strike. It is unexplained how a large scale

tectonic event could create only a single swath of folding within a zone at identical metamorphic grade to the rest of the terrane.

In addition to the reorientation of preexisting folds, large amounts of simple shear may lead to the formation of sheath folds (Carreras et al., 1977), which are generally assumed to represent large amounts of simple shear with $\gamma > 10$ (Cobbold and Quinquis, 1980). Several apparent sheath folds (e.g., Figure 3.9) are a likely product of large amounts of simple shear, and cannot be explained by a folding model.

The observed asymmetries of boudins at the macroscale also indicate an overall monoclinic symmetry created by simple shear (Fig. 3.12), and can act as SOS indicators (Goldstein, 1988). Within the Rock Lake area, the majority of asymmetric boudins fall under the category of type-III (Goldstein, 1988) or forward-vergent antithetic slip (Goscombe, 2003) boudins. However, there were an insufficient number of boudins observed and analyzed at the macro-scale to make any robust interpretations.

Within the RLCZ, metatonalite layers, mostly concordant (sill-like), show strong foliation and MELs. In one case, a thick sill contains quartz veins resembling large tension gashes (Magloughlin, 1993; Magloughlin, personal communication, 2013). This is shown in Fig. 4.1, and indicates simple shear dominated deformation (Fossen and Tikoff, 1993).

4.2. AMS

AMS lineation and foliation data, especially when defined by platy minerals such as biotite, independently support foliation and lineation data observed in the field (Aubourg et al., 2000; Pares and van der Pluijm, 2002). AMS foliation and lineation stereonet (Figs. 3.13-3.18) demonstrate a strong correlation with the structural stereonet (Figs. 3.6 & 3.10).

When biotite controls the magnetic fabric, the line normal to the K_{\min} has been shown to represent the c-axis of the biotite (Zapletal, 1990; Ono et al., 2010) which in this case is oriented normal

to the macroscopic foliation. Studies correlating the AMS with structural S–C fabrics have shown that the plane normal to K_{\min} approximates the S foliation, whereas K_{\max} coincides well with the orientation of the long axes of the biotite (Ono et al., 2010), interpreted to represent the maximum stretching axis within the C plane (Pares and van der Pluijm, 2002). A study of metapelites shows that deformation has a stronger influence on the shape of the magnetic susceptibility ellipsoid than composition or metamorphic grade (Richter et al., 1993). The same study concludes that the shape of the magnetic ellipsoid is coaxial with, and therefore an accurate indicator of the principal direction of shortening and extension, regardless of metamorphic grade (Richter et al., 1993). For the case of the RLCZ, this indicates that the stretching direction is parallel to lineations (that is, steeply plunging north to northeast) and the shortening is normal to the foliation.

Studies examining the AMS fabric of superposed folds of quartzite (Mamtani and Sengupta, 2010) and of metabasic rocks (Ghosh et al., 2010) both indicate distinctly separate orientations of the magnetic lineation and foliation, representing separate deformational events. Even in instances where host rocks have been completely annealed, previous AMS fabrics carried by biotite have not been reset by the static thermal overprint, and thus record the most recent deformation event (Ferré, 2000). Because AMS data from the Rock Lake area shows only a single strong orientation which corresponds to the macroscopic foliation and lineation, it is interpreted that there have been no more recent events which were capable of reorienting the magnetic fabric, such as a folding event. Therefore the most recent deformational event must have been able to reorient the lineation yet preserved the regional foliation.

4.3. Microstructures and petrology

Microtectonic indicators of simple shear and SOS include mineral fish, quarter structures, pull-apart clasts, domino clasts, and tailed porphyroclasts. The most prevalent and best preserved, and

therefore most useful, of these are the garnet and plagioclase porphyroclasts within the schist and metatonalites, respectively. The presence of multiple types of SOS indicators, especially the abundance of tailed porphyroclasts which commonly give clear SOS indications (Figs. 3.29 & 3.34), is interpreted as clear evidence for simple shear. Sense-of-shear analysis (Fig. 3.34) shows strong agreement among various samples from different localities within the RLCZ, giving a clear NE-side-up displacement direction. Because the displacement direction closely matches the foliation, this is interpreted as indicating a high angle reverse shear zone in its current orientation. However, the issue of tilting of the terrane remains under discussion (e.g. conjecture surrounding the Baja B.C. hypothesis). If the area has been tilted more than about 10° down to the SW, it becomes a normal-sense shear zone, though still with north-side-up displacement.

Vorticity analysis adds insight into relative degrees of simple shear and pure shear. Natural shear zones rarely, if ever, undergo exclusively simple shear, and nearly always have some component of pure shear as well (Tikoff and Fossen, 1993). Vorticity analysis performed on rocks from the RLCZ (Figs. 3.35-3.37) gives mean vorticity numbers (W_m) from 0.41 - 0.64. The mean vorticity number ranges from 0 to 1 with 0 representing end member pure shear, 1 representing end member simple shear, and a value of 0.71 representing the middle point between simple and pure shear (Xypolias, 2010). Therefore, rocks within the RLCZ have experienced, on average, general shear strain. This interpretation from vorticity also correlates well with the interpretation from AMS that clearly shows an oblate magnetic susceptibility ellipsoid, indicating strain which falls between the extremes of plane strain and flattening, consistent with general shear. Transpressional shear zones are known to display stretching lineations due to extrusion of material perpendicular to the displacement direction, but kinematic indicators in these cases still indicate the proper displacement direction perpendicular to the lineation (Tikoff and Greene, 1997). The agreement between lineations and kinematic indicators in the Rock Lake

area indicates that the formation of lineations perpendicular to displacement by extrusion is not likely taking place.

4.4. EBSD

LV-SEM EBSD work concentrated on quartz crystallographic orientations as it was believed that quartz may preserve crystallographic orientations (Heilbronner and Tullis, 2002; Otani and Wallis, 2006). Figure 3.40, however, demonstrates that the quartz crystallographic fabric appears to be random, with the exception of a few concentrations which, when connected, could indicate a weak girdle. The weak CPO in quartz is attributed to the polymineralic nature of the samples, in which the behavior of quartz is considerably less well understood than monomineralic samples (Prasannakumar, 2010) as well as the amphibolite facies conditions which promote recrystallization. Similar cases of poor quartz fabrics have been reported, both from the Chiwaukum Schist and elsewhere, and have remained enigmatic (Leiss et al., 2002).

Conversely, both biotite and hornblende displayed notable CPOs from which a sense of shear can be determined. Biotite data, unfortunately, are more difficult to obtain as proper polishing and indexing of EBSPs is problematic. CPO data acquired did indicate simple shear with the $\langle 100 \rangle$ and $\langle 010 \rangle$ directions forming a girdle along what is interpreted as the shear plane (Dempsey et al., 2011), and the c-axes maxima parallel to the shear plane and perpendicular to offset (Law, 1990; Dempsey et al., 2011).

Hornblende CPO is produced by intracrystalline glide with the $\langle 001 \rangle$ plane aligned along the shear direction and the $\langle 100 \rangle$ parallel to the shear plane (Yuanchao, 1999). Sense of shear is then determined by the asymmetric CPO pattern. The sole amphibolite sample analyzed by EBSD shows a NE-side-down sense of shear (Fig. 3.39). This result is opposite of the vast majority of the data which indicates a NE-side-up shear sense. A possible explanation for this is that the different lithology of the amphibolite within the surrounding schist may have caused the amphibolite to over-roll and therefore

“flip” its sense of shear (Passchier, 2001; Coelho et al., 2005). Also, this single sample was from a swath of unusual mafic metaigneous rocks suspected to have been intruded during RLCZ deformation, and thus the strain within these rocks may have been fundamentally different than that within the Chiwaukum (Magloughlin, personal communication, 2013). Regardless, the strong asymmetric CPO of the hornblende indicates the presence of significant simple shear strain (Cao et al., 2010).



Figure 4.1: Tension gashes (quartz veins) consistent with northeast-side-up simple shear strain. View is approximately horizontal to the southeast (after Magloughlin, 1993).

5. Conclusions and future work

5.1. Conclusions

The following conclusions can be made from the present study:

1. Throughout the study, no significant evidence was found that supports the hypothesis of superposed folding as the primary structural cause of the features seen in the Rock Lake area. Fold hinge lineations which form a NW-SE girdle remain the only feasible indicator of lineation reorientation by fold interference, but these are equally well explained by simple shear dominated deformation.

2. Field mapping shows that macroscopic structural features such as asymmetric boudinage and folds consistently display monoclinic symmetry, and do not fit the expected geometries generally associated with superposed folding.

3. Anisotropy of magnetic susceptibility indicates that biotite, which carries the magnetic signature, is aligned with c axes perpendicular to the foliation. Electron backscatter diffraction indicates asymmetries consistent with NE-side-up shear motion. EBSD performed on quartz, however, shows random fabrics, likely due to recrystallization.

4. Microstructural analysis clearly indicates the presence of recrystallized fabric with relict microstructures indicative of shear zones. This is demonstrated by recrystallized mantled porphyroclasts as well as asymmetric features such as mineral fish, micro-boudins, pull-apart structures, and dominoed clasts. Vorticity analysis using mantled clasts indicates general shear, and microstructural analysis using SOS indicators indicates NE-side-up displacement.

5. An alternative model, that a pre-existing weakness, defined by the extant regional foliation, was reactivated as a general shear zone, better explains the available data.

6. The Rock Lake Cryptic Zone of this study was accurately denoted the Rock Lake Shear Zone by Magloughlin, 1990.

7. The presence of a large-scale shear zone cutting the Nason Terrane, presumably listric on a large scale, may lend support to the view that discordant magnetic poles are better explained by the tilting of major crustal blocks rather than northward transportation (Costanzo-Alvarez and Dunlop, 1988), i.e., that less northward transport than has been proposed was necessary.

5.2. Future work

Additional questions regarding the RLSZ still exist and deserve additional study.

- Although the RLSZ is a major structural features, its geometry is not well constrained. Additional work is needed to better constrain the amount of displacement, its breath and length, and, if possible, its geometry at depth.

- An important, and yet unresolved question, is the age of the shear zone. Cross-cutting relations indicate that shearing was the last major ductile process, and post-dates both the MSB and the metatonalite intrusion. However, relating the RLSZ to the MSB immediately to the south may shed light on the contributing factors for the existence of the shear zone. Additionally, the temporal relation between the RLSZ and the White River Shear Zone (Magloughlin, 1986, p. 105) to the NE is not well understood. A possible scenario is that the two shear zones formed simultaneously by NE-SW shortening across the region.

- More EBSD would be instructive in better understanding the nature of strain both inside and outside of the RLSZ. The data obtained from the amphibolite sample shows strong, but opposite sense of shear, patterns than the determined NE-side-up motion. However, it is possible that the sample orientation may have been reversed either by a geological processes or by human error. Both additional EBSD analyses on amphibolites from throughout the shear zone, as well as more intensive study on the geometry of the amphiboles in outcrop is needed. The question of why quartz axes would not retain their CPOs, or potentially not form a strong CPO during shearing, is attributed to annealing and lithology.

However, a more in-depth analysis is warranted. Speaking more broadly, the way that quartz behaves at different conditions and lithologies is still in need of much refining. For example, studies have been performed on the behavior of quartz at various strains, and the behavior of quartz at various P-T conditions. However, studying the behavior of quartz patterns while varying P-T conditions and strain is yet to be seen. The added complexity of different rock types makes interpretation even more difficult.

- While vorticity analysis was performed using tailed porphyroclasts, other possible vorticity indicators may shed additional light on the kinematics of the shear zone. For example, tension gashes, which are known to be present, can act as vorticity gauges.

- Additional detailed analyses focusing on fold orientations and asymmetries would also aid in better understanding the strain history of the zone.

6. References Cited

- Ague, J.J., 1990. Restoration of offset along the Straight Creek-Fraser fault system, Washington State and British Columbia. *Abstracts with Programs - Geological Society of America* 22, 229.
- Ague, J.J., Brandon, M.T., 1996. Regional tilt of the Mount Stuart batholith, Washington, determined using aluminum-in-hornblende barometry: Implications for northward translation of Baja British Columbia. *Geological Society of America Bulletin* 108, 471–488.
- Anderson, L.J., 1997. Regional tilt of the Mount Stuart batholith, Washington, determined using aluminum-in-hornblende barometry: Implications for northward translation of Baja British Columbia: Discussion and Reply. *Geological Society of America Bulletin* 109, 1223–1227.
- Annis, D., 2012. EBSD and Microstructural Analysis of Quartzofeldspathic Rocks from the South Mountains, Arizona: An Evaluation of Flow Laws and Crustal Rheology. California State University, Northridge, 121.
- Aubourg, C., Hebert, R., Jolivet, L., Cartayrade, G., 2000. The magnetic fabric of metasediments in a detachment shear zone: the example of Tinos island (Greece). *Tectonophysics* 321, 219–236.
- Augenstein, C., Burg, J.-P., 2011. Natural annealing of dynamically recrystallised quartzite fabrics: Example from the Cévennes, SE French Massif Central. *Journal of Structural Geology* 33, 244–254.
- Bascou, J., Raposo, M.I.B., Vauchez, A., Egydio-Silva, M., 2002. Titanohematite lattice-preferred orientation and magnetic anisotropy in high-temperature mylonites. *Earth and Planetary Science Letters* 198, 77–92.
- Bates, R.G., Beck Jr, M.E., Burmester, R.F., 1981. Tectonic rotations in the Cascade Range of southern Washington. *Geology* 9, 184–189.
- Beck Jr, M.E., 1992. Some thermal and paleomagnetic consequences of tilting a batholith. *Tectonics* 11, 297–302.
- Beck, M., 1976. Discordant paleomagnetic pole positions as evidence of regional shear in the western Cordillera of North America. *American Journal of Science* 276, 694-712.
- Beck, M., Noson, L., 1972. Anomalous Paleolatitudes In Cretaceous Granitic Rocks. *Nature-Physical Science* 235, 11–13.
- Beck, M.E., Burmester, R.F., Schoonover, R., 1981. Paleomagnetism and tectonics of the Cretaceous Mt. Stuart Batholith of Washington: translation or tilt? *Earth and Planetary Science Letters* 56, 336–342.
- Bell, T., 1981. Foliation development - The contribution, geometry and significance of progressive, bulk, inhomogeneous shortening. *Tectonophysics* 75, 273–296.

- Bell, T., Hammond, R., 1984. On the internal geometry of mylonite zones. *The Journal of Geology* 92, 667–686.
- Bell, T.H., 1978. Progressive deformation and reorientation of fold axes in a ductile mylonite zone: the woodroffe thrust. *Tectonophysics* 44, 285–320.
- Benn, K., Paterson, S., Lund, S., Pignotta, G., Kruse, S., 2001. Magmatic fabrics in batholiths as markers of regional strains and plate kinematics: example of the Cretaceous Mt. Stuart batholith. *Physics and Chemistry of the Earth, Part A: Solid Earth and Geodesy* 26, 343–354.
- Brown, E.H., Talbot, J.L., 1989. Orogen-parallel extension in the North Cascades crystalline core, Washington. *Tectonics* 8, 1105–1114.
- Brown, E.H., Walker, N.W., 1993. A magma-loading model for Barrovian metamorphism in the southeast Coast Plutonic Complex, British Columbia and Washington. *Geological Society of America Bulletin* 105, 479–500.
- Butler, R.F., Dickinson, W.R., Gehrels, G.E., 1991. Paleomagnetism of coastal California and Baja California: Alternatives to large-scale northward transport. *Tectonics* 10, 561.
- Butler, R.F., Gehrels, G.E., Kodama, K.P., 2001. A Moderate Translation Alternative to the Baja British Columbia Hypothesis. *GSA Today* 11, 4–10.
- Butler, R.F., Gehrels, G.E., McClelland, W.C., May, S.R., Klepacki, D., 1989. Discordant paleomagnetic poles from the Canadian Coast Plutonic Complex: Regional tilt rather than large-scale displacement? *Geology* 17, 691–694.
- Cao, S., Liu, J., Leiss, B., 2010. Orientation-related deformation mechanisms of naturally deformed amphibole in amphibolite mylonites from the Diancang Shan, SW Yunnan, China. *Journal of Structural Geology* 32, 606–622.
- Carreras, J., Druguet, E., Griera, A., 2005. Shear zone-related folds. *Journal of Structural Geology* 27, 1229–1251.
- Carreras, J., Estrada, A., White, S., 1977. The effects of folding on the c-axis fabrics of a quartz mylonite. *Tectonophysics* 39, 3–24.
- Cobbold, P.R., Quinquis, H., 1980. Development of sheath folds in shear regimes. *Journal of Structural Geology* 2, 119–126.
- Coelho, S., Passchier, C.W., Grasemann, B., 2005. Geometric description of flanking structures. *Journal of Structural Geology* 27, 597–606.
- Coney, P.J., Jones, D.L., Monger, J.W.H., 1980. Cordilleran suspect terranes. *Nature* 288, 329–333.

- Costanzo-Alvarez, V., Dunlop, D.J., 1988. Paleomagnetic evidence for post-2.55-GA tectonic tilting and 1.1-Ga Reactivation in the Southern Kapuskasing Zone, Ontario, Canada. *Journal of Geophysical Research* 93, 9126-9136.
- Dempsey, E.D., Prior, D.J., Mariani, E., Toy, V.G., Tatham, D.J., 2011. Mica-controlled anisotropy within mid-to-upper crustal mylonites: an EBSD study of mica fabrics in the Alpine Fault Zone, New Zealand. *Geological Society, London, Special Publications* 360, 33–47.
- Van Diver, B.R., 1964. Petrology of the metamorphic rocks, Wenatchee Ridge area, central northern Cascades, Washington. University of Washington, 140.
- Van Diver, B.R., 1967. Contemporaneous faulting-metamorphism in Wenatchee Ridge area, Northern Cascades, Washington. *American Journal of Science* 265, 132–150.
- Erikson, E.H., 1977. Petrology and petrogenesis of the Mount Stuart batholith - Plutonic equivalent of the high-alumina basalt association? *Contributions to Mineralogy and Petrology* 60, 183–207.
- Evans, B.W., Berti, J.W., 1986. Revised metamorphic history for the Chiwaukum Schist, North Cascades, Washington. *Geology* 14, 695-698.
- Ferré, E., 2000. Preserved magnetic fabrics vs. annealed microstructures in the syntectonic recrystallised George granite, South Africa. *Journal of Structural Geology* 22, 1199–1219.
- Fossen, H., 2010. *Structural Geology*. Cambridge University Press, Cambridge, UK. 463.
- Fossen, H., Tikoff, B., 1993. The deformation matrix for simultaneous simple shearing, pure shearing and volume change, and its application to transpression-transension tectonics. *Journal of Structural Geology* 15, 413–422.
- Getsinger, J.S., 1978. A Structural and Petrologic Study of the Chiwaukum Schist on Nason Ridge, Northeast of Stevens Pass, North Cascades, Washington. 151.
- Ghosh, G., Kumari, S., Patil, S.K., Mukhopadhyay, J., Ray, A., 2010. Superposed deformation fabrics in the Precambrian metabasic rocks of the Iron Ore Group, Singhbhum craton, Eastern India: Evidences from anisotropy of magnetic susceptibility studies. *Journal of Structural Geology* 32, 249–261.
- Goldstein, A.G., 1988. Factors affecting the kinematic interpretation of asymmetric boudinage in shear zones. *Journal of Structural Geology* 10, 707–715.
- Goscombe, B., 2003. Asymmetric boudins as shear sense indicators--an assessment from field data. *Journal of Structural Geology* 25, 575–589.
- Haugerud, R.A., 1987. Argon geochronology of the Tenpeak Pluton and untilting of the Wenatchee Block, North Cascades Range, Washington. *Eos, Transactions, American Geophysical Union* 68, 1814.

- Heilbronner, R., Tullis, J., 2002. The effect of static annealing on microstructures and crystallographic preferred orientations of quartzites experimentally deformed in axial compression and shear. Geological Society, London, Special Publications 200, 191–218.
- Housen, B.A., 2003. Paleomagnetism of the Mount Stuart batholith revisited again: What has been learned since 1972? *American Journal of Science* 303, 263–299.
- Hudleston, P.J., Treagus, S.H., 2010. Information from folds: A review. *Journal of Structural Geology* 32, 2042–2071.
- Irving, E., Monger, J.W.H., Yole, R.W., 1980. New paleomagnetic evidence for displaced terranes in British Columbia. *Special Paper - Geological Association of Canada* 20, 441–456.
- Jeffery, G.B., 1922. The Motion of Ellipsoidal Particles Immersed in a Viscous Fluid. *Proceedings of the Royal Society A: Mathematical, Physical and Engineering Sciences* 102, 161–179.
- Jelinek, V., 1981. Characterization of the magnetic fabric of rocks. *Tectonophysics* 79, 63–67.
- Law, R.D., 1990. Crystallographic fabrics: a selective review of their applications to research in structural geology. Geological Society, London, Special Publications 54, 335–352.
- Lebit, H., Klaper, E., Lüneburg, C., 2002. Fold-controlled quartz textures in the Pennine Mischabel backfold near Zermatt, Switzerland. *Tectonophysics* 359, 1–28.
- Leiss, B., Groger, H.R., Ullemeyer, K., Lebit, H., 2002. Textures and microstructures of naturally deformed amphibolites from the northern Cascades, NW USA: methodology and regional aspects. Geological Society, London, Special Publications 200, 219–238.
- Lowes, B.E., 1972. *Metamorphic petrology and structural geology of the area east of Harrison Lake.* University of Washington. 162.
- Magloughlin, J.F., 1986. *Metamorphic petrology, structural history, geochronology, tectonics and geothermometry/geobarometry in the Wenatchee Ridge area, North Cascades.* University of Washington. 365.
- Magloughlin, J.F., 1987. A magmatic-epidote bearing leucotrandhjemite pegmatite from the North Cascades, Washington. *Geological Society of America Abstracts with Programs* 19, 232.
- Magloughlin, J.F., 1988. The White River shear zone; a major north Cascades terrane boundary and compressional structure. *Abstracts with Programs - Geological Society of America* 20, 395–396.
- Magloughlin, J.F., 1990. The Rock Lake shear zone; a partial solution to the geologic split personality of the Nason Terrane? *Abstracts with Programs - Geological Society of America* 22, 63.
- Magloughlin, J.F., 1993. A Nason terrane trilogy : I. Nature and significance of pseudotachylite; II. Summary of the structural & tectonic history; III. Major and trace element geochemistry, and

strontium and neodymium isotope geochemistry of the Chiwaukum Schist, amphibolite, and Geochemical Stability During Metamorphism.

Magloughlin, J.F., 1994. The Rock Lake shear zone; a geobarometric discontinuity in the Nason Terrane, and implications for the timing of metamorphism and the mechanism of crustal thickening. Abstracts with Programs - Geological Society of America 26, 186.

Magloughlin, J.F., 1995. A cryptic shear zone from the North Cascade Mountains; new (super 40) Ar/ (super 39) Ar dates, thermobarometry, and textural evidence for offset along the Rock Lake shear zone. Abstracts with Programs - Geological Society of America 27, 283.

Magloughlin, J.F., Edwards, R.L., 1993. Geochemistry of the Chiwaukum Schist, Washington: Evidence for a Back-Arc Basin and Island Arc Complex, the Accretion of a Juvenile Oceanic Terrane, and Geochemical Stability During Metamorphism. Abstracts with Programs - Geological Society of America 25, 321–322.

Magloughlin, J.F., Evans, B.W., 1987. Three unusual high pressure rocks from the Nason Terrane, North Cascades, Washington. Geological Society of America Abstracts with Programs 19, 400.

Mahoney, B.J., Mustard, P.S., Haggart, J.W., Friedman, R.M., Fanning, M.C., McNicoll, V.J., 1999. Archean zircons in Cretaceous strata of the western Canadian Cordillera: The “Baja B.C.” hypothesis fails a “crucial test”. *Geology* 27, 195.

Mamtani, M. a., Sengupta, P., 2010. Significance of AMS analysis in evaluating superposed folds in quartzites. *Geological Magazine* 147, 910–918.

McGroder, M.F., 1991. Reconciliation of two-sided thrusting, burial metamorphism, and diachronous uplift in the Cascades of Washington and British Columbia. *Geological Society of America Bulletin* 103, 189–209.

Miller, R., Paterson, S., Lebit, H., Alsleben, H., Luneburg, C., 2006. Significance of composite lineations in the mid- to deep crust: a case study from the North Cascades, Washington. *Journal of Structural Geology* 28, 302–322.

Miller, R.B., 1985. The ophiolitic Ingalls Complex, north-central Cascade Mountains, Washington. *Geological Society of America Bulletin* 96, 27–42.

Misch, P., 1982. North Cascades geology. *Geological Society of America Abstracts with Programs* 14, 217.

Monger, J.W.H., Irving, E., 1980. Northward displacement of north-central British Columbia. *Nature* 285, 289–294.

Monger, J.W.H., Price, R.A., 1979. Geodynamic evolution of the Canadian Cordillera — progress and problems. *Canadian Journal of Earth Sciences* 16, 770–791.

- Monger, J.W.H., Price, R.A., Tempelman-Kluit, D.J., 1982. Tectonic accretion and the origin of the two major metamorphic and plutonic belts in the Canadian Cordillera. *Geology* 10, 70.
- Monger, J.W.H., Souther, J.G., Gabrielse, H., 1972. Evolution of the Canadian Cordillera; a plate-tectonic model. *American Journal of Science* 272, 577–602.
- Ono, T., Hosomi, Y., Arai, H., Takagi, H., 2010. Comparison of petrofabrics with composite magnetic fabrics of S–C mylonite in paramagnetic granite. *Journal of Structural Geology* 32, 2–14.
- Otani, M., Wallis, S., 2006. Quartz lattice preferred orientation patterns and static recrystallization: Natural examples from the Ryoke belt, Japan. *Geology* 34, 561–564.
- Parés, J.M., 2002. Phyllosilicate fabric characterization by Low-Temperature Anisotropy of Magnetic Susceptibility (LT-AMS). *Geophysical Research Letters* 29, 2215–2218.
- Pares, J.M., van der Pluijm, B.A., 2002. Evaluating magnetic lineations (AMS) in deformed rocks. *Tectonophysics* 350, 283–298.
- Park, Y.-H., Doh, S.-J., Kim, W., Suk, D., 2005. Deformation history inferred from magnetic fabric in the southwestern Okcheon metamorphic belt, Korea. *Tectonophysics* 405, 169–190.
- Passchier, C.W., 1987. Stable positions of rigid objects in non-coaxial flow—a study in vorticity analysis. *Journal of Structural Geology* 9, 679–690.
- Passchier, C.W., 2001. Flanking structures. *Journal of Structural geology* 23, 951–962.
- Passchier, C.W., Trouw, R.A.J., 2005. *Microtectonics*, 2nd ed. Springer, New York, NY, United States. 366.
- Paterson, S., Miller, R., 1998. Regional tilt of the Mount Stuart batholith, Washington, determined using aluminum-in-hornblende barometry: Implications for northward translation of Baja British Columbia: Discussion and Reply. *Geological Society of America Bulletin* 110, 685–690.
- Paterson, S.R., 2004. Driving mechanisms for >40 km of exhumation during contraction and extension in a continental arc, Cascades core, Washington. *Tectonics* 23, 1–30.
- Piazolo, S., 2002. Controls on lineation development in low to medium grade shear zones: a study from the Cap de Creus peninsula, NE Spain. *Journal of structural geology* 24, 25–44.
- Prasannakumar, V., 2010. Application of SEM-EBSD to regional scale shear zone analysis: A case study of the Bhavani Shear Zone, South India. *Journal of the Geological Society of India* 75, 183–201.
- Richter, C., Ratschbacher, L., Frisch, W., 1993. Magnetic fabrics, crystallographic preferred orientation, and strain of progressively Metamorphosed pelites in the Helvetic Zone of the Central Alps (Quartenschiefer Formation). *Journal of Geophysical Research* 98, 9557–9570.

- Stowell, H.H., Bulman, G.R., Zuluaga, C.A., Tinkham, D.K., Miller, R.B., Stein, E., 2007a. Mid-crustal Late Cretaceous metamorphism in the Nason terrane, Cascades crystalline core, Washington, USA: Implications for tectonic models. *Memoir - Geological Society Of America* 200, 211–232.
- Stowell, H.H., Bulman, G.R., Zuluaga, C.A., Tinkham, D.K., Miller, R.B., Stein, E., 2007b. Mid-crustal Late Cretaceous metamorphism in the Nason terrane, Cascades crystalline core, Washington, USA: Implications for tectonic models, in: *Memoir - Geological Society of America: 4-D Framework of Continental Crust*. Geological Society of America, pp. 211–232.
- Stowell, H.H., Tinkham, D.K., 2003. Integration of phase equilibria modelling and garnet Sm-Nd chronology for construction of P-T-t paths: examples from the Cordilleran Coast Plutonic Complex, USA. *Geological Society, London, Special Publications* 220, 119–145.
- Symons, D., 2000. Eocene (51 Ma) end to northward translation of the Coast Plutonic Complex: paleomagnetism and K–Ar dating of the White Pass Dikes. *Tectonophysics* 326, 93–109.
- Tabor, R., Zartman, R., Frizzell Jr, V., 1987. Possible tectonostratigraphic terranes in the North Cascades crystalline core, Washington. *Selected papers on the geology of Washington: Washington Division of Geology and Earth Resources Bulletin* 77, 107–127.
- Tabor, R.W., Haugerud, R.H., Brown, E.H., Babcock, R.S., Miller, R.B., 1989. Sedimentation and tectonics of western North America; Volume 2, Accreted terranes of the North Cascades Range, Washington Field trips for the 28th international geological congress. *Am. Geophys. Union : Washington, DC, United States, U. S. Geol. Surv., Menlo Park, CA, United States*. 284.
- Tikoff, B., Fossen, H., 1993. Simultaneous pure and simple shear: the unifying deformation matrix. *Tectonophysics* 217, 267–283.
- Tikoff, B., Greene, D., 1997. Stretching lineations in transpressional shear zones: an example from the Sierra Nevada Batholith, California. *Journal of Structural Geology* 19, 29–39.
- Trouw, R.A.J., Passchier, C.W., Wiersma, D.J., 2009. *Atlas of Mylonites - and related microstructures*. Springer Berlin Heidelberg, Berlin, Heidelberg. 322.
- Wallis, S.R., Platt, J.P., Knott, S.D., 1993. Recognition of syn-convergence extension in accretionary wedges with examples from the Calabrian Arc and the Eastern Alps. *American Journal of Science* 293, 463–494.
- Wells, R.E., 1990. Paleomagnetic rotations and the Cenozoic tectonics of the Cascade arc, Washington, Oregon, and California. *Journal of Geophysical Research* 95, 19409–19417.
- Xypolias, P., 2010. Vorticity analysis in shear zones: A review of methods and applications. *Journal of Structural Geology* 32, 2072–2092.
- Yuanchao, L., 1999. Crystallographic preferred orientation and slip system of hornblende in the Florence shear zone, central Australia. *Journal of Mineralogy and Petrology* 19, 1–7.

Zaggle, R.H., Magloughlin, J.F., 2013. Is the Wenatchee Ridge Orthogneiss a Mesozoic analog for Archean TTG? Rocky Mountain Section of The Geological Society of America, Abstracts with Programs 45.

Zapletal, K., 1990. Low-field susceptibility anisotropy of some biotite crystals. *Physics of the Earth and Planetary Interiors* 63, 85–97.

7. Appendices

7.1. Appendix I

Field Data and Structural Measurements:

Table 7.1.1: Positional information for each station.

Location #	Easting (UTM)	Northing (UTM)	Elevation (Feet)	Distance Along Transect (m)
RM-01	652254.7	5295847.7	5989.4	2243.9
RM-02	652240.5	5295827.5	6003.9	2219.7
RM-03	652266.7	5295831.4	5959.5	2241.0
RM-04	652280.3	5295846.7	5973.5	2261.3
RM-05	652296.7	5295850.2	5953.5	2275.5
RM-06	652237.5	5295898.2	5970.5	2267.5
RM-07	652235.8	5295919.3	5923.3	2281.2
RM-08	652186.2	5295860.8	5978.0	2204.7
RM-09	652198.7	5295832.0	5999.1	2193.3
RM-10	652253.4	5295763.9	6048.7	2183.8
RM-11	652249.0	5295733.5	6109.9	2159.2
RM-12	652290.3	5295703.6	6113.2	2167.3
RM-13	652334.2	5295716.4	6059.4	2207.4
RM-14	652358.1	5295697.5	6041.9	2210.8
RM-15	652394.3	5295699.9	6006.7	2238.1
RM-16	652419.1	5295702.2	5978.3	2257.3
RM-17	652405.4	5295785.6	5897.5	2306.6
RM-18	652411.4	5295748.7	5950.9	2284.8
RM-19	652216.1	5295698.0	6165.5	2110.8
RM-20	652193.7	5295658.9	6170.1	2067.3
RM-21	652083.4	5295618.2	6229.2	1960.6
RM-22	652020.9	5295628.8	6263.2	1923.8
RM-23	651772.7	5295450.5	6363.7	1622.2
RM-24	651736.1	5295396.9	6434.5	1558.5
RM-25	651733.5	5295322.1	6423.2	1503.8
RM-26	651730.4	5295284.2	6429.4	1474.8
RM-27	651987.8	5295643.6	6313.9	1910.9
RM-28	652201.8	5295708.8	6138.2	2108.4
RM-29	652160.7	5295672.5	6178.5	2053.6
RM-30	652093.6	5295658.4	6212.0	1996.2
RM-31	652139.0	5295641.0	6227.7	2016.0
RM-32	651995.7	5295678.1	6275.9	1940.9
RM-33	652041.5	5295705.3	6196.5	1992.5

RM-34	651988.6	5295757.1	6151.3	1991.7
RM-35	652049.7	5295765.6	6100.8	2040.9
RM-36	652121.6	5295811.1	6010.9	2123.9
RM-37	652205.6	5295758.2	6088.3	2146.0
RM-38	652160.9	5295715.4	6106.6	2084.1
RM-39	652157.3	5296027.7	5975.6	2302.4
RM-40	652262.1	5295986.1	5961.7	2347.1
RM-41	652331.6	5296031.0	5980.9	2427.9
RM-42	652347.7	5295947.6	5940.5	2380.4
RM-43	652367.2	5295970.5	5955.9	2410.4
RM-44	652499.2	5296001.3	5990.9	2525.4
RM-45	652439.3	5295920.7	5940.9	2426.2
RM-46	652532.2	5295918.1	5933.3	2489.9
RM-47	652552.5	5295882.6	5968.9	2479.2
RM-48	652634.7	5295835.6	5931.2	2504.1
RM-49	652786.2	5295885.7	5916.0	2646.7
RM-50	652986.8	5295948.8	5936.4	2833.1
RM-51	653065.8	5296519.8	5558.7	3292.7
RM-52	653101.2	5296491.3	5569.0	3297.6
RM-53	653084.3	5296317.5	5646.9	3162.8
RM-54	653032.7	5296364.5	5615.6	3159.5
RM-55	653204.8	5296283.5	5672.3	3223.9
RM-56	653195.0	5296184.1	5780.8	3146.7
RM-57	653195.7	5295993.0	5862.4	3012.0
RM-58	653262.2	5295848.7	5960.5	2957.1
RM-59	652237.1	5295669.7	6133.5	2105.7
RM-60	652190.6	5295626.9	6133.3	2042.5
RM-61	652135.6	5295582.8	6140.8	1972.4
RM-62	652163.0	5295526.4	6066.6	1951.9
RM-63	652191.6	5295519.8	6038.1	1967.5
RM-64	652244.2	5295524.3	5989.8	2007.9
RM-65	652275.3	5295592.2	6036.7	2077.8
RM-66	652335.3	5295631.3	6019.9	2147.9
RC-01	653474.5	5293443.3	2663.4	1406.4
RC-02	653848.9	5293700.4	2667.7	1852.8
RC-03	654744.6	5294106.4	2771.1	2773.3
RC-04	655888.4	5294074.2	2667.4	3559.3

Table 7.1.2: Foliation data, using right-hand rule.

Location #	Foliation (Strike – Dip)	Foliation Strike - Average	Foliation Dip - Average
RM-01	305-68	305	68
RM-02	320-74	320	74
RM-03	320-82; 315-83	317.5	82.5
RM-05	310-84	310	84
RM-06	325-85	325	85
RM-07	326-82	326	82
RM-08	320-80	320	80
RM-10	321-84	321	84
RM-12	310-68	310	68
RM-14	320-78	320	78
RM-15	309-72	309	72
RM-16	311-72	311	72
RM-17	319-68	319	68
RM-19	311-70	311	70
RM-20	324-86	324	86
RM-21	211-73	211	73
RM-24	251-56	251	56
RM-27	309-83	309	83
RM-28	311-86	311	86
RM-29	316-82	316	82
RM-30	308-82	308	82
RM-33	308-78	308	78
RM-34	324-75	324	75
RM-36	309-81	309	81
RM-37	312-75	312	75
RM-38	306-72	306	72
RM-39	288-74	288	74
RM-40	325-72	325	72
RM-42	311-76	311	76
RM-43	300-70	300	70
RM-44	310-79	310	79
RM-45	310-81	310	81
RM-46	322-86	322	86
RM-47	309-71	309	71
RM-48	301-71	301	71
RM-49	301-51	301	51
RM-50	142-81	142	81
RM-52	131-74	131	74
RM-53	316-97	316	97

RM-54	320-89	320	89
RM-56	134-72	134	72
RM-57	139-88	139	88
RM-58	311-82	311	82
RM-59	321-78	321	78
RM-66	319-82	319	82
RC-02	322-74	322	74
RC-03	320-78	320	78

Table 7.1.3: Mineral lineation data.

Location #	Mineral Lineation (Plunge-Trend)	Average Plunge
RM-12	82-032 Amphibole	82
RM-19	64-345	64
RM-20	46-175; 84-090 Biotite	65
RM-23	46-045	46
RM-27	68-009	68
RM-28	86-356 Amphibole	86
RM-29	81-009 Amphibole	81
RM-30	76-032 Amphibole	76
RM-31	80-032	80
RM-32	64-026	64
RM-33	77-019 Amphibole; 89-036 Amphibole	83
RM-34	89-011	89
RM-35	76-064 Amphibole	76
RM-36	78-352	78
RM-37	88-008 Amphibole; 82-045 Amphibole	85
RM-38	73-004 Amphibole; 56-033 Amphibole	64.5
RM-40	74-356	74
RM-42	29-115	29
RM-44	44-007 Amphibole	44
RM-46	17-064 Amphibole; 07-308 Amphibole	12
RM-48	78-307 Amphibole	78
RM-50	06-112 Biotite	06
RM-52	16-312	16
RM-56	31-326 Staurolite	31
RM-57	08-146 Amphibole; 07-136 Amphibole; 22-144 Amphibole	12.3
RM-58	09-328 Amphibole; 12-337 Amphibole; 33-126 Amphibole	18
RM-59	28-021 Amphibole; 86-028 Amphibole; 76-053 Amphibole	63.3
RM-60	76-044 Amphibole; 76-044 Amphibole	76
RM-61	54-121	54
RM-64	81-007 Amphibole	81
RM-65	79-019 Amphibole; 88-015 Amphibole; 78-021 Amphibole; 74-003 Amphibole	79.75
RM-66	78-006 Amphibole	78
RC-02	77-356 Amphibole; 73-009 Amphibole	75
RC-03	02-304	02

Table 7.1.4: Fold hinge data.

Location #	Fold Hinge (Plunge-Trend)	Fold Hinge Plunge - Average
RC-01	75-328 Qtz Vein; 76-327 Qtz Vein; 74-324 Qtz Vein; 56-312 Qtz Vein; 74-316 Qtz Vein	71
RM-26	79-298 Schist; 24-256 Qtz Vein	51.5
RM-23	74-106 Qtz Vein	74
RC-02	66-319 Qtz Vein; 61-337 Qtz Vein; 58-328 Qtz Vein; 61-322 Qtz Vein	61.5
RM-27	89-106 Qtz Vein	89
RM-22	75-328	75
RM-32	59-014 Qtz Vein; 81-326; 76-010	72
RM-62	72-286 Qtz Vein; 66-308 Qtz Vein	69
RM-21	71-069 Qtz Vein; 84-286 Qtz Vein; 69-352 Qtz Vein	74.6
RM-61	74-311 Qtz Vein; 66-312 Qtz Vein; 64-308 Qtz Vein	68
RM-34	74-045 Qtz Vein	74
RM-33	82-092; 88-226	85
RM-64	84-278 Qtz Vein; 66-323 Qtz Vein; 70-129 Schist; 73-289 Schist	73.25
RM-31	74-262	74
RM-35	57-129; 69-026	63
RM-60	74-336 Qtz Vein; 82-122 Qtz Vein; 83-111 Qtz Vein	79.6
RM-20	75-176 Qtz Vein	75
RM-65	56-127 Qtz Vein; 87-128 Qtz Vein; 81-115 Qtz Vein; 85-125 Qtz Vein	77.25
RM-38	75-324 Qtz Vein; 61-343 Qtz Vein	68
RM-59	76-129 Qtz Vein; 70-306 Qtz Vein; 74-309 Qtz Vein	73.3
RM-28	77-325 Qtz Vein; 85-323 Qtz Vein	81
RM-36	65-312	65
RM-37	79-011 Qtz Vein; 76-126 Qtz Vein	77.5
RM-66	83-112 Qtz Vein; 82-132 Qtz Vein	82.5
RM-08	78-330 Qtz Vein	78
RM-13	61-094 Qtz Vein	61
RM-14	66-121 Qtz Vein	66
RM-02	72-040	72
RM-15	83-126 Qtz Vein	83
RM-03	45-337 Qtz Vein; 44-355 Qtz Vein	44.5
RM-01	67-300; 65-114	66
RM-16	59-114 Qtz Vein	59
RM-05	52-315 Qtz Vein	52
RM-40	57-299 Qtz Vein; 65-311 Qtz Vein; 62-324 Qtz Vein	61.3
RM-42	74-316 Qtz Vein	74
RM-43	78-317; 73-311	75.5
RM-45	38-322 Qtz Vein	38

RM-47	47-312 Qtz Vein; 36-315 Qtz Vein	41.5
RM-46	59-309 Qtz Vein; 51-312 Qtz Vein; 70-311 Qtz Vein	60
RM-48	51-302 Qtz Vein; 58-324 Qtz Vein	54.5
RM-49	32-322 Qtz Vein; 31-295 Qtz Vein	31.5
RC-03	24-322 Qtz Vein; 09-322 Qtz Vein	16.5
RM-50	23-322 Qtz Vein; 33-052 Qtz Vein; 64-324 Qtz Vein	40
RM-58	18-134 Qtz Vein; 17-137 Qtz Vein; 33-302 Qtz Vein; 19-315 Qtz Vein; 18-313 Qtz Vein	21.83
RM-57	33-319 Qtz Vein; 32-311 Qtz Vein; 24-316 Qtz Vein	29.6
RM-56	53-312 Qtz Vein; 45-321 Qtz Vein; 34-324 Qtz Vein	44
RM-54	31-302 Qtz Vein; 23-321 Qtz Vein; 22-321 Qtz Vein	25.3
RM-53	56-111 Qtz Vein	56
RM-55	28-133 Qtz Vein; 26-332 Qtz Vein	27
RM-52	23-132 Qtz Vein; 18-136 Qtz Vein; 04-317 Qtz Vein	15
RC-04	11-318 Qtz Vein; 06-314 Qtz Vein; 08-315 Qtz Vein	8.3

Table 7.1.5: Drill core orientations.

Location #	Drill Core	Orientation (trend, plunge)
RM-01	RM-1	310-67
RM-05	RM-5	025-14
RM-06	RM-6	150-52
RM-08	RM-8	102-61
RM-11	RM-11	210-20
RM-14	RM-14	220-41
RM-18	RM-18	210-42
RM-21	RM-21	330-64
RM-25	RM-25B	327-37
RM-26	RM-26	254-29
RM-27	RM-27	110-47
RM-31	RM-31-A & B	278-61; 090-63
RM-34	Rm-34-B	232-36
RM-36	RM-36	294-67
RM-39	RM-39	314-51
RM-40	RM-40	306-71
RM-42	RM-42	054-57
RM-44	RM-44	211-52
RM-46	RM-46	162-42
RM-48	RM-48	219-42
RM-51	RM-51	131-40
RM-52	RM-52	054-44
RM-54	RM-54	229-41
RM-55	RM-55	158-46
RM-61	RM-61	298-49
RM-62	RM-62	309-53
RM-63	RM-63	321-78
RM-65	RM-65	296-54

Table 7.1.6: Hand sample orientations.

Location #	Hand Sample # - 1	Hand Sample Orientation - 1	Hand Sample # - 2	Hand Sample Orientation - 2	Hand Sample # - 3	Hand Sample Orientation - 3
RM-04	RM-4	314-85				
RM-09	RM-9	035-10				
RM-20	RM-20	316-76				
RM-25	RM-25	122-74				
RM-33	RM-33-A	295-64	RM-33-B	305-84	RM-33-C	281-72
RM-34	RM-34	335-79				
RM-41	RM-41	300-82				
RM-45	RM-45	029-39				
RC-01	RC-1-A	012-37	RC-1-B	122-70		
RC-02	RC-2	319-61				
RC-03	RC-3	318-04				

Table 7.1.7: Photograph information.

Location #	Photo #	Photo Orientation	Photo Description
RM-01	101-0793	220-65	Boudinage
RM-02	101-0795	040-72	Floating Fold Hinge
RM-05	101-0796	170-54	Fold Pattern
RM-07	101-0797	302-76	Metatonalite Sill
RM-11	101-0799	216-74	Asymmetric fold hinge
RM-13	101-0802	224-75	Boudinage
RM-14	101-0803	275-72	Sheath Fold(?)
RM-16	101-0808	295-56	Boudinaged Folds
RM-21	101-0819	354-56	Folding pattern in schist
RM-26	101-0829	331-72	S-fold
RM-28	101-0834-7	225-49	Amphibole lineations
RM-32	101-0838	000-74	Sheath Fold
RM-36	101-0839	321-74	Floating fold hinges
RM-40	101-0845&6	131-79 & 283-56	Boudinage & Floating fold hinges
RM-61	101-0868 & 9	264-67	Foliation Turning in on itself
RM-63	101-0870	264-68	Mylonitic Fabric
RM-65	101-0872		Amphibole mineral lineation

7.2. Appendix II

Microstructural Data:

Table 7.2.1: Sense of shear data.

Slide	L-L or R-L?	NE or SW side up?	Confidence
RM-63	R-L	SW	Low
RM-41	L-L	NE	Low
RM-4	R-L	NE	High
RM-36	R-L	NE	Med
RM-14	L-L	NE	Low
RC-2	R-L	NE	High
N253-2-3	L-L	NE	Low
N251-4	R-L	SW	Med
N250-2	L-L	NE	High
N247-1	R-L	SW	Low
N245-6	L-L	NE	Med
N245-5	L-L	NE	Med
N245-4	R-L	NE	Med
N245-4	L-L	SW	Low
N245-3	L-L	NE	Low
N219-7	L-L	NE	Low
N219-6	R-L	SW	Low
N219-2	L-L	NE	Low

Table 7.2.2: Vorticity data for porphyroclasts in schist.

	Thin Section	Long Axis	Short Axis	R	B	ϕ
clast1	RC-2	2.54	2.28	1.11404	0.10757	-70
clast2	RC-2	1.43	1.13	1.26549	0.2312	-78
clast3	RC-2	1.11	0.85	1.30588	0.26072	77
clast4	RC-2	1.63	1.27	1.28346	0.24451	87
clast5	RM-36	2.29	1.37	1.67153	0.47285	-14
clast6	RM-36	1.22	0.97	1.25773	0.22537	-15
clast7	RM-14	2.17	1.86	1.16667	0.15294	5
clast8	RM-14	1.41	1.24	1.1371	0.12778	27
clast9	RM-14	2.07	1.91	1.08377	0.08027	-56
clast10	RM-14	2.14	1.95	1.09744	0.09271	-88
clast11	RM-14	1.54	1.44	1.06944	0.06704	7
clast12	N245-4	1.42	0.85	1.67059	0.47242	-39.8
clast13	N245-4	1.25	1.04	1.20192	0.18188	-39.8
clast14	N245-4	2.49	1.8	1.38333	0.31357	-40.2
clast15	N219-7	1.45	1.13	1.28319	0.2443	-20.6
clast16	N219-7	1.16	0.92	1.26087	0.22774	56.1
clast17	N219-7	1.44	0.78	1.84615	0.54631	-3.1
clast18	N219-7	1.42	1.27	1.11811	0.11118	-9.7
clast19	N219-7	1.69	1.39	1.21583	0.19297	-51.8
clast20	N219-7	3.03	1.68	1.80357	0.52973	10.8
clast21	N219-7	1.17	0.82	1.42683	0.3412	-59.8
clast22	N219-7	1.53	1.06	1.4434	0.35136	-39.3
clast23	N219-7	1.92	1.35	1.42222	0.33834	-33.6
clast24	N219-7	1.02	0.69	1.47826	0.37211	59.2
clast25	N219-7	1.12	0.8	1.4	0.32432	4.9
clast26	N219-7	0.94	0.66	1.42424	0.3396	8.9
clast27	N219-7	1.06	0.58	1.82759	0.53918	-29.4
clast28	N219-7	1.2	0.83	1.44578	0.35281	-89.3
clast29	N219-6	1.94	1.16	1.67241	0.47326	27.1
clast30	N219-6	1.74	0.81	2.14815	0.64378	6.5
clast31	N219-6	1	0.76	1.31579	0.26775	12.54
clast32	N219-6	2.3	1.2	1.91667	0.57207	-8.7
clast33	N219-6	0.96	0.6	1.6	0.4382	-5.6
clast34	N219-6	1.15	0.67	1.71642	0.49317	7.7
clast35	N219-6	1.02	0.64	1.59375	0.43503	9.8
clast36	N219-6	1.53	0.67	2.28358	0.67818	-19.7
clast37	N219-6	1.9	1.27	1.49606	0.38237	-72.9
clast38	N219-6	1.99	1.22	1.63115	0.45365	12.8
clast39	N219-2	2.01	1.49	1.34899	0.29073	11.5

clast40	N219-2	1.06	0.74	1.43243	0.34466	-27.9
clast41	N219-2	1.19	0.77	1.54545	0.40976	-15.8
clast42	N219-2	1.99	0.86	2.31395	0.68526	-5.7
clast43	N219-2	2.08	1.82	1.14286	0.13274	-14.7
clast44	N253-2-3	3.68	2.63	1.39924	0.32384	5.8
clast45	N247-1	1.23	0.71	1.73239	0.50015	5.5
clast46	N247-1	3.87	1.12	3.45536	0.84543	8.7
clast47	N247-1	1.52	1.04	1.46154	0.36226	-32.8
clast48	N247-1	3.31	1.04	3.18269	0.8203	6.07
clast49	N247-1	1.23	0.82	1.5	0.38462	51.27
clast50	N247-1	2.5	1.49	1.67785	0.47578	5.84
clast51	N245-5	1.86	1.52	1.22368	0.19917	-12.1
clast52	N245-5	1.78	1	1.78	0.5202	22.3
clast53	N245-5	1.95	1.43	1.36364	0.30058	77.3
clast54	N245-4	2.12	1.72	1.23256	0.2061	30.6
clast55	N245-4	2.48	1.79	1.38547	0.31496	-43.9
clast56	N245-4	1.91	1.84	1.03804	0.03732	-75.2

Table 7.2.3: Vorticity data for porphyroclasts in metatonalite.

	Thin Section	Long Axis	Short Axis	R	B	B*	φ
clast1	RM-04	1.34	0.74	1.81081	0.5326	0.5326	15
clast2	RM-04	0.94	0.79	1.18987	0.17212	0.17212	35
clast3	RM-04	1.24	0.84	1.47619	0.3709	0.3709	14
clast4	RM-04	1.13	0.68	1.66176	0.46829	0.46829	-70
clast5	RM-04	1.99	1.18	1.68644	0.47972	0.47972	4
clast6	RM-04	2.01	0.96	2.09375	0.62851	0.62851	-15
clast7	RM-04	1.93	1.02	1.89216	0.56334	0.56334	10
clast8	RM-04	1.11	0.9	1.23333	0.2067	0.2067	-70
clast9	RM-04	1.91	1.05	1.81905	0.53585	0.53585	-57
clast10	RM-04	1.1	0.85	1.29412	0.25226	0.25226	-24
clast11	RM-04	0.99	0.62	1.59677	0.43657	0.43657	16
clast12	RM-04	0.84	0.69	1.21739	0.19421	0.19421	-82
clast13	RM-04	2.16	1.16	1.86207	0.5523	0.5523	-5
clast14	RM-04	1.3	0.86	1.51163	0.39118	0.39118	13
clast15	RM-04	1.63	0.8	2.0375	0.61176	0.61176	-31
clast16	RM-04	1.05	0.78	1.34615	0.2888	0.2888	20
clast17	RM-04	1.35	0.7	1.92857	0.57622	0.57622	34
clast18	RM-04	1.73	1.42	1.21831	0.19494	0.19494	-23
clast19	RM-04	2.8	1.49	1.87919	0.55863	0.55863	21
clast20	RM-04	1.36	0.98	1.38776	0.31644	0.31644	-57
clast21	RM-41	1.83	0.89	2.05618	0.61744	0.61744	7.5
clast22	RM-41	1.09	0.69	1.57971	0.42783	0.42783	4.9
clast23	RM-41	1.29	0.69	1.86957	0.55509	0.55509	4.9
clast24	RM-41	1.02	0.77	1.32468	0.27399	0.27399	-58.5
clast25	RM-41	3.47	1.27	2.73228	0.76374	0.76374	5.5
clast26	RM-41	1.55	0.79	1.96203	0.58759	0.58759	-32.6
clast27	RM-41	1.8	1.39	1.29496	0.25288	0.25288	15.7
clast28	RM-41	1.35	0.97	1.39175	0.31903	0.31903	-7.3
clast29	N245-6	1.95	1.17	1.66667	0.47059	0.47059	40.6

7.3. Appendix III

Magnetic Data:

Table 7.3.1: Inclination (I) and declination (D) of the magnetic susceptibility axes.

Sample	D_max_in-situ	I_max_in-situ	D_int_in-situ	I_int_in-situ	D_min_in-situ	I_min_in-situ
RC01A	-260.110	61.681	-66.323	27.625	200.657	5.748
RC01B	-46.036	31.711	-250.098	55.915	216.931	11.209
RC02-1	-62.193	1.389	30.512	62.799	207.095	27.160
RC02-2	-42.629	33.470	92.692	47.084	210.631	23.540
RC03-1	-37.759	18.029	-202.294	71.340	53.760	4.653
RC03-2	-45.370	12.420	-197.847	76.053	46.011	6.245
RM01	-51.960	81.539	120.329	8.385	210.494	1.119
RM04	112.899	69.307	-53.142	20.131	215.171	4.590
RM05	-250.341	55.930	-61.498	33.753	205.752	4.106
RM06	-249.986	39.759	-63.188	50.042	202.805	3.351
RM08	-50.623	85.162	-257.192	4.329	192.972	2.155
RM09	-185.653	40.041	73.854	12.230	-29.764	47.366
RM11	-23.193	65.291	-243.016	19.462	212.273	14.620
RM14	-42.733	70.392	-240.382	18.750	211.501	5.529
RM18	-21.643	68.185	-241.193	17.152	212.915	13.067
RM20	26.308	79.632	123.697	1.348	213.942	10.278
RM21	84.718	63.752	-78.234	25.241	188.574	6.735
RM25	190.767	77.276	22.538	12.465	-68.018	2.515
RM25B	-47.992	61.973	130.549	28.019	220.871	0.605
RM26	-244.195	82.471	-59.518	7.504	210.402	0.606
RM27	48.554	74.132	-216.448	1.419	233.953	15.801
RM31	70.274	72.192	-73.994	14.615	193.383	9.952
RM33A	216.864	66.718	24.121	22.768	-243.939	4.611
RM34	110.720	64.696	-40.492	22.507	224.905	10.962
RM34B	6.399	67.887	114.991	7.381	207.800	20.722
RM36	-25.291	64.767	125.544	22.369	220.165	11.076
RM39	-33.579	52.465	110.391	31.854	211.843	17.722
RM40	-24.689	58.792	-237.459	26.994	220.096	14.471
RM41	-51.585	6.160	-240.192	83.770	218.315	0.925
RM42	-48.475	1.016	43.748	65.431	221.062	24.545
RM44	-9.761	67.777	102.175	8.678	195.410	20.293
RM46	8.654	60.823	-241.964	10.497	213.426	26.884
RM48	-53.145	23.486	81.289	58.173	207.653	20.205
RM51	-70.376	54.310	-263.227	35.004	191.066	6.101
RM52	-67.693	18.992	-189.150	56.595	32.129	26.364
RM54	-41.235	11.525	-241.773	77.715	227.908	4.194
RM55	-238.892	32.064	-34.605	55.502	218.355	11.386
RM58	61.113	54.198	248.984	35.545	156.309	3.737
RM61	76.860	68.819	-75.472	18.942	191.366	9.131
RM62	52.324	84.222	-49.673	1.205	220.207	5.650
RM63	56.458	57.757	-77.024	23.463	183.486	20.800
RM65	-20.449	62.084	118.496	21.779	215.333	16.591